UNIVERSITÀ DEGLI STUDI DI PAVIA

DOTTORATO IN SCIENZE CHIMICHE E FARMACEUTICHE E INNOVAZIONE INDUSTRIALE (XXXIV Ciclo)

Coordinatore: Chiar.mo Prof. Giorgio Colombo

POLYMERIC MATERIALS WITH

NOBLE METALS NANOPARTICLES

Tesi di Dottorato di

Lorenzo De Vita

AA 2020/2021

Tutor

Chiar.mo Prof. Piersandro Pallavicini

SUMMARY

Abstract

The general focus of this PhD project was the combination of gold and/or silver nanoparticles with a polymeric matrix. In particular, PVA films containing pectin-stabilized AgNP and gold nanostars (GNS) coated with HS-PEG or HS-PEG-COOH have been prepared. These materials proved to combine an intrinsic microbicidal activity, due to the release of Ag^+ ions, with an on-demand action given by the photothermal response of GNS upon laser irradiation in the NIR bio-transparent window. Films containing GNS coated with HS-PEG-COOH, that act directly as cross-linking agents, are most promising for the development of medical devices for wound healing applications.

In addition, the study of PEG coating of AuNP has been carried on, particularly by potentiometric titration, in order to investigate the effect of NP-binding on the acid-base properties of PEG thiols. After the determination of the protonation constants of a set of molecules with different mw, an experimental procedure for the titration of PEG-coated AuNP was set up. The first results on AuNP@HS-PEG-COOH show a reduction of the average acidity of the carboxylic groups, attributed to the interaction between the neighboring molecules confined on the NP surface. Eventually, a novel photothermal material has been produced by the inclusion of GNS in a sponge-like PDMS scaffold, obtained via a simple templating method which could also enable control over pore size and porosity. Very elastic, hydrophobic sponges have been obtained, both with and without PEGylated GNS embedded. Preliminary data from natural solar irradiation show a remarkable photothermal response of the PDMS@GNS samples; however, a finer control is required over irradiation parameters as well as new experimental setups to assess their performance as solar water evaporators and/or oil separation platforms.

PART 1. INTRODUCTION

1.1 NANOCOMPOSITE MATERIALS

Sometimes technological advances can simply arise from the innovative combination of known materials. Nowadays, nanoparticles are widely studied and used in a large variety of research fields, ranging from catalysis to electronics, nanomedicine, sensing, environmental remediation, cosmetics and food technology, and can even be found at commercial level in some cases. The enormous interest is given by the peculiar properties that arise when a material is limited to the nanometric range, that are surprisingly different from those presented by the bulk counterpart.

The constant emergence of new applications for nanomaterials is made possible by the increasing knowledge not only on the preparation, but also and most importantly, on the modulation of the surface chemistry, (bio)functionalization and self-assembly of nanoparticles of different chemical nature (metals, semiconductors, metal oxides, polymers etc.). At the same time, their combination with other materials is fundamental in the development of hybrid materials that hold the promise of not only mitigating the intrinsic limitations of the building blocks, but also providing additional functionalities.[1]

More specifically, when considering noble metals nanomaterials, the preparation of monodisperse nanoparticles with specific shape, size and optical properties is often performed by wet-chemistry through the fine tuning of synthetical parameters. However, the resulting colloidal suspensions are rather delicate and are easily destabilized by changes in the ionic strength, solvents or temperature, if not otherwise protected. The incorporation in another material, such as a polymeric matrix, can yield robust composites showing advanced properties with diverse potential applications as, for instance, opto-electronic devices, smart

biomedical devices or biosensing platforms.[2] In particular, the combination of noble metals nanoparticles with a polymeric material could lead to many advantages: the stabilization of the NP inside the polymer matrix, leading to the modulation of their reactivity (e.g. oxidability) and their potential toxicity, the enhancement of mechanical properties of the material, the gain of specific properties given by the NP, such as plasmonic and stimuli-responsive effects in general.

This synergistic effect given by the interplay of the different components have boosted the interest in the investigation of this promising class of materials from a multi-disciplinary point of view in the past decade.[3] One of the earliest works on such materials described the immobilization of gold nanoparticles (AuNP) in polyacrylamide (PAAm), obtained by swelling the dehydrated gel in the presence of the colloidal solution, giving a uniform distribution of the AuNP in the gel matrix.[4] Later on, various approaches have been reported for the preparation of these nanocomposites.

Four main approaches can be followed for the preparation of polymeric nanocomposites (Figure 1):

   a) polymer matrix formation in a nanoparticle suspension,
   b) nanoparticle incorporation into a preformed polymer matrix,
   c) *in situ* nanoparticle formation within a preformed polymer and
   d) polymer matrix formation driven by functionalized nanoparticles.
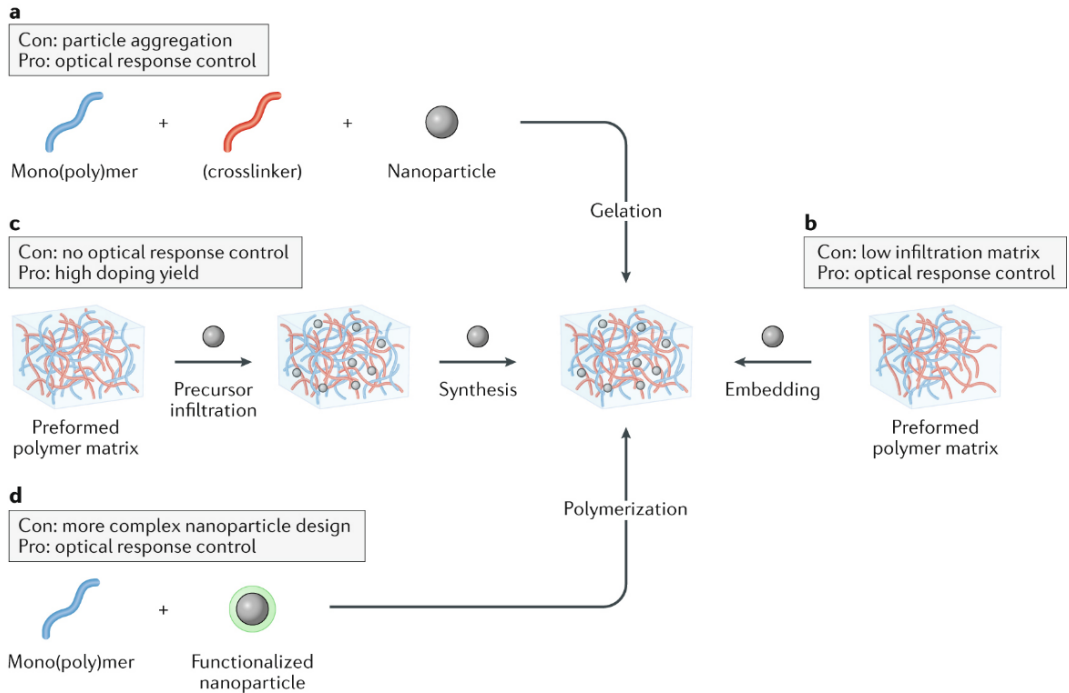
Figure 1 Alternative approaches for the fabrication of polymer nanocomposites: (a) polymer matrix formation in a nanoparticle suspension; (b) nanoparticle incorporation into a preformed polymer matrix; (c) in situ nanoparticle formation within a preformed polymer; (d) polymer matrix formation driven by functionalized nanoparticles. [2]

The choice of the method must take into account, and is generally determined by, the final application aimed for the composite material. For example, for the fabrication of plasmonic polymer nanocomposites for applications requiring well-defined or modulated optical responses, an approach based on *in situ* nanoparticle synthesis would not be suitable, as it would allow a poor control on the nanoparticles shape and dimensions, that in turn strongly influence their plasmonic response.

If the role of nanoparticles in the polymer nanocomposite is instead to enhance the mechanical or thermal properties, then approaches involving a strong bond (covalent or coordinative) between the nanoparticles or their coating and the polymer matrix are preferred.

1.1.1 Noble metals nanocomposites

The combination of metal nanoparticles with a polymeric substrate allows the preparation of hybrid materials that generally retain the properties of the bulk polymer with the addition of those imparted by the embedded nanoparticles, such as improved electrical conductivity, response to optical stimuli, antimicrobial action, etc. The applications of these hydrogels are found in catalysis, sensors, biomedical devices as well as microfluidics and separation technology.

1.1.1.1 Silver-based materials

Silver nanoparticles can add electronic, optical and antibacterial properties to a variety of polymer hydrogels. Tokarev and coworkers demonstrated that AgNP enhance the efficacy of surface plasmon resonance (SPR)-based sensors.[5] AgNP incorporated into pH-responsive hydrogels with the enzyme glucose oxidase function as glucose concentration sensors. The swelling-shrinking transition of AgNP filled hydrogels alter the interparticle distance and so affect the LSPR absorptions of the nanoparticles, leading to sensitive glucose detection.[6] Additionally, AgNP have been incorporated into hydrogels to form electrically conducting hydrogels. The correlation between initial precursor Ag^+ ions concentration and swelling ratio of the hydrogel have a direct impact on conductivity. A higher concentration of Ag^+ ions resulted in better conductivity, but reduced swelling ratios, and vice versa.[7] Other authors reported multicomponent hydrogels made from polymer particles that are decorated with polymer brushes and cross-linked within a poly(vinyl alcohol) matrix. Additional silver nanoparticles (35 nm) are generated on the surfaces of the brush particles or within the PVA matrix. The resulting hydrogels have a catalytic activity for the reduction of p-nitrophenol that is retained over several months.[8]

1.1.1.2 Gold-based materials

Stimuli-responsive AuNP composites have been reported by several groups.[9,10] External stimuli such as temperature or pH cause a change in conductivity of an hydrogel due to the change of the inter-particle distance. Even though AuNP-hydrogel composites have shown efficacy as SPR based sensors[11] and in anti-bacterial applications,[12] the high cost of gold has so far prevented wide-scale adoption of AuNP for such applications. Irradiation of light at the Au plasmonic peak induces localized heating within a temperature-responsive gel matrix. This phenomenon has been proposed for remote-controlled drug delivery.[13] If the temperature rises above the lower critical solution temperature (LCST) of the gel matrix, the gel structure collapses resulting in an on-demand burst release of drugs as opposed to a diffusion-controlled release. Shiotani and coworkers have demonstrated this concept using a system of Au nanorods-NIPAAm composite hydrogels and rhodamine-based materials.[14] They reported a fast and reversible shrinking and re-swelling of this composite hydrogel. The fast response was attributed to heat generation within the gel matrix, rather than external to the matrix. Different sized or structured AuNPs immobilized in a thermo-responsive hydrogel matrix can also function as remote-controlled microfluidic valves. The principle behind this application relies on the variation of thermal response with nanoparticle size. The use of different excitation wavelengths renders opening of different valves when the correct amount of energy is delivered by matching the plasmonic resonant peaks of the NP. On irradiation with 532 nm light, Au colloids (3–10 nm diameter) with plasmonic peak at 532 nm collapse the hydrogel network, opening the valve. Valves containing Au nanoshell (diameter 120nm, shell thickness 10nm) hydrogel composites remain unaffected. Opening of these valves containing Au nanoshells could be achieved upon illumination at 832 nm. Another

application of gold nanoparticle hydrogels describes how the spatial coupling of the nanoparticles is dependent on the stimuli induced swelling/de-swelling of the poly(2-vinyl pyridine) polymer. This pH-dependent process changes the localized surface plasmon resonance, allowing the material to analyze pH by measuring the change of the UV–vis spectrum of the hydrogel. The authors report a significant improvement in sensitivity and processing conditions compared to other technologies.[15]

1.1.2 Perspectives

Nanoparticle-hydrogel composites exhibit multi-functional and stimuli responsive properties, making them ideal for "smart" materials, including i) antimicrobial scaffolds; ii) photothermally active hydrogels; iii) soft material catalysts; iv) environmental absorbents; v) drug delivery vehicles; vi) optical detection sensors and vii) soft actuators. Potential applications include i) safe, clinically implantable nanoparticle-hydrogel composite systems for bio-sensing and therapy; ii) environmental remediation systems for catalytic oxidation of toxins/removal of pollutants; iii) recyclable catalytic nanoparticle hydrogel composites for chemical synthesis and iv) composite hydrogel patches for cosmetic applications.

Control of the covalent and supramolecular interactions by synthetic design and prediction of the resultant properties in the nanoparticle-hydrogel composite are major areas to be developed in this emerging field. Such predictions upon experimental validation will form the foundation of design for the next generation nanoparticle-hydrogel composites with optimal properties for a desired application. In the coming years, such design of nanoparticle-hydrogel composites will not only result in advanced applications but will also steer the fundamental

understanding of material interactions, aiding computational prediction of properties of new composites from existing components.

PART 2. ANTIBACTERIAL PVA FILMS

2.1 BACKGROUND

2.1.1 Silver nanoparticles as antibacterial agents

The use of silver as antibacterial have been known for centuries. Given its noble nature ($E°_{Ag+/Ag}$ = 0.800 V), silver cannot be oxidized by water or strong acids unless some oxidizing agents or ligands able to bind Ag^+ cations are present. In aqueous colloidal solutions the Ag to Ag^+ oxidation of silver nanoparticles can be potentially promoted by the dissolved O_2, as the $O_2 + 4e^- + 4H^+ \rightleftharpoons 2H_2O$ semi-reaction has $E°$ = 1.23 V. However, in pure, neutral water the process is extremely slow and takes days to be effective,[16] unless strong ligands for Ag^+ are added.[17] Already since 19th century the antibacterial properties of metallic silver, for example in its use in containers for the disinfection of water, have been attributed to Ag ions,[18] that are released in small quantities, also due to the contact with biological material containing a variety of possible ligands for the metal. The toxicity of Ag^+ for microbial organisms is attributed to different mechanisms, such as the interaction with thiols and amines of proteins, with nucleic acids and with membranes.[19] This kind of mechanisms ensure a non-selective action, making silver a generic, wide range antimicrobial agent, that cannot be subjected to the development of specific resistance, as instead is happening for many bacterial strains presenting multi-drug resistance to molecular antibiotics.

For all these reasons, the use of Ag in nanometric dimensions as antibacterial is one of the most explored fields in the application of nanotechnologies, as documented by the almost 18000 publications found on the topic while writing this thesis (February 2022).[20] Silver nanoparticles (AgNP) used as antibacterial agents are typically spheres of 5-20 nm diameter.[19] While generally colloidal solutions are employed in the antibacterial studies,[19] many papers also present

AgNP monolayers as coatings for antibacterial surfaces,[21–24] AgNP dispersed in hydrogels[25] or embedded in solid films. Examples of applications for these material range from food packaging,[26,27] to water filtration,[28,29] and wound dressing.[30,31] In all these cases, the antibacterial action of AgNP is mainly due to their slow surface oxidation, giving a prolonged release of Ag^+ ions,[19] although an additional nanomechanical effect is sometimes observed, exerted by the disruptive contact of the high-energy AgNP surface with bacterial membranes.[22]

2.1.1.1 AgNP with pectin

The preparation of AgNP from $AgNO_3$ and pectin in a basic acqueous environment has been described by our research group,[32] with a recent variation on the salt precursor.[33] The reduction to Ag^0 proceeds thanks to the oxidation of the diol moiety of the galacturonic acid units of pectin, with consumption of hydroxide anions, as represented in Figure 2.
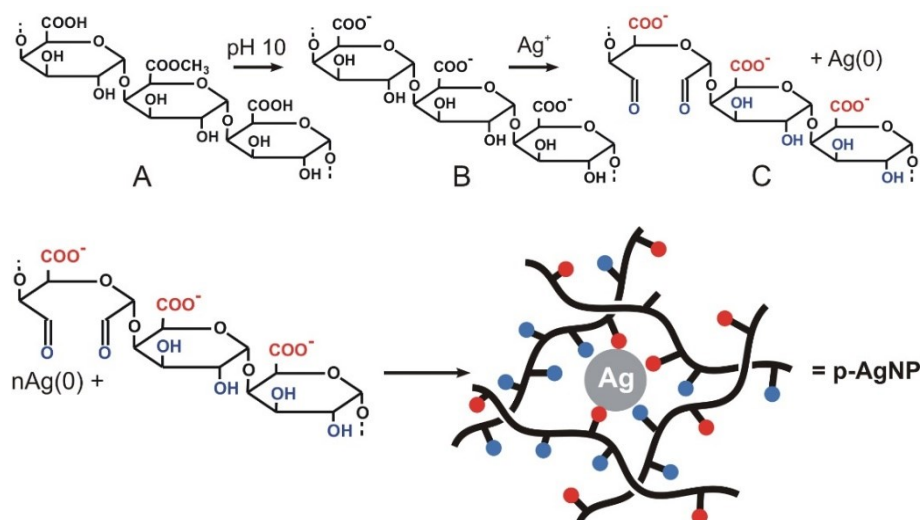
Figure 2 Scheme of the reaction involved in the formation of pectin-stabilized AgNP.
[32]

This synthesis allows a fast and reproducible preparation of spherical AgNP of 8.0(2) nm of diameter, with a ~ 100% reduction yield (residual Ag^+ < 0.8% of total Ag).[32,33] Under an established set of optimal conditions (1% w/w pectin in water, 1.0 mM $AgNO_3$ and a starting pH in the 10.5-11 range, at T = 60 °C), the galacturonic acid units of the pectin chains are in large excess with respect to Ag^+, thus preventing AgNP oxidation by O_2.[16,17,32] In addition, pectin can efficiently stabilize AgNP against aggregation.

This preparation exerted not only a strong antibacterial effect on planktonic cells of Gram-negative *E. coli* and Gram-positive *S. epidermidis* bacteria, but also a considerable killing action against pre-formed biofilms of both strains.[32,33] Moreover, pectin-coated AgNP demonstrated no significant cytotoxicity against human fibroblasts cells and even a promotion of their proliferation up to 130% with respect to the control (i.e. treatment with complete medium), holding good promises for their application in wound healing.

2.1.2 Microbicidal action of photothermal nanoparticles

Noble metals nanoparticles present intense absorption bands due to the phenomenon of Localized Surface Plasmon Resonance (LSPR).[34] Excitation of these bands, typically with a laser source, results in thermal relaxation, generating a local temperature increase.[35] Photothermally active nanoparticles in general find many potential uses in nanomedicine,[36] biosensing,[37] and solar energy technology.[38] In particular, they are intensively studied in cancer therapy for localized hyperthermal tumoral cell ablation and photothermally induced drug release.[39–42] Their application for novel quantitative biochemical analysis,[43] cell stimulation,[44] and bacterial eradication has also been exploited.[22]

Gold nanoparticles (AuNP) are commonly used for this purpose. Being the noble character of gold stronger than that of silver ($E°_{Au+/Au}$ = 1.83 V; $E°_{Au3+/Au}$ = 1.52 V), no oxidation is observed for AuNP colloidal solutions under a wide range of conditions, including all the physiological and bio-mimicking ones. Accordingly, AuNP do not release gold cations and differently from Ag nanoparticles do not exert intrinsic antibacterial action, although a poorly efficient membrane-disrupting contact effect is hypothesized. However, their photothermal properties can be exploited to exert an on-demand hyperthermal microbicidal action.[45]

At this regard, nanoparticles with non-spherical, anisotropic shapes (such as nanorods, nanostars, etc.) are particularly interesting, as their absorption bands due to longitudinal plasmon resonance fall in the near infrared (NIR) range.[46–49] This means that irradiation can be carried out with an intrinsically low energy radiation and inside the so-called first bio-transparent window (750-900 nm, Figure 3), a wavelength range in which water, blood, skin and muscles are less absorbing and allow significant laser beam penetration (some cm).[50]
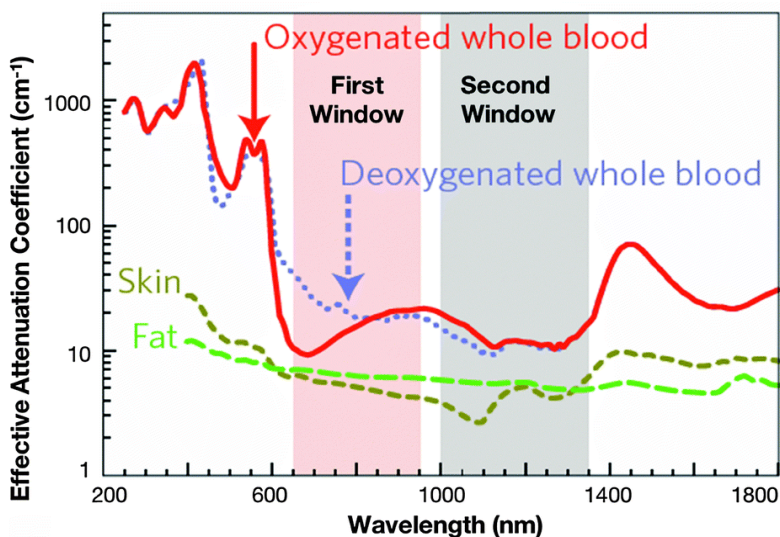
Figure 3 Absorption spectra of different biological tissues and fluids showing the first and second biological windows. [50]

This allows treatments of infected areas through tissues that avoid undesired hyperthermia of healthy tissues nearby, provided that suitable gold nanoparticles are localized in the relevant area. In this perspective, colloidal solutions of gold nanorods, for example, have proved to exert an efficient photothermal killing action against *S. aureus* and *Propionibacterium acnes* bacterial strains.[51]

However, the use of colloidal suspensions, with their intrinsic limitations in reusability and long-term stability, prevents the full-potential exploitation of photothermally active NP for biotechnological and biomedical applications. In addition, the relevant heat dissipation in solution, due to the thermal capacity of water, generally requires high irradiances to generate a significant photothermal response. The challenge seems therefore to develop lightweight materials with enhanced, long-lasting and controllable photothermal properties.

2.1.2.1 Gold nanostars

Gold nanostars are generally intended as nanoparticles in which two or more branches protrude from a spheroidal core[47] and this is the type of gold nanostars that have been used in this PhD research. However, also less simple shapes (e.g. nanourchins) and in general multibranched nanoparticles are named "nanostars" in the literature.[52]

The synthetic method used to obtain GNS with Triton X-100 was developed in our laboratory[53] and later employed by other groups.[54,55] This is a seed-growth process in aqueous solution, where the non-ionic surfactant Triton X-100 directs the growth of pre-formed small spherical AuNP (seeds) and eventually acts as GNS protecting agent, together with ascorbic acid (AA) as reducing agent, $HAuCl_4$ as gold precursor and $AgNO_3$ that is required in small quantities to help directing the anisotropic growth. These nano-objects present 2-6 sharp branches protruding

from the central core, giving two intense LSPR absorption bands falling in the 750 – 1100 nm and 1200 – 1600 nm wavelength ranges, respectively.[56] The morphology of these GNS, and in particular their aspect ratio, can be controlled by varying the synthetic parameters (such as AA, AgNO$_3$ and seeds concentration), allowing a fine tuning of the LSPR bands position, as can be noticed in Figure 4.
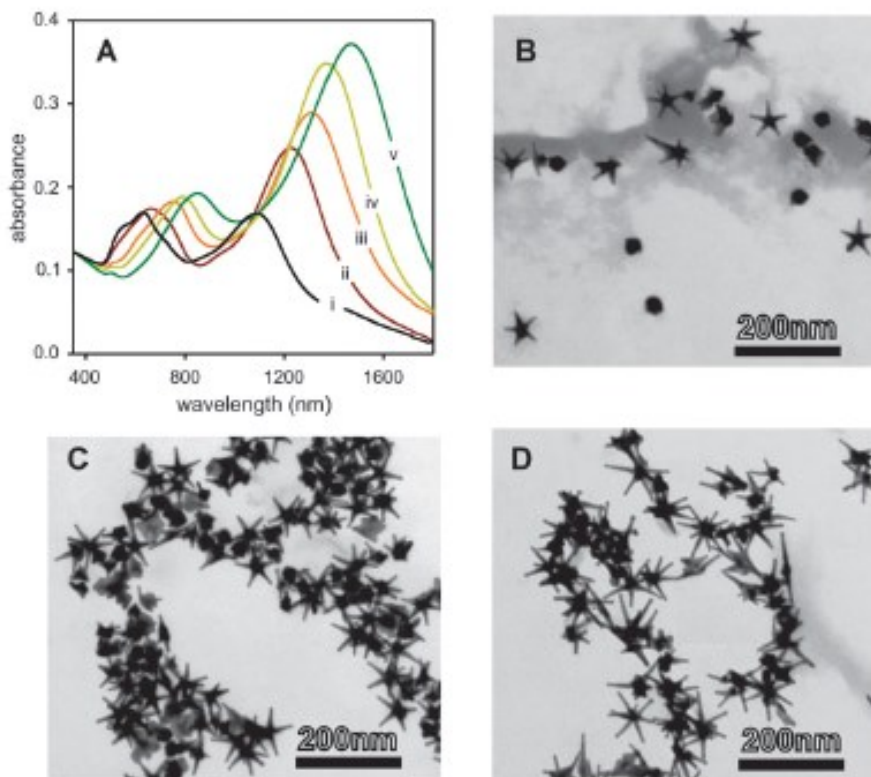
Figure 4 (A) Extinction spectra of GNS prepared with Triton X-100 at different reductant (AA) concentrations. (B), (C) and (D) TEM images from GNS solutions with corresponding spectra (i), (iii) and (v), respectively. [53]

Upon irradiation with a laser source matching the LSPR bands, GNS solutions show a steep temperature increase (ΔT), reaching a plateau at the equilibrium temperature. The entity of the observed plateau ΔT ultimately depends on the absorbance shown at the excitation wavelength.

2.1.3 Antibacterial nanocomposite materials

One of the best options to further extend the scope of applicability of antimicrobial nanoparticles is their combination with polymers to obtain composite materials that find their use in several fields such as medical devices, water treatment and food technology.[57] The development of polymeric antimicrobial materials is urged, for example, by the fact that a large part of hospital acquired infections (HAIs) are spread through contact with plastic-based surfaces, as in the case of catheters.[58] Infections are the main cause of biomaterial implant failure in modern medicine. This aspect is even more relevant in the light of the constant expansion of the polymer market in healthcare applications.

The use of antimicrobial polymers can offer different advantages, such as the enhancement of the efficacy and selectivity of existing antimicrobial agents, the extension of their lifetime and the reduction of their release and residual toxicity in the environment.[59,60]

The inclusion of nanoparticles with microbicidal activity can be achieved either by immobilization onto the surface of a bulk polymeric material or by incorporation into the polymer matrix. This second approach generally allows for more facile preparation and convenient utilization of the resulting composites. Anyway, the best strategy will always depend both on the final intended application and on the nature and physicochemical properties of the selected components to be combined.

2.1.3.1 Intrinsic antibacterial materials

Silver nanoparticles (AgNP) are the most used antimicrobial filler in polymeric nanocomposites. The design of Ag-based polymer nanocomposites aims at

providing protection for the AgNP along with control on the metal release for a sustained microbicidal action.

Research has mainly focused on the development of hydrogel composites where AgNP are *in situ* synthesized via the reduction of an Ag salt precursor, such as AgNO₃. In these cases, the polymer matrix can act as a nanoreactor for the formation of the NP.[57] For instance, swollen poly(acrylamide-co-acrylic acid) hydrogels have been used for the formation of AgNP of around 25–30 nm diameter. These nanocomposites demonstrated good antibacterial activity against *E. coli*, with a dependance on the size and the amount of the NP.[61] A variety of AgNP-embedded materials presenting antibacterial activity have been developed with this *in situ* approach from different polymers, such as poly(vinyl alcohol) (PVA),[62] poly(vinyl pyrrolidone) (PVP) and poly(acrylamide) (PAAm),[63] *N*-isopropylacrylamide (NIPAAm) and sodium acrylate.[64] AgNP have also been synthesized by reduction in water in the presence of poly(acrylates) of different molecular weights, showing the influence of the reduction method and the polymer chain length on the resulting NP. Antimicrobial textiles were then prepared by functionalizing cotton, wool and polyester samples with the colloidal suspensions.[65] Beside the described *in situ* approach, several nanocomposites have been prepared by mixing preformed particles with polymers.[60]

In recent years, the focus has moved to the use of natural polymers, which can act both as reducing agent and stabilizing agent for the NP.[66] For example, alginate was employed to prepare AgNP, that were further blended with varying amounts of chitosan. The resulting polyelectrolyte complexes were casted to obtain blended film displaying an excellent antibacterial activity.[67] The possibility to obtain biodegradable composite materials is interesting for the production of implantable

dressings, which can provide a prolonged disinfection without the need to remove the dressings.

2.1.3.2 Switchable antibacterial materials

The immobilization of photothermal nanoparticles on a solid substrate allows the preparation of materials showing an hyperthermal response upon irradiation that can be exploited against bacteria colonization of the functionalized surface. An example of such antibacterial composite has been prepared by coating an inert surface with a GNS monolayer, after the preliminary formation of a molecular SAM for the adhesion of the NP.[56,68] These surfaces do not show any intrinsic effect against planktonic bacteria or biofilms grown on them. However, laser treatment at a wavelength matching the LSPR absorption of the GNS (800 nm) generates a photothermal response that is capable of killing most of the planktonic cells as well as eradicating the biofilms. A 30-minutes irradiation is sufficient to reduce the viability of a biofilm grown from *S. aureus* on the functional surface.[68] Nonetheless, the incorporation of photothermally active nanoparticles into a polymeric matrix is a convenient alternative that allows the production of soft materials, with the additional advantages of a greater protection of the embedded NP and reduced cytotoxicity, plus the capability of a remote on-demand activation of an efficient photothermal action.[69]

Many examples of polymer-embedded photothermal NP have been reported too, such as hydrogel-embedded gold nanorods[70] or PDMS-embedded GNS[71]. PVA films with GNS embedded have been already obtained thanks to our active collaboration with two research groups at Milano-Bicocca and CNR-Pozzuoli.[72] The inclusion was possible after coating of the GNS with a thiol polyethylene glycol (HS-PEG). Photothermal antibacterial tests have been performed on *E. coli*,

finding a 50% decrease of the bacterial viability after 5 minutes of laser treatment at 1064 nm (matching the second LSPR band of the GNS). Results from control experiments on irradiated blank films (without GNS) and GNS-containing films without irradiation did not significantly differ from the reference, as expected. A more recent work explored the preparation of similar PVA-based materials by spray-coating instead of film casting.[73] In this case not only GNS, but also Prussian Blue nanoparticles (PBNP), a promising alternative component as photothermal additive, have been considered for the inclusion in the polymer matrix, giving noteworthy microbicidal results against both *P. aeruginosa* and *S. aureus*.

2.1.3.3 Combined antibacterial nanocomposites

The production of mixed materials possessing both an intrinsic and a photothermal on-demand microbicidal action is an essential advance in the production of efficient antibacterial devices. Indeed, the prolonged protection against bacterial infection given by AgNP is combined with the photothermal action exerted by AuNP, which can be switched on in case of more severe conditions, like the formation of a biofilm on the surface of an indwelling device or in a chronic wound. As mentioned above, employing LSPR bands in the bio-transparent window, this treatment can be in principle carried out through tissues and avoiding damages to the surrounding healthy areas.

However, the coexistence of the different types of NP has to be guaranteed in solution or in a solid material. This is not a trivial point given the different intrinsic stability[16,17] and required synthetic routes[24,46,68,74,75] for AgNP and AuNP. Moreover, the marked differences in shape, surface energy, oxidation potential and solubility between spherical AgNP of 5-20 nm diameter and bigger, non-spherical AuNP can

lead to interparticle Ostwald ripening processes[76] and underpotential Ag$^+$ deposition on gold[77], leading to Ag-promoted AuNP reshaping.[78,79]

One possible approach recently described is the formation of two separate monolayers of GNS and AgNP on top of each other, starting from a glass surface acting as a platform (see Figure 5, left).[80] The obtained material showed a marked antibacterial effect due to the spherical AgNP (d = 8 nm) grafted on top, plus a strong hyperthermal antibacterial effect when the LSPR band of the embedded GNS was excited with a 800 nm laser source. However, this layer-by-layer approach requires a time-consuming multistep procedure and a simpler, direct preparation would be welcome.
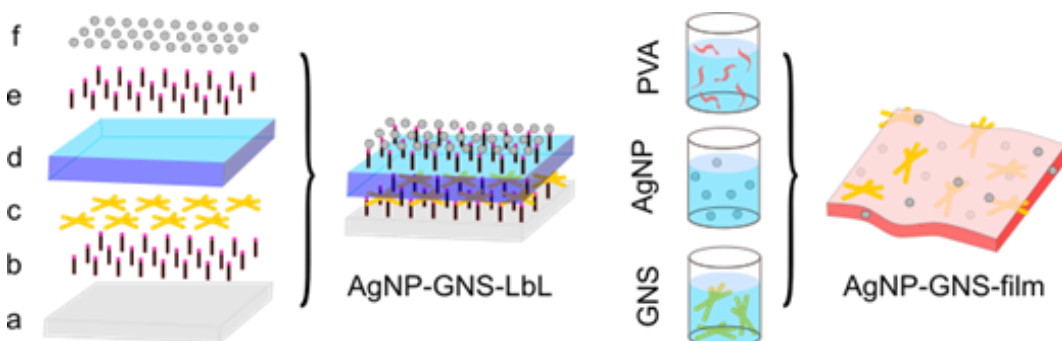
Figure 5 Left, layer-by-layer approach for the preparation of antibacterial glass slides with separate monolayers of GNS and AgNP, as described in ref. 77; right, single-step approach for the casting of PVA films with both NP, as described in this work (see below). [81]

Basing on these considerations, the first main part of my PhD research work focused on the preparation of polyvinyl alcohol (PVA) films containing both AgNP and photothermally active GNS. The aim was the facile production of stable functional nanocomposites, that could combine the intrinsic and switchable antibacterial actions as described above, possibly for their use in the treatment of wounds. Indeed, a straightforward procedure was adopted, demonstrating that this kind of films can be prepared in a single casting step, after mixing aqueous

solutions of the polymer with properly protected GNS and AgNP (see Figure 5, right).[81] PVA was chosen due to its low toxicity, biocompatibility, and easy film forming procedures.[82,83] Moreover, the strong hydrophilicity of PVA films is a potentially useful property for the capture of the exudate if used in wound healing processes.[84]

2.2 EXPERIMENTAL DETAILS

2.2.1 Materials and instrumentation

2.2.1.1 Reagents

Silver nitrate ACS reagent, ≥99.0%; Pectin from citrus peel (galacturonic acid ≥74.0 %, dried basis); Triton™ X-100 (laboratory grade); Gold(III) chloride solution 99.99% (30 wt. % in dilute HCl); Sodium borohydride ≥98.0%; L-Ascorbic acid ≥99.0%; poly(ethylene glycol) methyl ether thiol (HS-PEG-OMe, mw 2000); O-(3-Carboxypropyl)-O′-[2-(3-mercaptopropionylamino)ethyl]-polyethylene glycol (HS-PEG-COOH, mw 3000); poly(vinyl alcohol) Mw 89,000-98,000, 99+% hydrolyzed; poly(ethylene glycol) (mw 200); Citric acid ≥99.5%; sodium hydroxide ≥98%, pellets; nitric acid ≥65%; hydrochloric acid ≥37% have all been bought by Merck Life Sciences, Milano, Italy, and used without further purification.

2.2.1.2 Glassware pre-treatment

All the glassware used in the syntheses was pre-treated with *aqua regia* for 15 minutes and then washed three times with bidistilled water in an ultrasound bath for 5 minutes.

2.2.1.3 Instrumental procedures

Ultracentrifugation

Ultracentrifugation was carried out using the ultracentrifuge Hermle Z366 with polypropylene 10 mL tubes.

pH

Measurement of pH was carried out with a XS Instruments pH-meter (pH 50 model) with a Thermo Scientific Orion 91022 BNWP combined glass electrode.

Electrode calibration was carried out before measurements, with solutions buffered at pH = 4, pH = 7 and pH = 10.

UV-Vis-NIR spectroscopy

Absorption spectra were recorded on a Varian Cary 60 spectrophotometer, either in solution in 1 mm and 1 cm optical glass cuvettes or directly on films by means of a dedicated sample holder.

Transmission Electron Microscopy (TEM)

Colloidal solutions were diluted 10-100 times with bidistilled water and 10 μL were deposited on nickel grids (300 mesh) covered with a Parlodion membrane and dried in a desiccator. Images were taken using a JEOL JEM-1200 EX II 140 instrument with a 100 kV acceleration voltage.

Scanning Electron Microscopy (SEM)

Samples were sputtered with gold and observed with a Zeiss EVO MA10 instrument (Carl Zeiss, Oberkochen Germany). The images were acquired at high voltage (20 kV), in high vacuum, at room temperature and at different magnifications.

Thermograms

Samples were irradiated with an 808 nm laser source (Thorlabs L808P200 AlGaAs laser diode) with a beam waist of 1.0 cm and power tunable up to 200 mW. Thermal images were taken with a FLIR E40 thermal camera with FLIR Tools+ dedicated software for data acquisition and analysis. For each sample a region of interest (ROI) was defined, comprising the laser-irradiated area, and the maximum temperature was determined for each thermal image inside the ROI (±0.1 °C accuracy). In a typical experiment thermal images were acquired at 1 fps rate for 60-240 seconds.

Determination of Ag and Au by ICP-OES spectroscopy

90 mg portions of the films were suspended in 3.0 mL of bidistilled water in a stoppered vial and incubated at 37 °C for 1, 5 and 24 hours. The "refresh+24 h" data were obtained by removing the films from vials after 24 h and, after quick washing, dipping them in 3.0 mL of "fresh" bidistilled water for further 24 h. Then, 1.0 mL of the resulting solutions was collected, treated with 1.0 mL of *aqua regia* and allowed to react for 15 minutes. After a further addition of 3.0 mL of bidistilled water the samples were analyzed by Inductively Coupled Plasma Optical Emission Spectroscopy (ICP-OES) on a Perkin Elmer Optima 3300 DV instrument.

Film thickness

Average film thickness was determined by 10 measurements on different points of a same film sample with a digital micrometer (Neoteck).

Tensile tests

Mechanical properties of films were assessed by means of a TA.XT plus Texture Analyzer (Stable Micro Systems, Godalming, UK), equipped with a 5 kg load cell. Before testing, film thickness was measured by means of Sicutool 3955 G-50 (Sicutool, Milan, Italy) apparatus. Each film was cut in 1×3 cm strips and then clamped on A/TG tensile grips probe; an initial distance of 1 cm between the grips was set. The upper grip was raised at a constant speed of 5 mm/s up to a distance of 30 mm, corresponding to 300% elongation. Maximum deformation force (F_{max}), forces at different deformations (F50, F100, F150 and F200 at 50%, 100%, 150% and 200% elongation, respectively) and deformation work (W_{max}) were measured.

2.2.2 Nanoparticles preparation

All solutions were prepared with bidistilled water, if not stated otherwise.

2.2.2.1 pAgNP synthesis

Pectin-coated AgNP were prepared according to a procedure previously described by our research group.[32] Briefly, 0.3 g of pectin from citrus peel were dissolved in 30 mL of bidistilled water by stirring at 60 °C. When dissolution was complete, 1.0 mL of 0.03 M $AgNO_3$ was added, quickly followed by 3.0 mL of a standard 0.5 M NaOH aqueous solution. The solution was kept stirring at 60 °C for 14 h. The resulting yellow-orange colloid has a pH between 10.5 and 11.4, that was adjusted to 7.0-7.5 by slowly adding 0.1 M HNO_3.

2.2.2.2 GNS synthesis

The preparation of Au nanostars was carried out according to a seed-growth method developed by our group.[53] First, a seed solution was obtained by mixing 5.0 mL of 0.2 M Triton X-100 with 5.0 mL of 0.5 mM $HAuCl_4$ and then quickly adding 600 μL of ice-cooled 0.01 M $NaBH_4$. The resulting light orange solution was kept in an ice bath and used within 1 hour. For the growth, 50 mL of 0.2 M Triton X-100 were put in a 250 mL flask under magnetic stirring at room temperature and then the following additions were made in a fast and sequential fashion: 2.5 mL $AgNO_3$ 4 mM, 50 mL $HAuCl_4$ 1 mM, 1.7 mL ascorbic acid 78.8 mM and finally 120 μL of a freshly prepared seed solution. The solution quickly turned from pale yellow to colorless and, after the last addition, to violet and eventually blue-black color, at which point stirring was stopped. However, the growing process was allowed to proceed and considered complete after 2 hours.

2.2.2.3 GNS coating and purification

GNS obtained as described above were then coated with HS-PEG (mw 2000) or HS-PEG-COOH (mw 3000). Respectively, 4.0 mg or 6.0 mg of the thiols were dissolved in 2.0 mL of bidistilled water and then added to the freshly prepared

gold colloids and allowed to react for at least 3 hours at room temperature. After that, pegylated GNS were purified by ultracentrifugation at 13000 rpm (15870 rcf) for 25 min. The colorless supernatant was discarded and each pellet redissolved in 10 mL of fresh water. The procedure was repeated three times, with the aim of removing all the surfactant and other subproducts from the synthesis, but after the last cycle the pellets were redissolved in a total volume of 3 mL to obtain concentrated GNS solutions.

2.2.3 Film production

Films were prepared by an established procedure with slight modifications.[85] 10 mL of 6% w/w PVA solution were prepared by dissolving the polymer in water at 90 °C. The solution was then allowed to cool down to room temperature and 66.0 mg of PEG200 were added. After stirring for 1 hour, the following additions were made, alternatively:

a) nothing → **film-blank**;

b) 1.0 mL of 1% w/w pectin solution → **film-pec**;

c) 1.0 mL of pAgNP → **film-Ag**;

d) 0.5 mL of concentrated GNS@PEG → **film-GNS**;

e) 1.0 mL of pAgNP and 0.5 mL concentrated GNS@PEG → **filmMIX-Ag/GNS**;

f) 0.5 mL of concentrated GNS@PEG-C → **film-GNS-C**;

g) 1.0 mL of AgNP and 0.5 mL concentrated GNS@PEG-C → **filmMIX-Ag/GNS-C**

After stirring for further 3 hours, only for cases a) – e) 66.0 mg citric acid were added and allowed to solubilize. This was not added in cases f) and g), where GNS are coated with HS-PEG-COOH, as the carboxylated particles can act themselves

as cross-linking agent. Finally, all the film-forming solutions were casted in 9 cm diameter Petri dishes, treated in an oven at 130 °C for 5 minutes and then allowed to dry at RT for 4 days, after which time the final films can be easily peeled off and are ready to use.

2.2.4 Microbiological experiments

2.2.4.1 Antimicrobial activity on planktonic cells

Staphylococcus aureus ATCC 6538 and Escherichia coli ATCC 10356 were used (ThermoFisher Diagnostic S.P.A, Italy). Tryptone soya Agar (TSA) and tryptone soya broth (TSB) were purchased from Oxoid (Basingstoke, UK).

Determination of microbicidal effect in suspensions

Bacteria were grown overnight in TSB at 37 °C. The bacteria cultures were centrifuged at 2000 rpm for 20 minutes to separate cells from broth and then suspended in phosphate buffer saline (PBS, pH 7.3). The suspension was diluted to adjust the number of cells to $1 \times 10^7 - 1 \times 10^8$ CFU/mL. A portion of each film at 30 mg/mL concentration was added to the microorganisms suspensions. For each microorganism used, a suspension was prepared in PBS without PVA films and used as control. Bacterial suspensions were incubated at 37 °C. Viable microbial counts were evaluated after contact for 5 and 24 hours with PVA films and in control suspensions; bacterial colonies were enumerated in Tryptone Soya Agar after incubation at 37 °C for 24 h. The microbicidal effect (ME value) was calculated for each test organism and contact time according to the following equation:[86]

$$ME = \log N_C - \log N_A \qquad (1)$$

where N_C is the number of CFU of the control microbial suspension and N_A is the number of CFU of the microbial suspension in presence of the PVA film.

Determination of film contact effect

Microbial suspensions were filtered with an initial inoculum of approximately 1-2 × 10^7 CFU/mL on filter membranes of cellulose acetate with a porosity of 0.22 μm. The membranes were then deposited on Petri plates containing TSA, suitable for the growth of microorganisms selected. The filter membranes were covered with PVA films for 5 and 24 hours contact times. Similarly, plates were prepared containing membrane filters without PVA films (control). After contact, the filter membranes were recovered, washed by suspending them in sterile water with a standardized method and at the end of the washing procedure, dilutions of the microbial suspensions were made to determine the microbial content with subsequent plating in TSA in order to count the viable cells and calculate the contact, apparent microbicidal effect (ME) as:

$$ME = \log N_C - \log N_d \tag{2}$$

where N_C is the number of colonies forming unit (CFU) of the control and N_d is the number of CFU in the cases of contact with the films.

2.2.4.2 Photothermal antibacterial activity

Escherichia coli MG1655 and Staphylococcus aureus ATCC 6538P strains were routinely grown in LB (Bacto tryptone 10 g/L; yeast extract 5 g/L; NaCl 10 g/L) (Difco; Franklin Lakes, NJ, USA) agar plates, incubating at 37 °C. For antibacterial effect assessment a single bacterial colony was inoculated in 5 mL of liquid LB broth and incubated at 37 °C under aeration for 16-18 hours. Following incubation, the bacterial culture was diluted 1:10 in the same medium to adjust the bacterial concentration to approximately 1-5 × 10^8 CFU/mL.

The followed method has been already described by Borzenkov and coworkers.[87] Briefly, films were cut to fit laser beam size (~1 cm diameter) and placed in Petri dishes with a cover glass bottom (MatTek, Ashland, MA, USA). An amount of 20 µL of diluted bacterial suspension was inoculated on the top of the glasses, and the films were gently air-dried under a laminar flow hood. The films were irradiated with 800 nm laser light (Mai Tai, Spectra-Physics), 0.30 W/cm^2 irradiance on the sample plane and different durations of irradiation (0, 15, 30 min). Irradiated and non-irradiated (control) samples were stained with Film Tracer Live/Dead viability kit (L10316, Invitrogen, Carlsbad, CA, USA) based on the use of the SYTO® 9 and propidium iodide stains mixture in an appropriate concentration ratio (0.167 or 3.34:20) to ensure that bacteria with intact membranes (live) stain fluorescent green (SYTO® 9) whereas propidium iodide stains red only bacteria with damaged membranes (dead). The stained samples were analyzed with a Leica SP5 TCS confocal microscope using a 20× dry objective (HC PL FLUOTAR 20× 0.5, dry, Leica, Wetzlar, Germany). At least four z-stacks of raster scanned images were collected from three distant regions in the film by using the 488 nm argon ion laser emission in both spectral intervals (510–580 nm and 590–700 nm, where the bleed through of the green dye at the concentration used for the staining experiments is negligible). Each image has been acquired with either 512 × 512 or 1024 × 1024 pixels and 400 Hz of line scan frequency, with fields of view ranging from 64 µm × 64 µm to 110 µm × 110 µm. Z-stacks were acquired by taking planes every 1.0 µm. The images have been analyzed by employing a threshold filter [Fiji, version 2.0.0-rc-43/1.52n, NIH] and measuring the percent area in the red (A_{dead}) and green (A_{live}) channels.

2.2.4.3 Biocompatibility assays

Cytotoxicity test

Dried films (1 cm²) were soaked in 2 mL of complete culture medium (CM) at 37 °C for 24 h under mild stirring (60 rpm). After 24 h, the "conditioned" medium was recovered and put in contact with a monolayer of Normal Human Dermal Fibroblasts, NHDF (PromoCell GmbH, Heidelberg, Germany). Briefly, cells were seeded on 96-well plates (3.5×10^4 cells in 200 μL of CM/well) and incubated (37 °C and 5% CO_2) for 24 hours in order to reach semi-confluence. 200 μL of each sample (conditioned medium) were put in contact for 24 hours with cells; CM was used as reference. After incubation, an MTT assay was performed. Briefly, samples and reference were removed from the 96-well plate and cell monolayers were washed with PBS; subsequently, 50 μL of MTT 7.5 μM in 100 μL of DMEM without phenol red were added to each well and incubated for 3 hours (37 °C and 5% CO_2). Finally, 100 μL of DMSO, used as solubilization agent, was added to each well. In order to promote the complete dissolution of formazan crystals, obtained from MTT dye reduction by mitochondrial dehydrogenases of alive cells, the solution absorbance was measured by means of an iMark® Microplate reader (Bio-Rad Laboratories S.r.l.) at a wavelength of 570 nm and 690 nm (reference wavelength) after 60 s of mild shaking. Results were expressed as % cell viability by normalizing the absorbance measured after contact with each sample with that measured for CM. Twelve replicates were performed for each sample.

Fibroblasts proliferation test

Dried films (1 cm2) were soaked in 2 mL of medium without serum (M w/S) at 37 °C for 24 h under mild stirring (60 rpm). After 24 h, the "conditioned" medium was recovered and put in contact with a fibroblast monolayer. The capability of each "conditioned" medium to promote NHDF proliferation was evaluated. Cells

were seeded on 96-well plates (2 ×104 cells in 50 µl of CM/well) and immediately put in contact with 200 µL of each sample for 24 h. CM and medium without serum (M w/s) were used as references. A MTT assay was performed as previously described.

2.3 RESULTS AND DISCUSSION

2.3.1 Nanoparticle synthesis and characterization

2.3.1.1 pAgNP

Colloidal solutions of AgNP were prepared following a procedure introduced by our group[32], using an established set of optimal conditions as described in 2.1.1.1. Upon addition of NaOH to a solution containing $AgNO_3$ and excess pectin, the solution immediately turns to a yellow-brown colour, indicating the fast formation of the AgNP, given by the reduction of Ag^+ by pectin, that proceeds only in basic conditions.

The obtained colloids present a sharp LSPR absorption band centered at 412 nm, typical of small, spherical AgNP.[88–90] The absorption maximum and the band shape are nicely reproducible, as can be seen in Figure 6 (spectra obtained from 3 different syntheses).
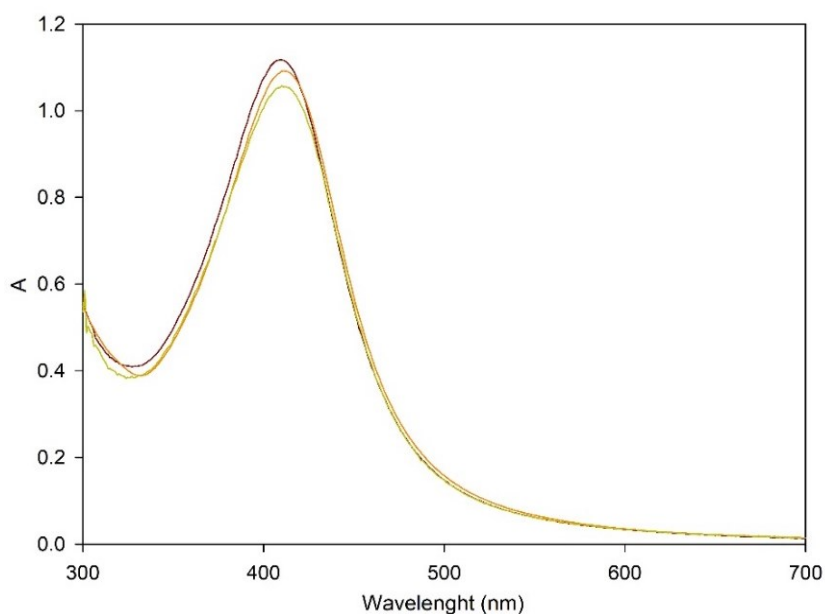
Figure 6 Extinction spectra of different pAgNP colloids.

Also, the Ag nanoparticles shape and dimensions are well reproducible, as we always obtain spheres with d = 8(±2) nm. The as-prepared solutions had a pH between 10.5 and 11.4, that was adjusted to 7.0-7.5 with 0.1 M HNO_3 in order to increase the stability of pAgNP when mixed with GNS (see 2.3.1.3).

2.3.1.2 GNS

Gold nanostars were also prepared according to the method already developed in our laboratory.[56] This seed-growth synthesis exploits the non-ionic surfactant Triton X-100 to direct the anisotropic growth of small, spherical Au seeds. The procedure, as described in 2.2.2.2, yields a blue-grey colloidal solution that presents multiple LSPR absorption bands. Figure 7 shows the extinction spectra in the 300-1100 nm range of three GNS colloidal solutions used in this research. The intense peak with λ_{max} between 790 and 850 nm is associated to the longitudinal plasmonic resonance of the GNS branches.
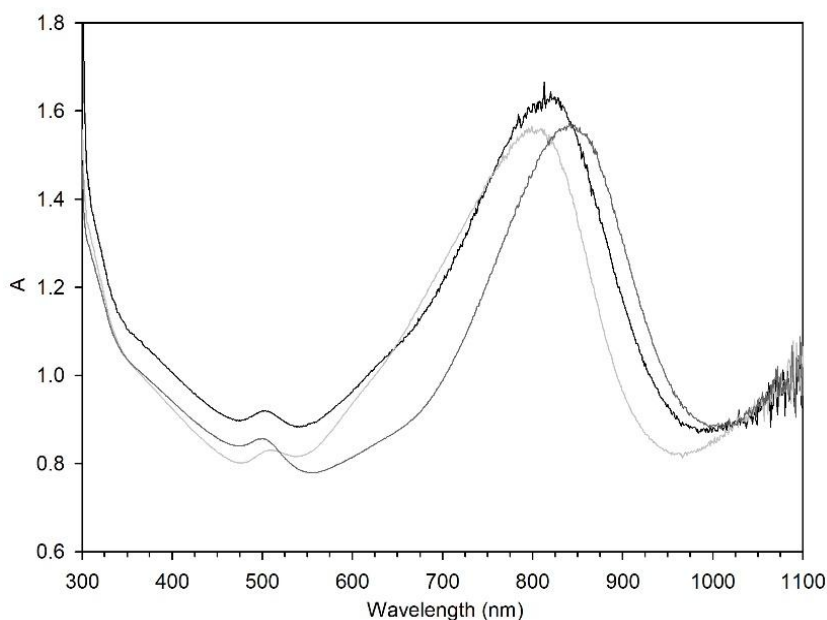
Figure 7 Extinction spectra of different GNS colloids

A second peak falls above 1100 nm, thus out of the range of the instrument used. This is related to the tip-to-tip oscillation of the conduction electrons, generated by the coupling of the longitudinal resonances in the case of aligned branches. The smaller peak at 520 nm is due to spherical by-products and to the transversal oscillation of the electrons in the branches, typical of all elongated gold nanoparticles.[46,91] A weak shoulder at 650 nm can also be noticed, that is attributed to a minor population of partially grown nano-objects.

As it can be seen in Figure 7, reproducibility is only partial, as typical of the complex mixtures of gold nanostars obtained with this type of synthesis. The GNS obtained under the described synthetic conditions are mainly 5- or 6-branched, with a tip-to-tip maximum distance of around 100 nm (see Figure 8). However, despite the complex spectra and the related manifold populations, the synthesized GNS are suitable for the aim of this work, as they present a strong, large LSPR absorption in the bio-transparent window, with the maximum of the band falling close to the typical NIR laser source wavelength of 808 nm.

Once grown, GNS need to be coated with a thiolated polyethylene glycol (HS-PEG). As a matter of fact, "nude", as obtained GNS do not resist to ultracentrifugation (that leads to aggregation). Grafting of PEG molecules on their surface allows instead GNS to withstand repeated ultracentrifugation cycles that are required to purify the colloids, in particular to remove the cytotoxic Triton X-100 surfactant that is used in excess in the growth process, and be then readily redispersed.[92] Moreover, with this procedure concentrated colloids can be obtained by simply adding the desired small volume of dispersant to the pellet obtained after the final ultracentrifugation step.

Both a "plain" thiol PEG (methoxy-terminated, mw 2000) and an α,ω-bifunctional HS-PEG-COOH (mw 3000) were used in this work. PEG coating of GNS is also

intended to improve their biocompatibility and stability in complex media, in particular upon mixing with pAgNP, to avoid a fast reshaping.[81]

2.3.1.3 pAgNP/GNS mixtures

Solutions containing both the pre-synthesized nanoparticles were prepared by mixing pectin-coated AgNP at neutral pH and concentrated PEGylated GNS. A standard volume ratio AgNP:GNS 2:1 was adopted as it gave a similar intensity for the two relative LSPR absorbances.[81] A representative spectrum of the resulting deep green mixtures is shown in Figure 8, together with TEM images obtained from this solutions, where both types of nano-objects are recognizable.
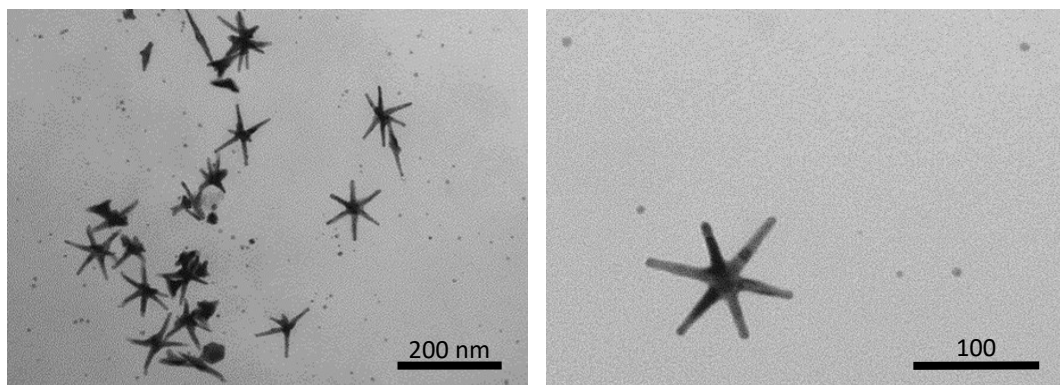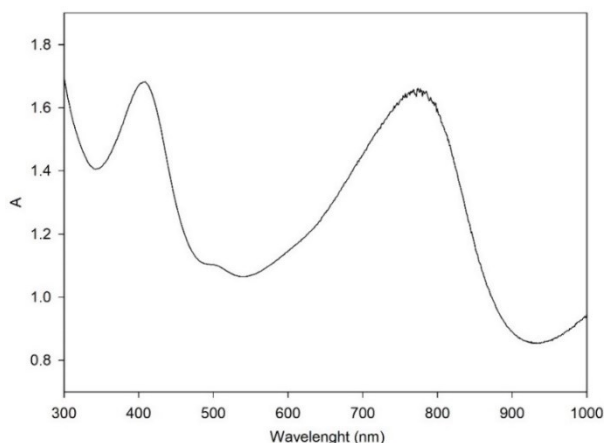
Figure 8 Extinction spectrum of a typical pAgNP/GNS-PEG 2:1 standard mixture (top); TEM images obtained from the mixed solution at different magnifications (bottom)

The pH of the silver colloids must be neutralized before mixing with GNS to avoid AgNP consumption and GNS reshaping in the short run. Indeed, a decrease of the AgNP LPSR band has been noticed on a 1-7 days range, with the simultaneous blue shift of the GNS NIR band, when using as-prepared pAgNP (i.e. with basic pH) in the mixture.[81] This could be due to the slow reduction of the equilibrium concentration of Ag+ from pAgNP (10 ppm) on the highest-energy portions of the GNS surface, a process that would be enabled by the presence of excess pectin in a basic environment.[32] To highlight the importance of pectin coating and pH regulation, we checked the stability of mixed solutions containing standard citrate-coated AgNP (d = 7-8 nm)[24,75]. The complete disappearance of the plasmon band at 394 nm was observed in 6 hours (Figure 9).
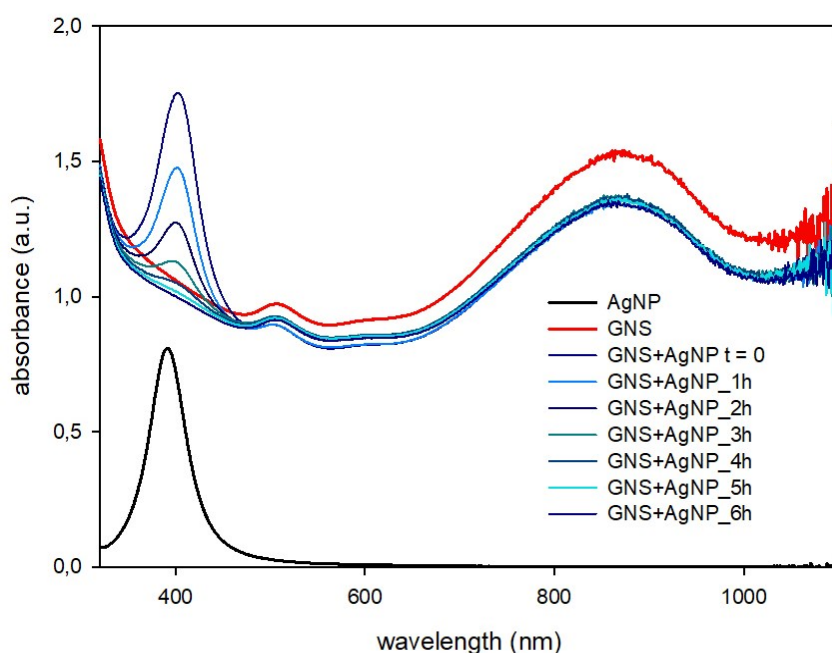
Figure 9 Extinction spectra of a mixture of citrate-coated AgNP (ref. 10,40) and GNS, recorded upon mixing and then every hour for 6h. Reference spectra for the two isolated preparations (black line and red line, respectively) are also reported.

2.3.2 PVA films

2.3.2.1 Film casting

Films were prepared by casting a 6% w/w aqueous solution of PVA (mw 89000-98000) containing also a short chain PEG as plasticizer (mw 200, 11% w/w relative to PVA), following the procedure described in 2.2.3. The crosslinking of the polymer relies on the ester formation between the hydroxyl groups of the PVA and the carboxylic functions of a crosslinking agent – either citric acid or the HS-PEG-COOH grafted on GNS (Figure 10).[93]
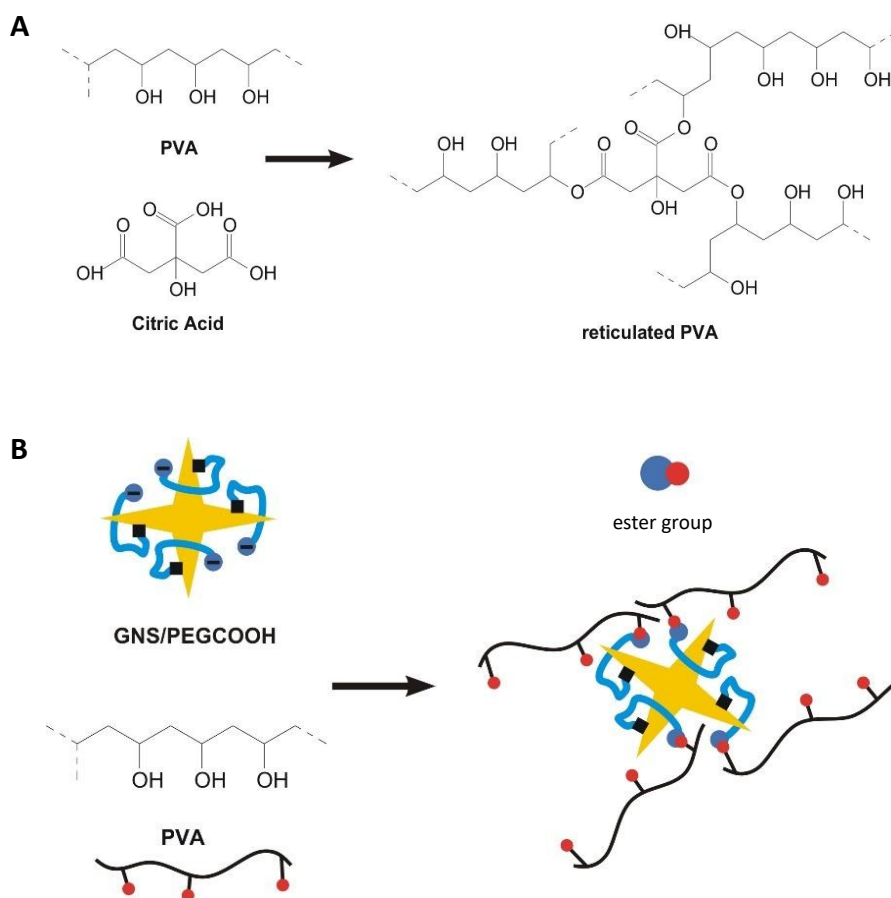
Figure 10 Crosslinking schemes of PVA with (A) citric acid and (B) GNS-PEG-COOH

Small volumes of 1% w/w pectin, pAgNP, GNS-PEG and/or GNS-PEG-COOH aqueous solutions were added to the film-forming mixtures (Figure 11), giving the set of entries listed in Table 1. Citric acid (CA, 11% w/w relative to PVA) was added in all cases except when GNS-PEG-COOH are present. After casting and drying, films were peeled off from the Petri dishes and were ready for further characterization.
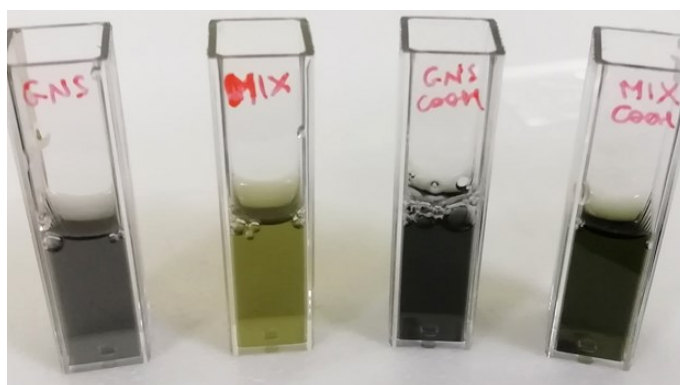
Figure 11 Picture of film-forming solutions for, from left to right, film-GNS, filmMIX-Ag/GNS, film-GNS-C and filmMIX-Ag/GNS-C.

Knowing the amount of all the solid components added, the approximate total mass of the prepared film samples can be calculated, as well as the total content of Ag and Au, from the concentrations of the two metals in the colloidal solutions (the relevant data and mass film composition are reported in Table 1). The actual weights of the dried films show that the water content is in all cases < 2% of the total film mass.

As it can be also noticed, the total noble metal content is always lower than 1 mg; in particular, the content of silver, a potentially toxic element, is extremely low (< 0.03% w/w). It is worth to recall that some Ag comes also from the GNS colloids, as it takes part in the nanostars growth.

Table 1 Composition of the casting solutions, total metal content and weight of the resulting films

	Pectin[1]	AgNP[2]	GNS-PEG[3]	GNS-PEG-COOH[4]	CA[5]	Total Ag (mol; µg)	Total Au (mol; µg)	Calc. film mass[6] (mg)	Dry film mass[7] (mg)
film-blank	-	-	-	-	✓	-	-	732	731(5)
film-pec	1.0	-	-	-	✓	-	-	742	740(8)
film-Ag	-	1.0	-	-	✓	8.82×10^{-7} 95.1	-	742	748(10)
film-GNS	-	-	0.5	-	✓	9.7×10^{-7} 104	4.34×10^{-6} 855	733	728(12)
film-GNS-C	-	-	-	0.5	-	9.3×10^{-7} 99	4.26×10^{-6} 840	667	660(11)
filmMIX-Ag/GNS	-	1.0	0.5	-	✓	1.85×10^{-6} 199	4.34×10^{-6} 855	743	746(9)
filmMIX-Ag/GNS-C	-	1.0	-	0.5	-	1.81×10^{-6} 194	4.26×10^{-6} 840	677	686(8)

[1] *mL of 1% w/w pectin solution added to 10 mL of PVA solution;* [2] *mL of pAgNP solution added to 10 mL of PVA solution;* [3] *mL of concentrated GNS-PEG solution added to 10 mL of PVA solution;* [4] *same, for GNS-PEG-COOH;* [5] *the ✓ symbol indicates the presence of citric acid in the solution (11% w/w relative to PVA);* [6] *sum of the mass of all solid components added;* [7] *actual film weight after preparation and 4 days drying at RT (s.d. in parentheses).*

Effects of PVA inclusion on NP

When GNS-PEG are mixed in the PVA solution their spectral features are somehow affected. Indeed, a red shift along with an intensity decrease of the NIR LSPR band was observed right after the addition, both with and without AgNP present (Figure 12A-B).
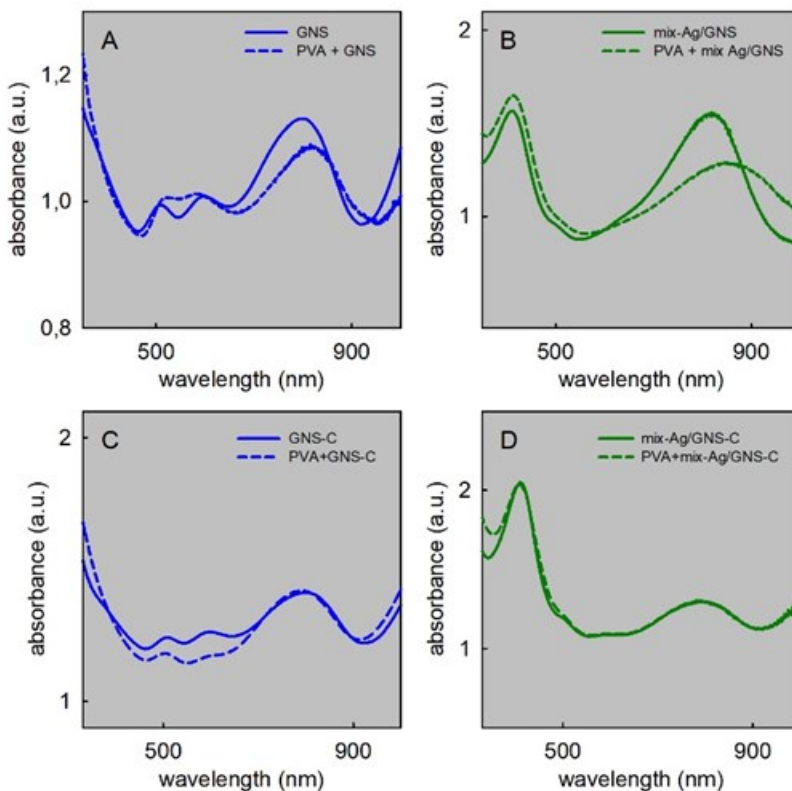
Figure 12 Extinction spectra of nanoparticles before (solid lines) and after (dashed lines) addition in PVA. (A) GNS-PEG; (B) pAgNP/GNS-PEG mixture; (C) GNS-PEG-COOH; (D) pAgNP/GNS-PEG-COOH mixture.

The absorption of the latter does not change significantly instead, as it can also be noticed in Figure 13, where pAgNP spectra in the presence of PVA, PVA + PEG200 and PVA + PEG200 + citric acid are reported. Absorption spectra of all the other components of the films except GNS have been recorded as well for comparison (Figure 13).

It is interesting to notice that, when GNS-PEG-COOH are used instead of GNS-PEG, both alone and in the mixed solutions with AgNP, the spectral changes described above do not take place (Figure 12C-D). A possible explanation could be that, in the case of GNS-PEG, portions of the PVA chains interact directly with the

GNS surface; indeed, it has been already observed how the surface of HS-PEG-coated GNS is still accessible to different molecular species.[94] In that case, the higher PVA refractive index (1.4748) compared with that of water (1.33) and the high sensitivity of the NIR bands of GNS to refractive index changes[74] would account for the observed changes. Conversely, the presence of carboxylic functions on the coating would explain the absence of a band shift in the case of GNS-PEG-COOH, since the crosslinking reaction can prevent the direct contact of PVA with the gold surface. Although the full reticulation is not a fast process, it is reasonable to think that the condensation of the hydroxyl groups of PVA with the carboxylate functions on the GNS starts immediately, anchoring the polymer on the far end of the PEG molecules. The hypothesis of a fast esterification is corroborated by the presence of a large excess (500,000-fold) of the functional groups of the PVA involved in the reaction compared to those from HS-PEG-COOH in the conditions used here, which can be estimated from the published data of % weight of HS-PEG on these GNS (~10%).[68]
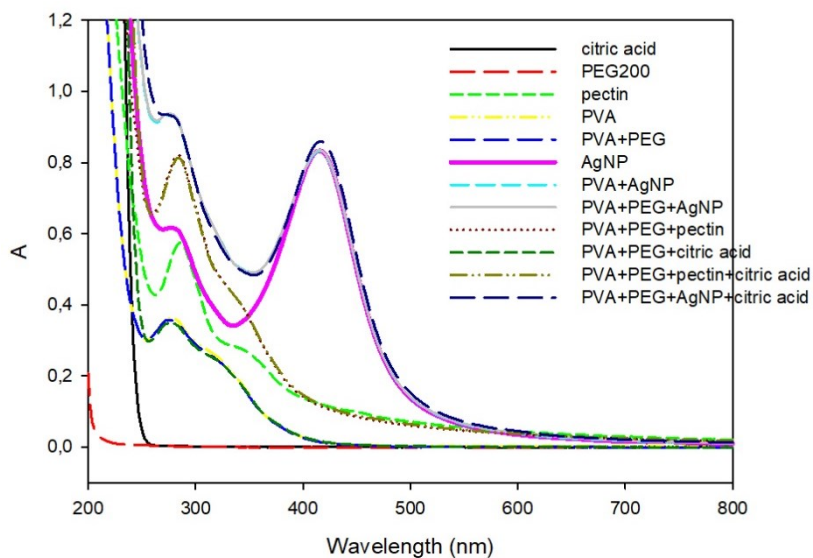
Figure 13 Absorption spectra of all the components of the films except GNS and their combinations.

2.3.2.2 Film characterization
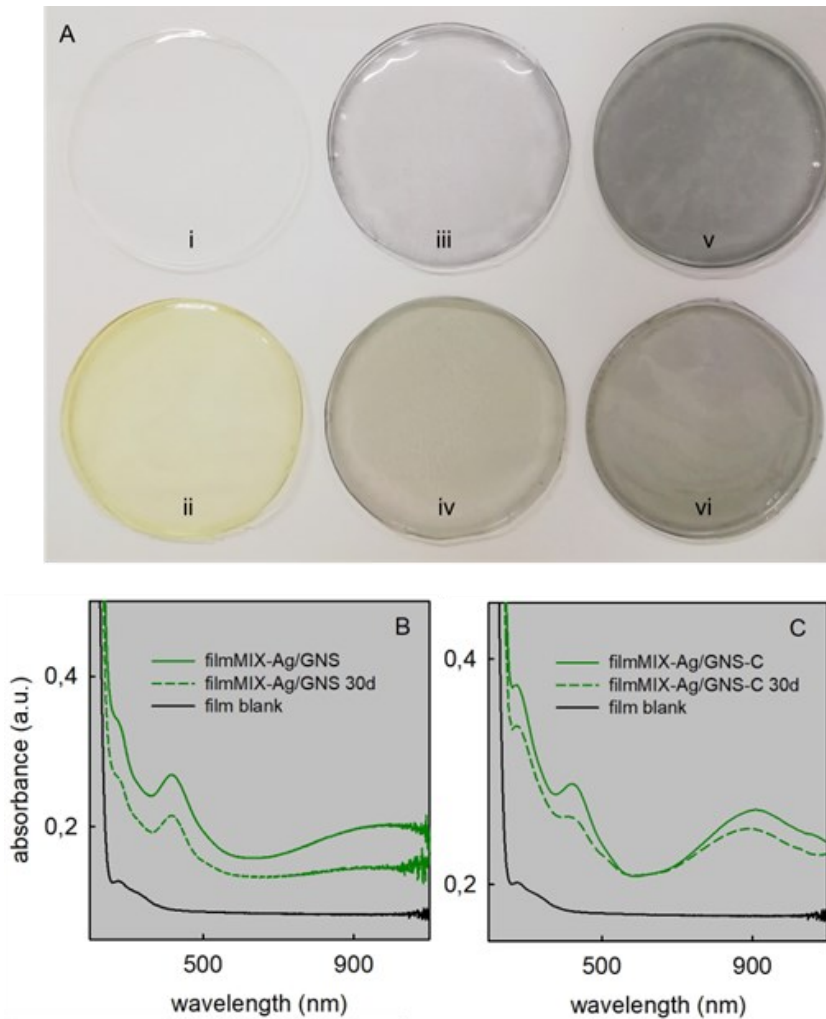
Figure 14 (A) Picture of different films i) film-blank; ii) film-Ag: iii) film-GNS; iv) filmMIX-Ag/GNS; v) film-GNS-C; vi) filmMIX-Ag/GNS-C. (B) extinction spectra of freshly prepared (green solid line) and 30-days (green dashed line) aged filmMIX-Ag/GNS. (C) same, for filmMIX-Ag/GNS-C. Spectrum of film-blank (black solid line) is shown for comparison.

The visual appearance of the obtained films is displayed in Figure 14A. They are transparent, allowing excellent light transmission, so that the absorption bands of the included nanoparticles can be easily observed with a spectrophotometer (Figure 14B-C).

All the films retain the color of the relative colloids used in the preparation. As expected, films containing both AgNP and GNS have a dark green color. However, samples containing GNS-PEG (**film-GNS** and **filmMIX-Ag/GNS**) present a fainter color compared to those prepared with GNS-PEG-COOH (**film-GNS-C** and **filmMIX-Ag/GNS-C**), despite the equivalent concentration of GNS. This observation is confirmed by extinction spectra, as the GNS LSPR band in freshly prepared films is weaker for films with GNS-PEG, as can be noticed in Figure 14B-C for the case of the mixed films.

The stability of the nanoparticles in the prepared films has also been investigated by absorption spectroscopy. After 30 days at room temperature, films containing GNS-PEG present a low, almost flat NIR LSPR band, while the same is only slightly diminished when GNS-PEG-COOH are present (see dashed spectra in Figure 14B and C for the cases of **filmMIX-Ag/GNS** and **filmMIX-Ag/GNS-C**, respectively). Instead, the AgNP LSPR band in **film-Ag** remains practically unchanged after the same ageing time. The modifications in the films containing nanostars could be attributed to a residual mobility of the GNS in the PVA matrix and to the tendency of PEG-coated gold nano-objects to segregate in hybrid materials, a process that has been already observed in the laboratory where I worked for spherical Au nanoparticles.[95] Segregation leads to short interparticle distances, that in turn cause plasmon hybridization and band flattening.[96–98] On the other hand, the fact that GNS-PEG-COOH act as cross-linking agents drastically decrease the mobility of the particles in the polymer, preventing segregation. From these results, **film-GNS-C** and **filmMIX-Ag/GNS-C** appear as better candidates in the view of obtaining stable photothermal antibacterial materials with intense absorption in the NIR range.

While the average thickness of all the films obtained with citric acid as cross-linker are similar (87-100 μm range), the samples containing GNS-PEG-COOH are thinner, suggesting a more compact structure when the nanostars are directly involved in cross-linking (Table 2).

Table 2 Average thickness (s.d.) of the different types of films

Film sample	Thickness (μm)
film-blank	100(3)
film-pec	90(4)
film-Ag	87(3)
film-GNS	99(2)
filmMIX-Ag/GNS	93(5)
film-GNS-C	68(4)
filmMIX-Ag/GNS-C	65(3)

Mechanical properties

Tensile strength tests on the films prove that all the samples can be stretched up to 3 times their original length without losing their integrity. Indeed, stress vs. strain profiles reported in Figure 15A show an increase in the normalized force on increasing strain up to 200% without breakdown of the film structure. The inclusion of AgNP and/or GNS-PEG does not significantly affect the mechanical properties and the ultimate resistance of the derived films. On the contrary, the presence of GNS-PEG-COOH correlates with an increase of the maximum force. This improvement in the mechanical resistance of films containing GNS-PEG-COOH with respect to those cross-linked with citric acid is confirmed by the

normalized tensile work values, calculated as the area under the force vs. deformation distance curve (Figure 15B).
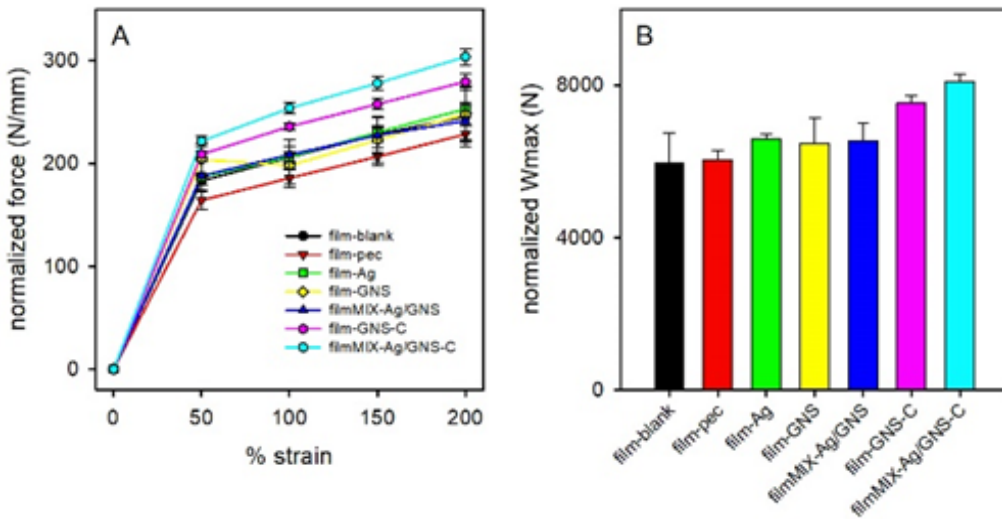
Figure 15 (A) Normalized force vs % strain curves; (B) normalized work of deformation.

Interestingly, the sample showing the highest tensile work value, when compared on statistical basis with all the other films considered in the study is **filmMIX-Ag/GNS-C**. A role of the hydrolyzed pectin present in this film as AgNP coater taking part in the cross-linking process may be hypothesized to explain this finding, although no further investigation has been carried out on this point.

Morphology

Low magnification (20000×) Scanning Electron Microscopy imaging was performed on **film-blank**, **filmMIX-Ag/GNS** and **filmMIX-Ag/GNS-C**. Figure 17C shows that the latter has a smoother and more compact appearance, compared to the two citric acid-reticulated films, which present a rougher and even cracked surface (Figure 17A-B). This is in agreement with previous observations on the different cross-linking approaches.
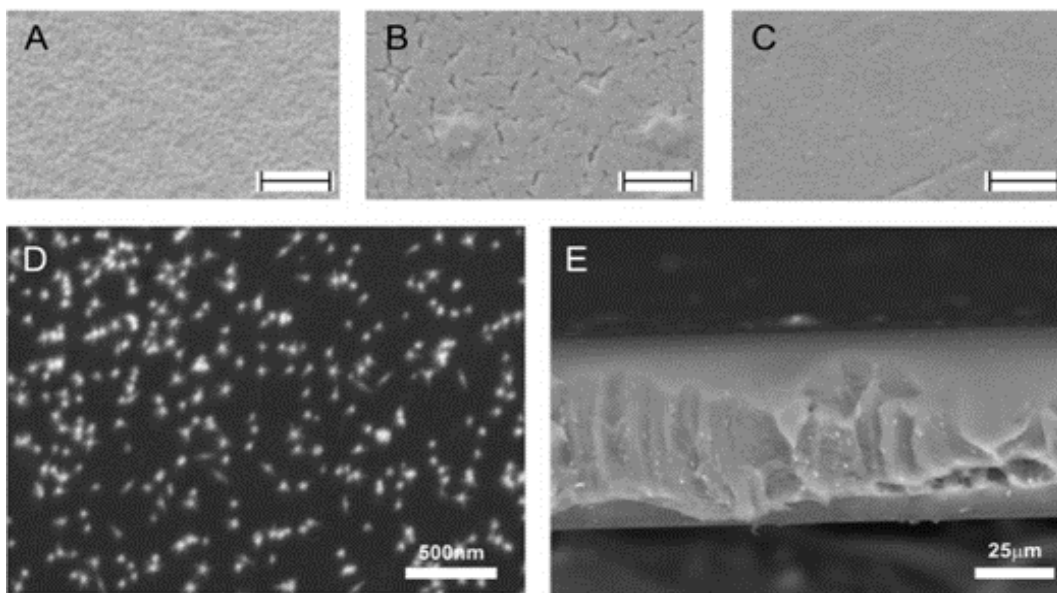
Figure 17 Low magnification SEM images of (A) film-blank, (B) filmMIX-Ag/GNS and (C) filmMIX-Ag/GNS-C, scale bar = 1 μm; (D) backscattered electrons SEM images of the filmMIX-Ag/GNS-C surface and (E) of its cross-section.

Higher magnification SEM on **filmMIX-Ag/GNS-C** allowed to image GNS close to the surface (Figure 16; the smaller AgNP cannot be observed on this scale) and to verify their homogeneous distribution in the sample (see Figure 17D-E for backscattered electrons images of the surface and of a cross-section of the film).
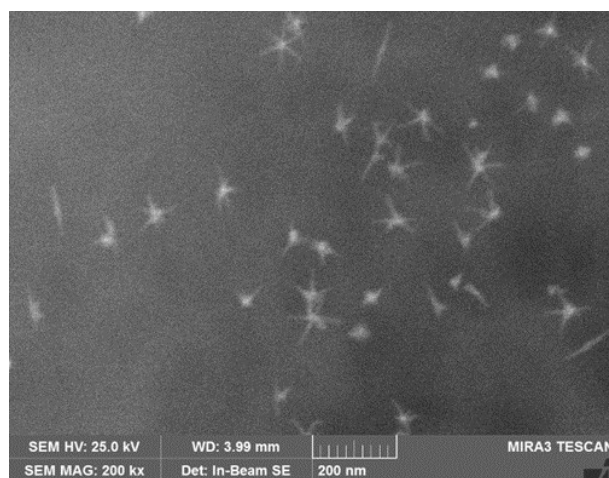
Figure 16 SEM image (200,000×) of filmMIX-Ag/GNS-C.

Hydration properties

PVA films are strongly hydrophilic. All the samples quickly absorb water up to 200-300% of their initial dry mass when soaked for 1 hour. Hydration degree does not significantly increase for longer immersion times, but partial films disruption starts to occur after 6 hours. For the more resistant films containing GNS-PEG-COOH, water absorption capacity has been measured also by placing dry samples in contact with a filter paper impregnated in buffered water at pH 7.2 at 37°C, in order to mimic real use conditions. In this case, the amount of absorbed liquid by both **film-GNS-C** and **filmMIX-Ag/GNS-C** in 1 hour is around 17% of their dry mass, with minor increases for longer contact times (18-20% for 24 hours).

Release of metals

Release of silver and gold in water has been evaluated according to the protocol described in 2.2.1.3. Release solutions, obtained by placing 90 mg film portions in 3 mL of bidistilled water for 1, 5 or 24 hours, have been analyzed by ICP-OES to determine the amounts of the two metals present.
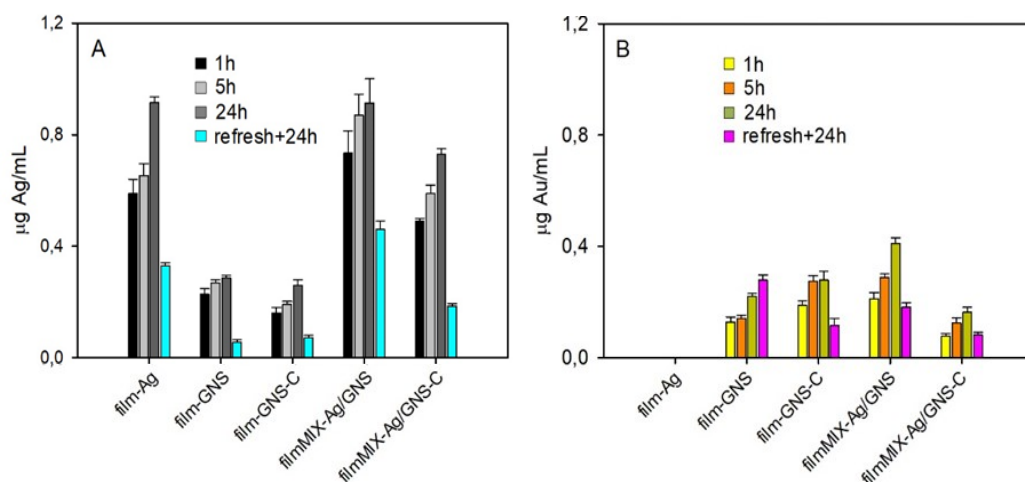
Figure 18 (A) Ag release (µg/mL) from different film samples in water (30 mg film/mL) after 1, 5 and 24 hours; "refresh+24h" indicates samples removed from water after 24 h and dipped in fresh water for further 24 h; (B) same, for Au.

Results for Ag are presented in Figure 18A, while Figure 18B shows data for Au. Samples named "refresh+24h" refer to films that, after 24 hours, have been transferred into fresh water and then analyzed after further 24 h of immersion. Silver is released in water, from films containing AgNP, reaching concentrations of nearly 1 ppm after 24 hours. Some Ag, although in smaller amounts (<0.3 ppm), is released also from **film-GNS** and **film-GNS-C**, where it is present inside the lattice of the nanostars. Most of the metal seems to be released in the first 24 hours, as the "refresh+24h" values are much lower (light blue bars in Figure 18A). This is in line with previous findings on AgNP immobilized on solid surfaces, where a rapid increase of Ag^+ in solution was measured in the first 24 hours, while only a minor additional release was observed on longer times.[22,99] Based on this references, it can be supposed that silver is released in its ionic form, derived from a slow AgNP oxidation by O_2. The amount released from **film-Ag** is 15.0% (1h), 17.1% (5h) and 23.9% (24h) of the total Ag content of the sample, while for **fimMIX-Ag/GNS** and **filmMIXAg/GNS-C** values are slightly lower (between 9.0% and 11.4% for the first; between 5.8% and 8.5% for the second). Unexpectedly, minor amounts of gold are also found for films containing GNS (Figure 18B). In particular, the maximum level of Au detected in solution is 0.41 ppm after 24h for **filmMIX-Ag/GNS** (corresponding to 1.2% of the total Au present). Given that GNS cannot be oxidized by O_2, these data could be explained by the release of unreduced noble metals ions that remain adsorbed on the surface of the nanoparticles from the synthesis.[16,17] However, a leakage of AgNP and GNS in traces (no plasmonic features can be found in the absorption spectra of the release solutions) cannot be excluded, especially considering the partial film degradation observed for long immersion times.

2.3.2.3 Photothermal effect

Thermograms of **filmMIX-Ag/GNS**, **filmMIX-Ag/GNS-C**, and **film-Ag** presented in Figure 19A were acquired with the help of a thermal camera, following the procedure described in 2.2.1.3. Dry film samples have been irradiated with a laser source at 808 nm with 0.13 W/cm² irradiance.
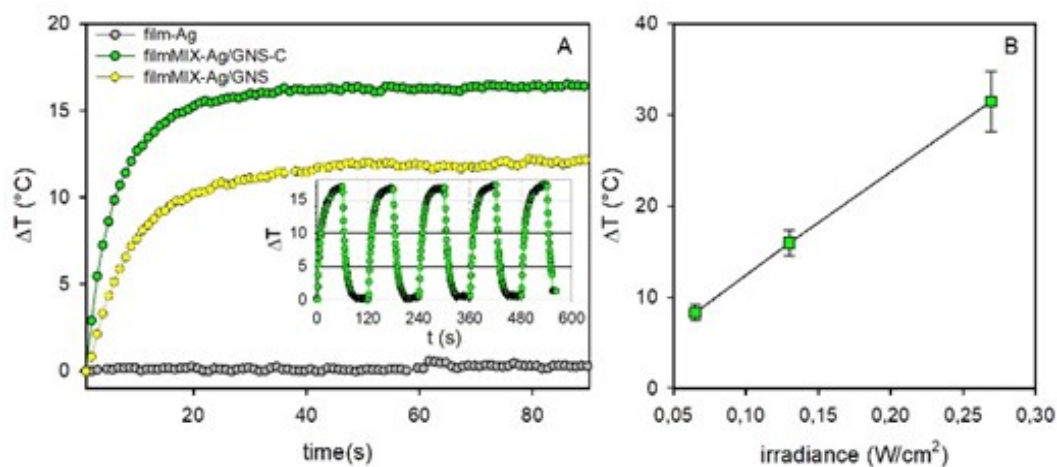
Figure 19 (A) Thermograms (ΔT vs time) for filmMIX-Ag/GNS-C, filmMIX-Ag/GNS and film-Ag, irradiance 0.13 W/cm²; inset: thermogram for 5 ON-OFF cycles (60 s + 60 s) on filmMIX-Ag/GNS-C. (B) ΔT vs irradiance for filmMIX-Ag/GNS-C.

In all cases when GNS are present, a prompt increase of the temperature (ΔT) is observed in the first 20-30 seconds of irradiation, then reaching a plateau within 60 s. This thermal response is due to the excitation of the NIR LSPR band of the embedded nanostars. The difference in the ΔT values at plateau showed by the two GNS-containing films reflects the different intensity of the absorption of the two films at the excitation wavelength, as it can be seen in Figure 14B-C. Similar values were measured for **film-GNS** and **film-GNS-C**. Instead, as expected, no heating occurred in **film-blank**, **film-pec** and **film-AgNP** upon irradiation, as can be noticed by the flat grey plot in Figure 19A for **film-AgNP**, since they do not present any absorption over 600 nm (see Figure 13). Heating of **filmMIX-Ag/GNS-C** at

different laser powers have been carried out, confirming the expected linear dependence of the photothermal response on the irradiance (Figure 19B). At the maximum power used of 200 mW, corresponding to 0.26 W/cm^2, the sample can reach over 30°C of T increase. It is important to underline that all used irradiances with the 808 nm laser source remain under the 0.32 W/cm^2 limit imposed by ANSI (American National Standard Institute) for the use of lasers of such wavelength on human skin.[100,101] To demonstrate the thermal stability of the responsive films and the reproducibility of the experiment, five cycles of irradiation ON (60 s) and OFF (60 s) have been performed consecutively on **filmMIX-Ag/GNS-C** (see inset of Figure 19A). Perfectly superimposable ΔT vs irradiation time profile were found for all cycles.

2.3.2.4 Antibacterial activity on planktonic cells

The microbicidal effect of all films was determined against *E. coli* and *S. aureus* planktonic suspensions, according to the protocol described in 2.2.4.1. The cell viability was evaluated after 5 and 24 hours of contact with film samples immersed in the suspensions at the same concentration used for release experiments (30 mg/mL). The colony forming units (CFU) counted in all cases are compared with those from a control suspension without any film added. The microbicidal Effect (ME) is expressed as:

$$ME = \log N_C - \log N_A \qquad (1)$$

where N_C is the number of CFU counted for bacteria in reference suspensions and N_A for bacteria treated with films. Results are presented in Table 3.

Table 3 Microbicidal effect (ME) values at 5 h and 24 h on planktonic E. coli and S. aureus[1]

	E. coli		S. aureus	
	5 h	24 h	5 h	24 h
film-blank	1.2(0.2)	2.3(0.2)	2.9(0.2)	3.2(0.2)
film-pec	1.7(0.3)	3.0(0.2)	3.1(0.2)	3.7(0.3)
film-Ag	5.5(0.3)	>7	3.1(0.3)	>7
film-GNS	2.2(0.2)	4.9(0.3)	3.7(0.2)	4.6(0.3)
film-GNS-C	0.8(0.1)	2.3(0.2)	1.1(0.2)	2.3(0.2)
filmMIX-Ag/GNS	5.6(0.3)	>7	3.5(0.3)	>7
filmMIX-Ag/GNS-C	0.2(0.1)	4.4(0.3)	1.3(0.2)	4.7(0.3)

[1]*All reported data are the average of 3 experiments, standard deviation in parentheses*

A first observation is that, as expected, ME values are always higher after 24 hours than after 5 hours of immersion. In general, it can be noticed how AgNP-containing films show a remarkable effect against both *E. coli* and *S. aureus*. For two films in particular, namely **film-Ag** and **filmMIX-Ag/GNS**, ME values after 24 hours are higher than 7, meaning that nearly 0 CFU have been found after exposure. A significant antibacterial effect has been observed also for films containing only GNS but not AgNP, with **film-GNS** showing ME values close to 5. To explain this, it must be remembered that these films release Ag^+ too, due to the metal present in the GNS lattice (see 2.3.2.2 and Figure 18A for release data).

What is more surprising is that even **film-blank** and **film-pec** exert a relevant action, although their components are not supposed to possess bactericidal properties. To further examine this aspect, the effect of all the single components (PVA, PEG200, citric acid and pectin) has been checked by preparing solutions of these in PBS at concentrations corresponding to their total content in the relative

films (i.e. equivalent to 100% release). No ME was observed in any of the cases against both strains. Therefore, a purely mechanical effect can be hypothesized to explain the reported values for **film-blank** and **film-pec**. This means that planktonic cells are probably removed from the suspension thanks to their adhesion to the film samples. To support this hypothesis, a specific experiment has been devised to evaluate this "contact" effect. Briefly, bacterial suspensions have been filtered on cellulose acetate membranes, which were then placed in direct contact with samples of **film-blank**; a membrane alone, loaded with bacteria but without any film, was taken as control (see 2.2.4.1 for experimental details). After 5 hours of contact, the bacteria remaining on the recovered filter membranes have been resuspended, in order to count the viable cells and evaluate the apparent microbicidal effect given by this contact mechanism. 24h experiments had to be excluded, since films could not be completely detached from the membranes. Obtained ME values (1.57 for *E. coli* and 1.53 for *S. aureus*) are comparable with the results on planktonic cells, thus confirming the tendency of both strains to adhere to PVA films.
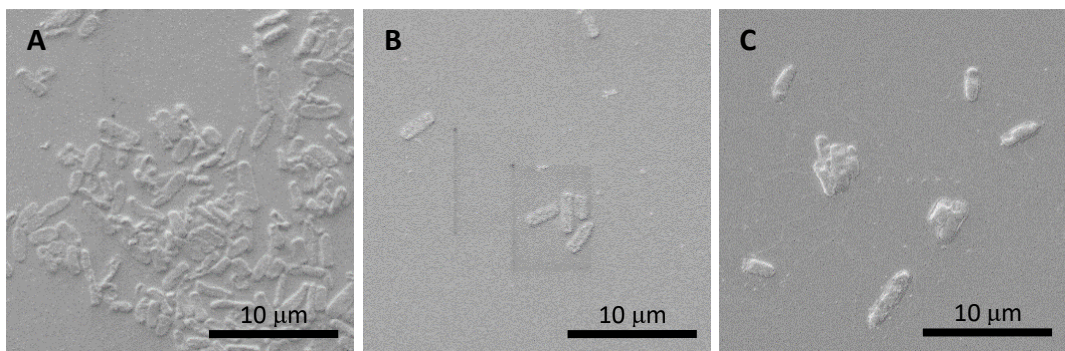
Figure 20 SEM images (10,000×) of E. coli bacteria adhering on (A) film-GNS, (B) film-GNS-C and (C) a glass slide, for reference.

However, the ME of **film-GNS-C** is much lower than that of **film-GNS** and a similar decrease is observed also for **filmMIX-Ag/GNS-C** compared to **filmMIX-Ag/GNS**. So, in other words, films that are cross-linked with GNS-PEG-COOH show a markedly more contained ME than their equivalent with GNS and citric acid. Given that an antibacterial action of citric acid itself has been excluded (at least in the range of concentration relevant to such experiments) and that Ag release is similar between the two films of each pair, the observed difference may be ascribed to the more compact texture of the films containing GNS-PEG-COOH as well as probably to the negative charge given by the carboxylate groups not involved in the reticulation. Both factors are likely to decrease the bacterial adhesion to the films, thus removing the additional, apparent ME effect, otherwise observed in all other cases. This hypothesis is supported by SEM images taken on films immersed for 5 hours in a suspension of *E. coli*. As can be noticed in Figure 20A, **film-GNS** is much more crowded with bacterial cells than the sparsely populated **film-GNS-C** surface (Figure 20B), which present a scarce adhesion of *E. coli*, comparable to that on a plain glass slide (Figure 20C).

2.3.2.5 Photothermal antibacterial effect

The on-demand bactericidal action of photothermal films upon irradiation has been investigated, according to a method recently proposed by the group of Pallavicini and Chirico and described in detail in 2.2.4.2.[87] PVA films have been inoculated with suspensions of *E. coli* or *S. aureus*, gently air-dried at RT and irradiated with a laser source at 800 nm and 0.30 W/cm² irradiance for 15 or 30 minutes; inoculated, non-irradiated samples have been tested as control. Samples were then stained with a live/dead kit that marks viable bacteria in green and those with damaged membranes in red and analyzed by confocal laser scanning

microscopy (CLSM). The extent of the microbicidal effect have been evaluated by the ratio between the red and the green areas in the acquired images, that allowed to calculate the percentage of dead cells.
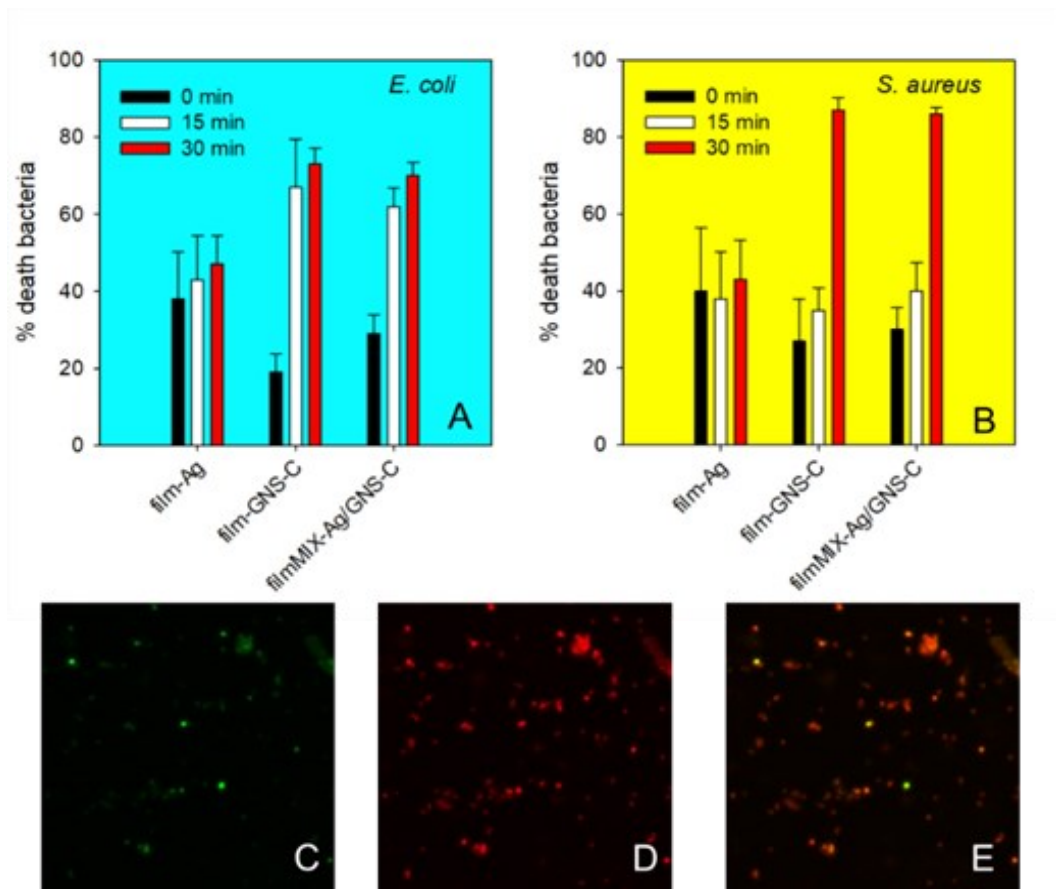
Figure 21 (A) % fraction of death E. coli bacteria inoculated in the films, with no irradiation (black bars), and laser irradiated at 808 nm for 15 min (white bars) and 30 min (red bars). (B) same, for S. aureus. (C) green channel (living cells) in stained filmMIX-Ag/GNS-C inoculated with E. coli and irradiated for 30 min; (D) same, red channel (death cells); (E) same, both channels.

Results for **film-Ag**, **film-GNS-C** and **filmMIX-Ag/GNS-C** are reported in Figure 21A and B (on *E. coli* and *S. aureus*, respectively). Figure 21C-E show representative CLSM images for the case of *E. coli* on **filmMIX-Ag/GNS-C** after 30 min irradiation.

For the two films containing GNS, thus exhibiting a photothermal effect, there is a clear enhancement of bacterial mortality upon laser irradiation. In particular, 60-70% of *E. coli* cells have been killed already after 15 minutes with both **film-GNS-C** and **filmMIX-Ag/GNS-C**, but further irradiation does not bring a substantial increase (73 and 70%, respectively, after 30 min). On the contrary, 15 min of laser treatment are not enough to drastically affect *S. aureus*, but after 30 min an impressive 87% death is reached with both types of film. This different response of the two strains relates to the higher resistance of Gram-positive bacteria, such as *S. aureus*, with respect to Gram-negative ones, such as *E. coli*, due to the rigid peptidoglycan cellular walls of the former.[102]

Also for **film-Ag** % death values of around 40% have been found on both strains, but, as expected, no significant increase is observed upon irradiation, since it does not produce any T increase on this sample. In fact, these values are due to the intrinsic bactericidal effect of the films with AgNP. For **film-Ag** this is higher than what found for the GNS-containing films when non-irradiated, even in the case of **filmMIX-Ag/GNS-C**, reflecting approximately the tendency of the different samples to release Ag (see data for 1h release time in Figure 18A for comparison). Finally, it must be pointed out that **film-blank** has been tested as well for reference and even in this case a fraction of dead cells between 21 and 26% was found for both strains, independently of the irradiation time (not shown in Figure 21). The reason behind these data appears to be the inherent stress conditions of the experimental setup, since bacteria inoculated on films are kept at room temperature, in a nutrient-free environment for the time needed to complete the experiment. This was confirmed by further control tests with an inert surface, such as a glass slide, where similar values have been measured. Overall, the obtained data show that the photothermal effect brings an additional contribution to the

microbicidal action, on top of the intrinsic one, against both the tested bacterial strains, although requiring different irradiation times.

2.3.2.6 Biocompatibility studies

Biocompatibility of PVA films have been verified evaluating their cytotoxicity against human fibroblasts by an indirect test, as described in 2.2.4.3.
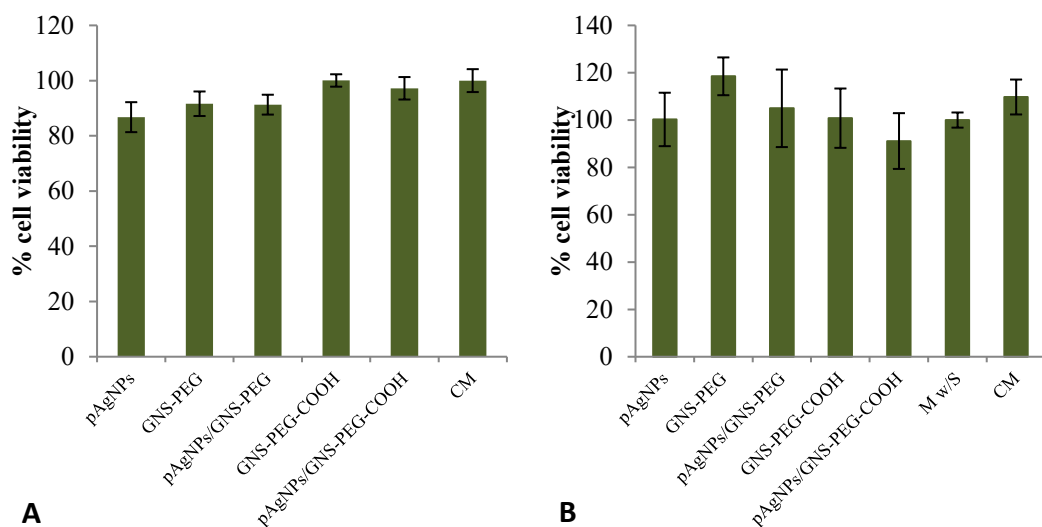
Figure 22 % cell viability for (A) cytotoxicity test and (B) proliferation test on NHDF; complete medium (CM) and medium without serum (M w/S) were considered as references (mean values ± s.d.; n=12).

Results reported in Figure 22A show that viability is preserved (~ 100%) with the two films containing GNS-PEG-COOH, while **film-Ag**, **film-GNS** and **filmMIX-Ag/GNS** cause a modest reduction of the fibroblasts viability (87, 91 and 92%, respectively). On the whole, these data indicate an acceptable biocompatibility of all the obtained films.

A similar experiment has been performed to determine the capability of PVA films to promote fibroblasts proliferation. Unfortunately, as can be noticed in Figure 22B, no significant increase of cells growth is observed when incubated with the

"conditioned" medium that is obtained from the films (see experimental details in 2.2.4.3). However, no inhibition occurs as well, confirming the compatibility of the material.

2.4 CONCLUSIONS

After finding the proper conditions that allowed the stable inclusion of AgNP and GNS together in the same precursor solution, PVA films were prepared. A set of films containing both nanoparticles, mixed or separate, were obtained by casting and cross-linking with either citric acid or exploiting the terminal carboxylate group of GNS coated with HS-PEG-COOH.

In general, NP-containing films demonstrated an intrinsic antibacterial activity, which lasts and increases up to at least 24 hours. This is attributed to the well-known action of Ag^+, that in this case can be released from the GNS lattice, where a small fraction of Ag is included from the synthesis, as well as from AgNP. However, when the latter are present the microbicidal action is markedly stronger at both times examined (5h and 24h). Adhesion of bacteria was also noticed, particularly on films reticulated with citric acid, leading to their removal from planktonic suspensions. This, in turn, gives rise to an apparent microbicidal effect that contributes to the overall antibacterial action of all the films, except for those with GNS-PEG-COOH, where this mechanism is much less relevant, due to their more compact structure and smoother surface.

In addition to this intrinsic effect, an on-demand photothermal antibacterial action was demonstrated upon laser irradiation of the GNS-containing films. While in the case of **filmMIX-Ag/GNS** (with citric acid as cross-linker) the GNS LSPR absorption band placed in the NIR range drastically decays within a month, it remains unaltered in **filmMIX-Ag/GNS-C**, which appears to be the best candidate for the potential development of a bifunctional medical device, aimed for practical applications such as wound disinfection and healing. With this material, a CFU reduction higher than 4 log units (ME) was observed after 24 hours on both

planktonic *E. coli* and *S. aureus* strains, thanks to the intrinsic action of silver alone. Moreover, laser treatment for just 30 minutes allows to kill the large majority of the bacteria in direct contact with the film. Such irradiation is performed with a low energy radiation (800 nm) falling inside the bio-transparent window, with applied irradiances (0.3 W/cm^2) well within the limit imposed by ANSI for human skin treatment.

Finally, the suitability of this material for real use on wounds is supported by its good biocompatibility, as observed in cytotoxicity tests on human fibroblasts. Unfortunately, films cannot also significantly promote the proliferation of these cells, but this could be enhanced, for instance, with the inclusion of specific additives, such as growth factors, in the material.

PART 3. STUDY OF THIOL-PEG COATING OF GOLD NANOPARTICLES

3.1 BACKGROUND

3.1.1 The role of NP surface ligands

The choice of proper surface ligands is fundamental for the design of advanced nanomaterials. Indeed, these molecules play a significant role not only for the synthesis of robust nanoparticles with specific size, morphology and properties, but also for their further modification and combination with other components. Their action can range from the regulation of the solubility and availability of species involved in the NP preparation to their post-synthetic stabilization by minimization of surface energy and prevention of agglomeration phenomena. Moreover, depending on the coating chemical nature, successive functionalization by coupling reaction may be envisaged, together with responsive behavior switched by changing parameters such as pH or temperature.

The variety of ligands employed for the coating of NP includes small organic molecules, polymers of different molecular weight and polarity, surfactants and various biomolecules (e.g. peptides, proteins, nucleic acids, aptamers), all providing NP with specific additional features (Figure 23).[103] Moreover, the possibility to graft multiple different ligands on the NP surfaces, thus creating mixed coatings, enables a richer and finer set of possible reactions and properties associated with the NP core, obviously expanding the arsenal of potential applications. Therefore, it is evident how the selection of appropriate ligands is crucial to obtain a final nanomaterial with suitable properties for the target application. The choice must take into account different factors, such as the chemical nature of the NP surface and its interaction with the coating molecules as well as their surrounding environment and the need for further modifications.
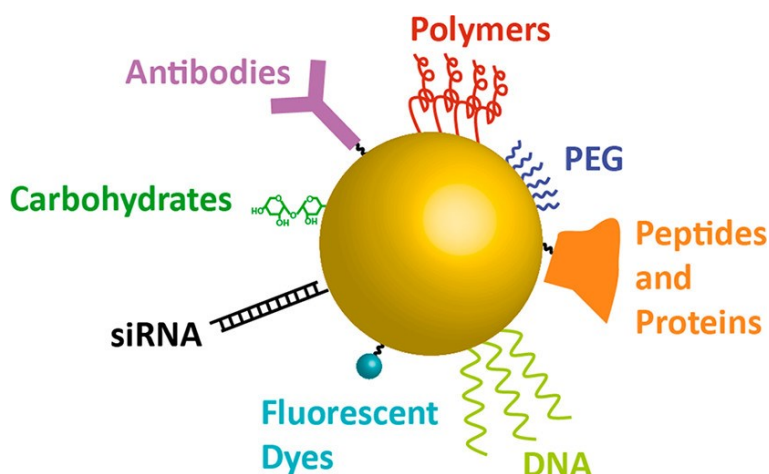
A direct example of the coating role was encountered in my PhD research and is described in the previous part of this thesis. The coating of GNS with an α,ω bifunctional PEG – one end featuring the –SH grafting group, the other a –COOH function – allowed to obtain a more stable precursor solution with respect to –OCH$_3$ terminated PEG of similar mw. In addition, GNS with such coating were able to act as cross-linker in the formation of the PVA polymeric films, yielding products with superior stability and mechanical properties. On the other hand, this case, in which the end function of the linear polymeric coating molecule is a carboxylic acid, led to the decision of studying how the acid-base properties of a molecule may be influenced by the presence of a "substituent" of "infinite" dimensions (a spherical nanoparticle, a nanorod, a nanostar) and by the reciprocal influence exerted by a high number of functions gathered in a nano-volume. This is the theme of this part of the PhD thesis. Due to the hard synthetic challenges posed by this kind of study (see 3.3.2.2) and to the scarce reproducibility of gold nanoparticles with complex shapes, the decision was taken to work on the simplest possible model, i.e. spherical gold nanoparticles.

3.1.1.1 AuNP coating

After the first chemical preparations of gold colloids reported Michael Faraday in 1857,[104] based on the reduction of an aqueous solution of tetrachloroaurate and phosphorus dissolved in carbon disulfide, an efficient alternative method was later described by Turkevich for the facile preparation of spherical AuNP via the reduction of gold ions in an aqueous boiling solution of trisodium citrate.[105] This method was then developed by Frens to enable control over the NP size by varying the gold/citrate ratio.[106] The synthetic process has been extensively investigated in the following years, finding that sodium citrate plays multiple roles in the reaction, not only reducing the gold salt and stabilizing the resulting NP through electrostatic repulsion, but also determining the process pH, which ultimately affects the particle size distribution.[107–109]

However, citrate-coated AuNP have the major drawback of all electrostatically stabilized NP, that is irreversible aggregation induced by high salt concentrations and/or pH modifications. On the other hand, the weak binding of citrate (6.7 kJ/ mol) allows for an easy ligand exchange.[110] This can be done with many species bearing different functional groups that can bind more strongly on the AuNP surface, such as thiolates and amines.[111,112] Thiols in particular have been widely employed, as the strong sulfur-gold interaction (126–167 kJ/mol) yields an efficient exchange and greatly enhances the colloidal stability.[113–115]

3.1.2 Polymeric coating

The use of polymers that are able to interact with the NP surface by physi- or chemisorption can give a greater steric stabilization, sometimes coupled with an electrostatic contribution.

During synthesis, polymers can bind preferentially to specific crystallographic planes of the NP surface and promote anisotropic growth or serve as a matrix for nanocrystal growth. For example, poly(vinyl pyrrolidone) (PVP)-stabilized AuNP showed changes in their optical properties due to energy transfer between PVP and the NP core.[116] It was observed how PVP molecules dispersed in hot water not only act as surface ligands but also control clustering and growth of polygonal AuNP (25–50 nm). Similar to PVP, poly(vinyl alcohol) (PVA) has also been shown as a suitable ligand for NP synthesis. Polyelectrolyte-protected AuNP of different sizes have been obtained directly by heating $AuCl_4^-$ in an aqueous solution of amine-containing polyelectrolytes such as poly(ethylenimine)[117] and poly(allylamine hydrochloride).[118] Wang and coworkers reported a one-step aqueous preparation of highly monodisperse AuNP smaller than 5 nm using thioether- and thiol-functionalized polymer ligands: dodecanethiol (DDT)-poly(acrylic acid), DDT-poly(methacrylic acid), DDT-poly(vinylsulfonic acid), DDT-poly(vinylpyrrolidone), DDT-poly (hydroxyethyl acrylate), and DDT-poly(ethylene glycol methacrylate). Here particle uniformity and colloidal stability were strongly dependent on changes in ionic strength and pH.[119]

3.1.2.1 PEG-based coatings

A very popular class of polymeric coatings are polyethylene glycols (PEG) and their derivatives. This is a unique category of various molecular weight polymers, presenting interesting properties such as high solubility in water as well as many organic solvents, efficient NP stabilization against aggregation, high biocompatibility and stealth functions.[120]

One of the first demonstration of the promising role of these polymers as NP coating was reported in the development of Doxil®, the first FDA-approved nano-formulation of doxorubicin. The grafting of PEG molecules around the liposomes loaded with the anticancer drug was effective in preventing the non-specific adsorption of plasma proteins, thus minimizing the accumulation of liposomes into the liver and spleen rather than in the target delivery site.[121] Since then, the use of PEG became a common practice in the design of nanomedical formulations, both at the research and commercial levels, with the aim of stabilizing NP against aggregation, preventing undesired uptake in vivo, increasing their circulation time in blood and enhancing the accumulation into target organs.[122]
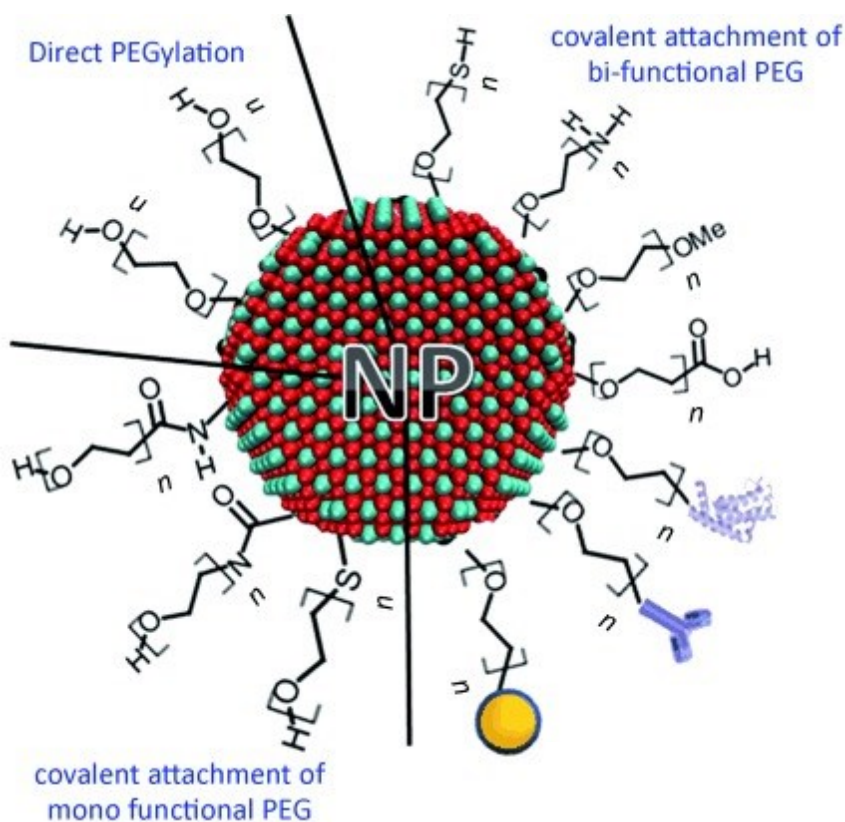
Figure 24 Different possible strategies for the PEGylation of nanoparticles. [120]

PEG coating of NP (PEGylation) can be achieved by simply adding the desired PEG molecules in the synthetic process. This approach is commonly employed to coat polymeric NP and it has also been reported for the functionalization of some inorganic NP.[120] However, "plain" PEG molecules are only weakly bound to the NP surface and can easily detach during processing of the colloid (e.g. dilution, centrifugation, heating, drying, mixing with other components). A common strategy to overcome this limitation is the use of PEG molecules bearing functional groups able to bind onto the NP surface, such as thiols, amines, carboxylic acids, or silanes, depending on the NP nature (Figure 24).

In the case of AuNP, thiolated PEG ligands provide exceptional colloidal stability under a wide range of conditions, thanks to the strong coordinative S-Au bond, and enhanced biocompatibility.[123] The stability of the Au-S bond in gold nanoparticles has been recently reinvestigated by the groups of Pallavicini and Chirico.[124] The coordinative nature of such bond has been confirmed, and also its high stability, based on a thiolate (-S$^-$)-Au$^+$ interaction. However, it was observed that a temperature increase to 40°C leads to a partial detachment of the thiols grafted on a GNS. The % of detachment depends on heating time (e.g. 5% for 40 min heating for a bodipy-thiol molecule, and 1% for 20 min heating) and is also proportional to the solubility of the thiol in the receiving solution. The latter point must be seriously taken into account when a hydrophilic coater such as a PEG-thiol is used, especially if PEG-coated AuNPs are planned for in vivo use (considering 37°C as the typical body temperature). On the other hand, a fundamental point relevant to the studies carried out in this part of the PhD research, is that the Au-S bond in GNS is sufficiently strong and/or kinetically inert to remain definitely intact, at least at room temperature, provided that competing species (like, for instance, other thiols or amines) are not present in the Au

nanoparticles colloidal solution. Although the mentioned study regarded the oddly-shaped GNS, it was assumed that the same Au-S bond stability is found for HS-PEG coatings, at room temperature, on spherical AuNP. This assumption was also confirmed by potentiometric titration data (see 3.3.2.2).

As a final consideration, the grafting of bifunctional PEG and the study of their acid-base properties, as already pointed out, is important for additional functionalization of the coating layer with various (bio)molecules, such as fluorophores, peptides and antibodies, typically through amide bond formation (for amine or carboxyl-terminated PEG@AuNP) or click chemistry reactions (e.g. azide-PEG@Au NP), while maintaining the stability of the system.[120,125] The addition of end groups whose charge depends on pH, such as carboxylates or amines, also affects the properties of the coating (non-functional PEG generally displays little net-charge), altering the interactions with other biomolecules and the surrounding environment in general.[126]

3.1.3 Investigation of the coating properties

3.1.3.1 Confinement effects

Immobilization of coating ligands onto nanoparticles can modify the physicochemical properties of these molecules, including the redox potentials, ability to undergo conformational changes and the availability for further functionalization or assembly of superior structures.[127]

The effect of confinement of molecules in a limited volume on their acid/base properties has been already explored in micellar systems.[128] Indeed, micelle-included molecules are confined inside a nanometric volume, generating a huge increase of their local concentration. For example, when a lipophilic molecule is added to a bulk aqueous micellar solution, even at micromolar or sub-micromolar

concentration, its local in-micelle concentration rises up several orders of magnitude, thanks to micellar inclusion. Therefore, reciprocal interactions (e.g. coordinative, donor–acceptor, hydrogen bonding) between different molecules inside a micelle will be strongly promoted.

This phenomenon, together with poor solvation and low ions concentration, particularly affects the tendency to protonate/deprotonate of the included acid/base active species. For example, dodecyldimethylamine included in micelles from Triton X-100 displays a logarithmic protonation constant of 7.84, almost 3 log units lower than the value for the reference triethylamine in water.[129]

Moreover, the electrostatic effect played by the overall charge on the micellar surface can be modulated by varying the composition of the micelles in terms of surfactants (e.g. anionic, cationic or non-ionic), enabling a certain degree of control on the pK_a and log K values of micelle-included species.[130]

3.1.3.2 Potentiometric titrations

A crucial point in the optimization of functional NP for successive modifications or combination with other components is an extensive characterization of their coating, including the accurate quantification of the available functional groups grafted on the NP surface and the assessment of their physicochemical properties. Potentiometric titrations have been proposed as a powerful and convenient tool for this purpose.[131,132] Indeed, the possibility this technique offers to determine both the number of surface functional groups and their properties in terms of ionization state can help improving the quality and reproducibility in the development of advanced nanomaterials.
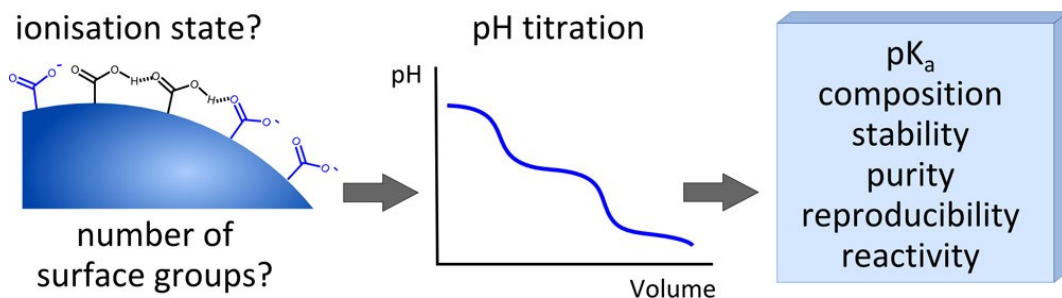
Figure 25 Schematic approach for the characterization of NP coating by potentiometric titrations.
[131]

Acid-decorated NP have been widely exploited for the formation of advanced coatings by bioconjugation or self-assembly on the NP surface.[125,133] In all these systems, the knowledge of the protonation state of the carboxylic groups is of key importance for a proper functioning. How NP binding affects the immobilized ligands has been scarcely investigated, with a focus on the modification of the acid-base equilibria of the acidic coating molecules. For example, it has been demonstrated that the pK_a of a self-assembled monolayer (SAM) of a model acidic ligand, 11-mercaptoundecanoic acid (MUA), on AuNP differs from the value characterizing the SAM on a flat surface by as much as two pH units.[132] The authors also observed a variation of the pK_a shift that is correlated with the NP curvature. In particular, with the NP radius decreasing, the distance between the charged end groups increases, thus lowering the electrostatic repulsion between them. Therefore, smaller NP have smaller pK_a shifts. It was also described how the value of the pK_a can be controlled by the concentration of salt in solution and by the size of the ions.[132] Similarly, another work found a positive pK_a shift of 2–2.5 units for MUA molecules grafted onto AuNP compared to the free ligand value. The increase was attributed to the accumulation of negative charges on the surface, as carboxyl groups deprotonate. Even higher pK_a shifts were measured in the case of

a shorter ligand, 3-mercaptopropanoic acid (MPA).[131] Such findings are consistent with older studies on carboxyl-terminated thiols SAM on planar Au surfaces.[134,135] It is then clear that NP-bound coating molecules display a different chemical reactivity than that of the starting material. For instance, the weak nucleophilicity of carboxylate groups will be exerted at different pH when free in solution or when supported on NP. The use of potentiometric titrations for the quantitative characterization of NP coating enables the control of its stability as well as the efficiency of purification procedures or the yield of functionalization reactions. This method of investigation can be extended to other types of coated NP and can help tailor the properties of nanostructured materials and systems based on ionizable molecules.

3.2 EXPERIMENTAL DETAILS

3.2.1 Materials and instrumentation

3.2.1.1 Reagents

Gold(III) chloride solution 99.99% (30 wt. % in dilute HCl); Trisodium citrate dihydrate; 2-(2-Methoxyethoxy)ethanethiol 97%; O-(2-Mercaptoethyl)-O'-methyl-hexa(ethylene glycol) ≥95%; Poly(ethylene glycol) methyl ether thiol (HS-PEG-OMe, mw 750); Poly(ethylene glycol) methyl ether thiol (HS-PEG-OMe, mw 2000); Poly(ethylene glycol) methyl ether thiol (HS-PEG-OMe, mw 5000); Methoxyacetic acid 98%; 2-(2-Methoxyethoxy)acetic acid; [2-(2-Methoxyethoxy)ethoxy]acetic acid; O-(2-Carboxyethyl)-O'-methyl-undecaethylene glycol ≥95%; Thiol-dPEG®4-acid ≥95%; O-(2-Carboxyethyl)-O'-(2-mercaptoethyl)heptaethylene glycol ≥95%; O-(3-Carboxypropyl)-O'-[2-(3-mercaptopropionylamino)ethyl]-polyethylene glycol (HS-PEG-COOH, mw 3000); O-(3-Carboxypropyl)-O'-[2-(3-mercaptopropionylamino)ethyl]-polyethylene glycol (HS-PEG-COOH, mw 5000); Sodium nitrate ≥99%; Potassium phthalate monobasic acidimetric standard; Sodium hydroxide standard solution 0.1 M; Nitric acid standard solution 1 M; Nitric acid ≥65%; Hydrochloric acid ≥37% have all been bought by Merck Life Sciences, Milano, Italy, and used without further purification.

3.2.1.2 Glassware pre-treatment

All the glassware used in the syntheses was pre-treated with *aqua regia* for 15 minutes and then washed three times with bidistilled water in an ultrasound bath for 5 minutes.

3.2.1.3 Instrumental procedures

Ultracentrifugation

Ultracentrifugation was carried out using the Hermle Z366 ultracentrifuge with 10 mL polypropylene tubes or 30 mL polycarbonate tubes.

Rotary evaporation

Gold colloids were concentrated using a LABOROTA 4000eco rotary evaporator (Heidolph), keeping the water bath at 30-35°C.

UV-Vis-NIR spectroscopy

Absorption spectra were recorded on a Varian Cary 60 spectrophotometer in 1 cm optical glass cuvettes.

Dynamic Light Scattering (DLS)

DLS analysis was performed with a Zetasizer Nano ZS90 instrument (Malvern Instruments) equipped with a 4mW 632.8 nm laser source. Size were carried out in a quartz fluorescence cuvette (1 cm×1 cm) with a 90° detecting angle. For zeta potential measurements a folded capillary cell (DTS1070) was used.

Thermogravimetric analysis (TGA)

Dried AuNP samples were analyzed with a TGA Q5000 instrument (TA Instruments) by heating in a Pt crucible under nitrogen flux, from room temperature up to 600 °C with a linear ramp of 5°C/min. Data were elaborated by Universal Analysis v.4.5A software (TA Instruments) and the mass loss and temperature at mass loss values were evaluated considering the DTG signals.

Potentiometric titrations

All the potentiometric titrations were performed with the help of a Mettler-Toledo G20 automatic titrator, equipped with a combined glass electrode (DGi115-SC), in a glass titration vessel connected to a circulating thermostat (LAUDA Ecoline

RE207) at 20°C. Standard 0.1 M NaOH solution was used as titrant; titer was checked before each titration session by standardization with potassium hydrogen phthalate. All titrand solutions were prepared in bidistilled water with $NaNO_3$ 0.05 M and HNO3 1 M standard solution was added in small amounts to adjust the starting potential. Nitrogen was bubbled in the vessel for 5 min before starting the titrations and then kept flowing throughout the whole experiment to maintain an inert atmosphere. Experiment control and data collection was carried out by the Mettler-Toledo LabX software; data analysis was performed with Hyperquad2008 software.

3.2.2 Gold nanoparticles preparation

All solutions were prepared with bidistilled water, if not stated otherwise.

3.2.2.1 AuNP synthesis

Spherical gold nanoparticles (AuNP) were prepared through the standard citrate reduction method by Turkevich.[105] 87 μL of $HAuCl_4$ solution (30 wt. % in dilute HCl) were added to 500 mL of bidistilled water and brought to boiling. Then, 25 mL of a 0.017 M solution of sodium citrate dihydrate in water were added and, after the color turned to ruby red, heating was switched off, leaving the solution stirring for 2 hours. Before further use the prepared colloid was allowed to cool down to room temperature.

3.2.2.2 AuNP coating and purification

Citrate-coated AuNP from the synthesis were then treated with a HS-PEG or HS-PEG-COOH to exchange the coating ligand. The selected thiol was dissolved in the colloid so as to get a PEG concentration of 2×10^{-5} M and allowed to react for at least 3 hours at room temperature. Then, pegylated AuNP were purified by

ultracentrifugation at 13000 rpm (15870 rcf) for 30 min. The supernatant was discarded and each pellet redispersed in the original volume of fresh water. The procedure was repeated two times, after which the AuNP are ready for further characterization. For TGA measurements, a third ultracentrifugation cycle was performed on 100 mL of the colloid. The resulting pellets were reunited, dried under a gentle nitrogen flow until complete solvent evaporation and then kept under vacuum in a desiccator before the analysis.

3.2.3 Potentiometric titrations

3.2.3.1 Free ligands titration

20 mL of 0.1 mM, 0.5 mM and 1 mM solutions of the molecules considered were prepared, either by directly dissolving the solid in water (with $NaNO_3$ 0.05 M) or by dilution of a $0.01 - 0.1$ M stock solution, and placed in the thermostatic titration vessel, allowing to thermally equilibrate to 20°C. After the addition of 50 µL of 1 M HNO_3 standard solution, they were titrated with NaOH 0.1 M standard solution, using stepwise additions of 10 µL. A gentle nitrogen flow was kept in the empty space over the solution in the titration vessel, in order to avoid atmospheric CO_2 interference.

3.2.3.2 PEG-coated AuNP titration

For potentiometric titrations of the PEG molecules bound on AuNP, concentrated colloids were necessary. In order to have sufficient AuNP solution for the experiments, the synthesis described in 3.2.2.1 was scaled up to 2.5 L. In this case the amount of PEG added to coat the NP was exactly that needed to obtain a 100% coverage, as calculated from TGA data. In particular, 15.0 mg of HS-PEG_{5000}-COOH and 19.0 mg of HS-PEG_{3000}-COOH were used alternatively. The procedure for the

coating is the same reported in 3.2.2.2. After pegylation, the whole volume of AuNP was reduced to roughly 250 mL by rotary evaporation. The obtained 10× solution has been then purified with 3 cycles of ultracentrifugation at 13000 rpm for 30 min. After each cycle, the supernatant was not completely colorless, given the high colloidal concentration, so a second round of centrifugation was performed to maximize the NP recovery. All the pellets obtained were collected together and redispersed in a total volume of 25 mL with bidistilled water. This 100× concentrated AuNP solution was then placed in a dialysis tube membrane (MWCO 14 kDa) and thoroughly purified for one week to achieve the complete elimination of all the citrate present, which obviously would interfere in the potentiometric measurement. At this point, after the addition of the supporting electrolyte (NaNO$_3$ at 0.05 M concentration) and excess acid (250 µL of HNO$_3$ 1 M), the whole batch was transferred in the thermostatic titration vessel, allowing to thermally equilibrate to 20°C, and titrated with standard 0.1 M NaOH, using stepwise additions of 10 µL, under a N$_2$ atmosphere.

3.3 RESULTS AND DISCUSSION

3.3.1 PEG-coated AuNP

3.3.1.1 AuNP preparation and coating

Citrate-coated AuNP have been prepared via a standard citrate reduction method (see experimental details in 3.2.2.1) yielding monodisperse spherical nanoparticles with an average diameter of 17(1) nm. A typical extinction spectrum, presenting a sharp LSPR band at 519 nm, together with a picture of the colloid and an electron microscope image of the NP are shown in Figure 26. Hydrodynamic diameter (d_{hyd}) and zeta potential (ζ), measured by Dynamic Light Scattering (DLS), are reported in Table 4.
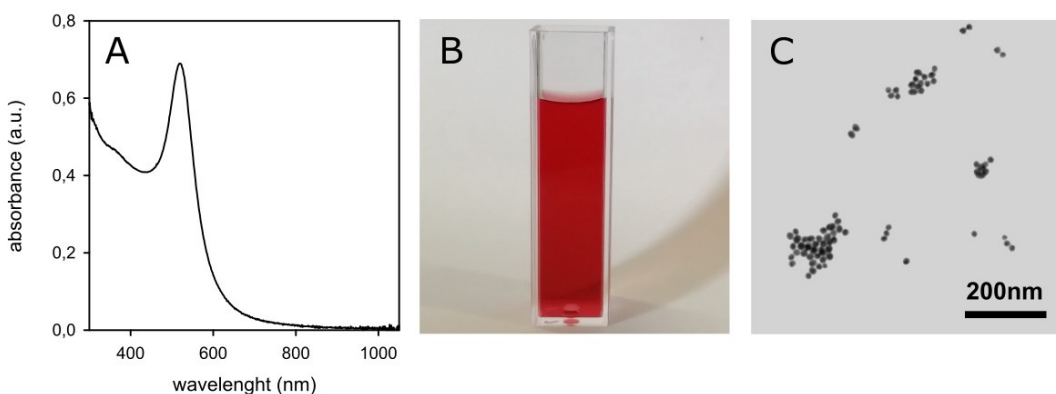
Figure 26 (A) Extinction spectrum, (B) picture and (C) TEM image of a freshly prepared solution of citrate-coated AuNP.

Freshly prepared AuNP have been then coated with various thiolated polyethylene glycols with different molecular weights (general structures of the molecules are shown in Figure 29). In particular, four methoxy-terminated PEG (HS-PEG) with average molecular weight of 2000 (n ~ 44), 5000 (n ~ 112), 10000 (n ~ 226) and 20000 (n ~ 453) were chosen, together with two α,ω-bifunctional polymers (HS-PEG-COOH) with mw = 3000 (n ~ 64) and 5000 (n ~ 110).

In all cases, an equal, slight red-shift of 2-3 nm of the LSPR absorption band has been observed upon pegylation, due to the small local refractive index variation associated with the substitution of the coating ligand on the NP surface (see Figure 27 for a representative spectrum of AuNP@HS-PEG$_{5000}$-COOH compared to that of the starting AuNP solution).
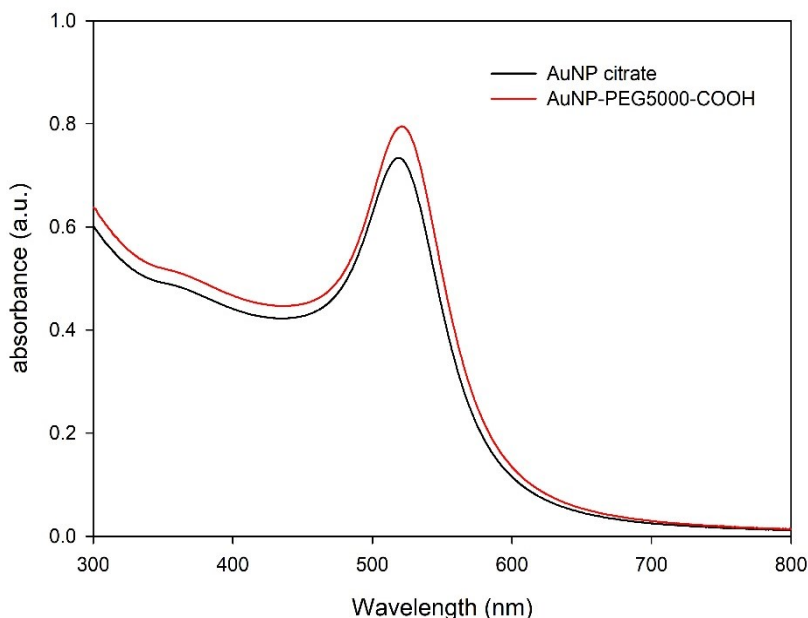
Figure 27 Extinction spectra of a solution of citrate-coated AuNP (black line) and of the same coated with HS-PEG$_{5000}$-COOH (red line)

3.3.1.2 Coating characterization

Size and zeta potential

All the samples have been analyzed with DLS in terms of hydrodynamic diameter (d_{hyd}) and zeta potential (ζ). Results are reported in Table 4. As-prepared AuNP have a highly negative ζ value (−32 mV) due to the layer of citrate anions adsorbed onto their surface. These are displaced by the addition of PEG thiols, that bind on the Au surface in the thiolate form (-S-PEG). This explains how the zeta potential observed with neutral PEG (without -COOH) is still negative, although less

pronounced and moving toward zero with increasing coating thickness. Longer polymeric chains shield more the negative charge present on the AuNP surface – considering that ζ is measured at the slipping plane, which is moved further from the surface with bigger PEG molecules.

Table 4 Zeta potential (ζ), hydrodynamic diameter (d_{hyd}), % PEG/Au ratio and average number of PEG molecules per particle for AuNP coated with different HS-PEG and HS-PEG-COOH. Data for citrate-coated AuNP are reported for reference.

	AuNP citrate	AuNP HS-PEG				AuNP HS-PEG-COOH	
PEG MW		2000	5000	10000	20000	3000	5000
ζ (mV)	-32	-13	-5	-9	-1	-22	-13
d_{hyd} (nm)	21	23	54	74	93	48	56
%w/w PEG/Au	-	11.5%	29.4%	29.7%	43.6%	14.4%	10.9%
n PEG/NP	-	1805	1759	889	652	1434	652

Accordingly, a clear trend can be noticed in the size of the coated particles, with the hydrodynamic diameter increasing with the polymer length, both in the case of HS-PEG and HS-PEG-COOH. Instead, as expected, similar dimensions have been found for particles coated with PEG molecules with the same mw, regardless of the terminal functional group, as can be verified comparing values for AuNP@HS-PEG5000 and AuNP@HS-PEG5000-COOH.

Zeta potential in the case of carboxylated AuNP is clearly more negative, due to the presence of charged -COO⁻ groups (fully deprotonated at working conditions) on the outer part of the coating. However, a decrease of its absolute value with increasing PEG mw seems to occur also in this case, but this is likely related to the decrease of the NP coverage (see discussion below).

Determination of PEG coverage

In order to evaluate the average number of coating molecules grafted on a single particle, thermogravimetric analysis (TGA) was performed on all AuNP samples considered. This technique allows to precisely quantify the amount of substance lost (or eventually gained, e.g. in reactions with oxygen) from a sample upon heating. A linear temperature ramp of 5°C/min has been used. Since, after purification, the only organic material remaining in the samples should be the PEG grafted on the AuNP, the weight loss occurring in the 200-400°C range can be entirely attributed to the NP coating. Once the amount of Au fraction in the sample is derived by difference from the initial weight of the whole sample (residual water, sometimes visible in the TGA curves as a small loss around 100°C, must be subtracted too), the PEG/Au ratio can be calculated (see results in Table 4). From these data, the average number of PEG molecules per particle can be obtained knowing the average NP mass, calculated in turn from the Au density and the volume of the NP core (measured with TEM imaging, i.e. from the average diameter of the nanospheres).
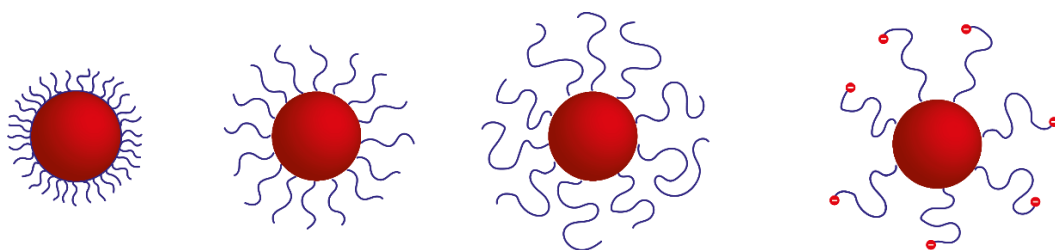
Figure 28 Schematic representation of the coating of AuNP with different HS-PEG, illustrating how the coverage decreases with increasing PEG length (left) and how the coverage achieved for a HS-PEG-COOH is lower than with the correspondent HS-PEG with the same mw (right).

It is evident from the values reported in Table 4 that the amount of PEG molecules present on a single NP decreases with increasing the length of the polymer chain. This trend can be attributed to a hindering effect, both on the available surface on the AuNP by the already grafted molecules and on the thiol group of the incoming ones, an effect that is more relevant for longer chains. Finally, for the same PEG molecular weight, a lower coverage is achieved when -COOH is present, most probably due to the repulsion between the charged end groups (Figure 28).

3.3.2 Potentiometric studies

3.3.2.1 Protonation constants determination of free PEG molecules

As preliminary experiments, with the perspective of studying the behavior of thiol-PEG molecules grafted on AuNP, potentiometric titrations of various HS-PEG, and HS-PEG-COOH free molecules have been performed in order to determine their protonation constants. A series of analogue molecules with different molecular weights have been studied for each class, ranging from the smallest ones, with few monomeric units (formally not PEG but oligo-ethylene glycols), up to medium-length chains of hundreds of EG units (mw of few thousands). The general structures of the examined molecules are shown in Figure 29. The screening allowed to appreciate the effect of the PEG chain length on the acidity of the terminal functional groups. PEG-COOH have also been examined for comparison, to better evaluate the effect on the two distinct groups.
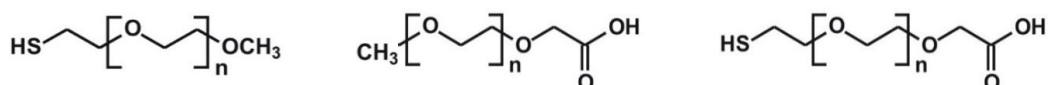
Figure 29 General structures of HS-PEG (left), PEG-COOH (middle) and HS-PEG-COOH (right) molecules.

Table 5 pKa values for a series of PEG-COOH, HS-PEG and HS-PEG-COOH molecules obtained from the fitting of potentiometric titration curves

	MW	n	pK_{a1}	pK_{a2}
	90	0	3.85(2)	-
	134	1	3.85(2)	-
PEG-COOH	178	2	3.86(2)	-
	589	11	4.56(1)	-
	5000	112	4.78(1)	-
	136	1	-	9.49(2)
	350	6	-	9.51(2)
HS-PEG	750	15	-	9.62(4)
	2000	44	-	9.4(2)
	5000	112	-	9.34(7)
	282	4	4.44(2)	9.67(2)
	459	7	4.47(2)	9.70(2)
HS-PEG-COOH	3000	64	4.7(1)	9.6(1)
	5000	110	4.8(1)	9.5(2)

The potentiometric titration profile (pH vs added base volume) of a solution of the molecule of interest at a known concentration, obtained as described in detail in 3.2.3.1, and fitting of the resulting curve with the Hyperquad software package[136] allowed to derive its pK_a values.

Results obtained from titration of 0.5 mM solutions are presented in Table 5. Data for 0.1 mM solutions are not reported, because in most cases the concentration of the weak acid was too low to observe a titration profile different from that of a strong acid with a strong base (and constants could not be determined by the fitting program). On the other hand, data for 1 mM solutions are incomplete

(results for HS-PEG-COOH are missing for a shortage of materials; as an example, 20 mL of 1mM solution of HS-PEG-5000 would require a solution containing 100 mg of product).

The increasing length of the molecules yields an evident shift of pK_{a1} to higher values. This could be attributed to the possibility for the -COOH to establish intramolecular interactions with longer PEG chains as well as to the higher entropic cost needed to expose the terminal group towards the solvent once deprotonated. Both effects are related to a higher flexibility and conformational variability of longer molecules, that eventually cause the observed decrease of their apparent acidity by "trapping" or hiding the hydrophilic –COOH group, e.g. by H-bond interactions with the non-bonding couples of the –O– units. On the contrary, no clear trend can be noticed for the -SH group, coherently with the lower electronegativity of the S atom, not allowing H-bond interactions.

3.3.2.2 Potentiometric titrations of AuNP@HS-PEG-COOH

The following step was of course to attempt potentiometric titrations on HS-PEG-COOH grafted on the surface of AuNP, for the purpose of understanding how the properties of the coating molecules are affected when confined on the surface of the nanoparticles.

In particular, the aim was to determine the variation of the acidity of AuNP-bound HS-PEG-COOH with respect to the free molecules (Figure 30), given that the –SH acid/base behavior is not observable, due to the stability (at least at 20 °C) of the S-Au bond.
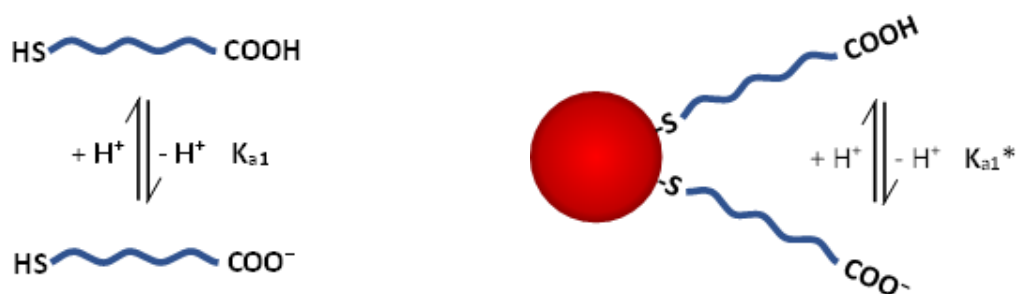
Figure 30 Schematic representation of the protonation equilibrium for the carboxylic acid of a general HS-PEG-COOH free molecule (left) and when grafted to AuNP

Significant experimental problems were encountered. For example, considering AuNP coated with HS-PEG-COOH with mw 5000, PEG is only 10% w/w of the coated particle, as we have seen from TGA data. A 0.1 mM concentration of such PEG in 20 mL of titrating solution requires 10 mg of the polymer and, consequently, ~ 90 mg of Au, that is a huge quantity and an unusually high concentration for a gold colloidal solution. Therefore, highly concentrated solutions of pegylated AuNP had to be prepared in order to get a barely sufficient ligand concentration ($> 10^{-4}$ M) for the detection of the protonation equilibrium of the -COOH group and the determination of its constant.

The starting AuNP solutions (2.5 L) have been intensively purified after pegylation, concentrated 100 times and then titrated (see experimental details in 3.2.3.2). The experiment has been performed on AuNP@HS-PEG$_{5000}$-COOH and AuNP@HS-PEG$_{3000}$-COOH. The concentration of PEG in the final colloidal solutions was 0.12 mM and 0.25 mM, respectively. Figure 31 shows both experimental and calculated titration curves for the latter sample.
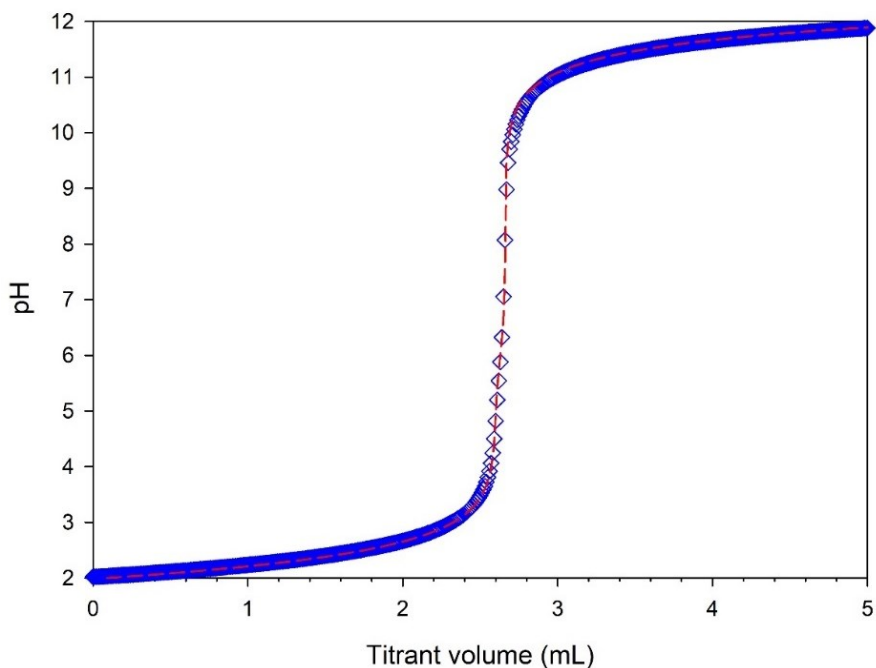
Figure 31 Potentiometric titration curve (pH vs mL) for AuNP@HS-PEG$_{3000}$-COOH; observed data are indicated in blue, red dashed line is the fitted curve.

The actual situation in these samples is complex, as the molecules grafted on a single AuNP are confined on a limited space and are then somehow affected by the surrounding environment. In particular, different carboxylic groups can interact between themselves, so that they cannot be considered as independent. The deprotonation of one -COOH affects the equilibrium of those of its neighboring molecules, as a negative charge adds up in the system, making the following deprotonations less favorable. This, in turn, leads to a progressive shift of the single protonation constants to higher pK$_a$ values, i.e. a decrease in the acidity, generating overall a distribution of close yet different values. So, the AuNP@HS-PEG-COOH system ought to be considered as a whole, as characterized by multiple equilibria that can also vary in the course of the experiment.

However, given the inconvenience of setting countless similar protonation constants, not to mention the difficulty in determining them numerically, a simpler model with a single constant was adopted. This is intended as an apparent constant, representative of the average situation of the more complex system. The constant related to the thiol function of the PEG was not considered in the model, as its protonation is supposed not to occur at working conditions (starting pH around 2), with the sulfur atom remaining firmly bound to the Au surface. This is confirmed by the stability of the AuNP throughout the whole experiment, since protonation would otherwise lead to the detachment of the coating molecules and therefore to a general destabilization of the colloidal solution. Moreover, a titration was carried out also on a colloidal solution of AuNP coated with HS-PEG$_{5000}$-OCH$_3$, i.e. with no acid/base functions. Beside some interference due to citrate (that was not accurately eliminated in this first experiment), the reassuring data was that no titration curve inflection was observed in the pH range in which -SH groups are expected to undergo deprotonation (8-10), a further indication that no significant HS-PEG release from AuNP occurs.

In both experiments, a clear increase of more than 1 unit of the carboxylic acid pK$_a$ was observed. In particular, similar values of 5.9(4) for AuNP@HS-PEG$_{5000}$-COOH and 6.0(7) for AuNP@HS-PEG$_{3000}$-COOH were found, corresponding to a shift of 1.1 and 1.3 units, respectively, relative to the values for the free molecule (see Table 5 for comparison). The fact that the obtained values are only indicative of a broader distribution of pK$_a$ is reflected in the higher standard deviation associated to these values compared to those obtained for the free molecules. The slightly stronger variation in the case of AuNP@HS-PEG$_{3000}$-COOH could be related to the higher NP coverage given by this molecule, as observed in 3.3.1.2. As a matter of fact, a

"denser" coating layer would increase interactions between nearby molecules, making the deprotonation accordingly more difficult.

3.4 CONCLUSIONS

The coating of gold nanoparticles with different PEG thiols has been thoroughly investigated. Spherical AuNP have been coated with various HS-PEG and HS-PEG-COOH of different molecular weights and examined by Dynamic Light Scattering (DLS) and Thermogravimetric Analysis (TGA) to study the properties of the coated AuNP. Size, zeta potential and PEG coverage results, in terms of average number of molecules per particle, all show a clear correlation with the molecular weight of the polymer. In particular, the latter parameter is affected by the steric hindrance of longer chains, that prevent an easier access to the NP surface of other molecules and their closer arrangement, as in the case of smaller molecules.

Potentiometric titrations of HS-PEG, PEG-COOH and HS-PEG-COOH molecules allowed to determine their protonation constants. Even in this case, a trend related to the different molecular weight was observed in the pK_a values. In particular, the acidity of the carboxylic acid decreases with increasing length of the polymer chain, probably as an effect of increased intramolecular H-bonds, hindering the deprotonation process.

Eventually, two different AuNP@HS-PEG-COOH samples have been titrated, demonstrating a further shift of the apparent pK_a of the -COOH groups to higher values when confined on the AuNP. The simplest interpretation is that this phenomenon occurs because the tendency of each functional PEG to undergo deprotonation is affected by the presence of other nearby molecules grafted on the NP surface and decreases in the course of the experiment (depending on the degree of dissociation of the system). So, the obtained constants are only averaged values

of a complex situation, where this interaction between neighboring molecules generates a distribution of multiple different protonation constants.

As future perspectives, further titrations of AuNP coated with non-functional HS-PEG may be performed as a control, to confirm that the thiolate group is in any case (i.e. independently on the chain length) still bound to the Au surface and does not present any acid/base activity and, in general, to better understand the whole system and the significance of such experiments.

However, the complex procedure of purification and concentration needed to obtain a suitable sample for potentiometric titration is quite demanding in terms of time and materials and not so mild on the colloidal solution. For this reason, it appears quite unfeasible to perform it on all the other possible samples coated with the different thiol-PEG available. Therefore, an alternative approach seems necessary for a more practical/convenient screening of the set of PEG molecules considered that could be grafted on AuNP. A possible option would be to exploit DLS to perform zeta potential titrations, that could as well give some indication on the collective behavior of the functional groups on the coating. This method should then allow faster measurements, as it can be applied on as-prepared pegylated AuNP, thus not requiring strong concentration of the samples. If effective, this could serve as a preliminary screening to plan potentiometric experiments aimed at selected samples.

PART 4. PHOTOTHERMAL PDMS SPONGES

4.1 BACKGROUND

In recent years porous materials have received an increasing attention in literature, often with the purpose to mimic natural occurring porous structures. A variety of materials have been developed, starting from inorganic zeolites, active carbon, porous silicates, to hybrid metal-organic frameworks (MOFs) and porous organic polymers (POPs).[137,138] Porous polymers have been particularly studied as they combine typical properties of porous structures, such as large surface area and well-defined porosity, with the advantages of polymeric materials, namely the ease in processability, with multiple possible routes for their fabrication and functionalization. The use of porous polymeric materials has been developed for various applications, such as greenhouse gas adsorption, proton conduction, energy storage and conversion, sensing, separation, catalysis, drug delivery and tissue engineering.[139–145]

4.1.1 PDMS-based porous materials

Among many possible porous polymeric materials, the growing research interest on polydimethylsiloxane (PDMS) sponges is based on the remarkable properties of this polymer. Indeed, PDMS has been the most widely used silicon-based organic elastomer since the first silicones were synthesized by Wacker Chemie in the 1950s. Its viscoelasticity, biocompatibility, chemical and mechanical resistance, low glass transition temperature, high cost-effectiveness and good moldability, promoted its widespread practical use. The Si–O–Si backbone (see Figure 32 for the structure) provides high flexibility, non-toxicity, non-flammability, thermal and electrical resistance, and low bulk density. PDMS ensures high transmittance and low UV absorption, making it suitable for fine optical applications.[146]
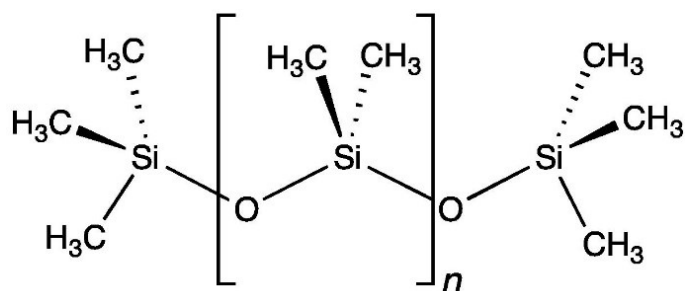
Figure 32 General structural formula of a linear polydimethylsiloxane (PDMS).

Because of its excellent contour accuracy of less than 10 nm, it is widely employed in micro- and nanofabrication.[147] PDMS is resistant against most aqueous reagents and alcohols, while organic solvents, such as xylene, are able to give swelling.[148] In addition, it is permeable to small unreactive vapor and gas molecules such as water and oxygen. The surface of pristine PDMS is hydrophobic, presenting a low surface tension. However, its wettability can be increased on purpose, with the introduction of hydroxyl groups by oxygen plasma treatment; this also enables the further functionalization of the surface.[149,150] However, this modification is temporary, as it regains its hydrophobic properties owing to chain migration.[151]

Different approaches can be followed to generate the porous structures in PDMS sponges, such as template leaching, phase separation, gas foaming or 3D printing.[152] The appropriate fabrication method, yielding materials with the required structural characteristics (total porosity, pore size, geometry and distribution, etc.). should be selected according to the desired functions; not every fabrication method could meet the needs of the intended application. The template leaching approach involve generally the use of sugar cubes (or other macroscopic objects with a definite shape) to assist the infiltration of the liquid pre-curing mixture (SYLGARD™ 184 Silicone Elastomer Kit) into the voids of the sacrificial template. Then, the PDMS-soaked cubes are cured in an oven to complete PDMS

polymerization and eventually the sugar template is leached out by water, giving a 3D interconnected porous polymeric structure. The pore size and porosity of the PDMS sponges can be tuned by varying the particle size in the template and the mixing ratio with the PDMS precursors. The typical pore size obtained by sugar leaching techniques is in the range from tens to hundreds of μm. The fabrication of PDMS sponges with optimized performance for oil absorption has been already reported using sugar crystals[153] or NaCl microcrystals[154] of different sizes to obtain the templates. More recently, an alternative leaching method was described, employing citric acid and ethanol as solvent, which is capable of wetting PDMS, thus optimizing the template removal. Accordingly, the obtained sponges presented high performances in oil absorption.[155] Other sacrificial templates, such as polystyrene (PS) microspheres with specific dimensions, have been reported for generating fine-tuned porous structures.[156] A major drawback in these cases is the need of hazardous solvents for the leaching of the templates.

The possibility to functionalize the PDMS sponges, either by inclusion of active components or by modification of the pores surface, provide these materials with extensive scope for application as flexible conductors, sensors, energy generators and storage devices, adsorbents, oil/water separators, biomedical scaffolds.[152] The inclusion of photothermally active nanoparticles, for instance, is a promising way for the production of materials for efficient solar energy harvesting and conversion.[35] In continuity with the inclusion of photothermal GNS in polymeric films studied in the first part of the PhD research, the inclusion of such active plasmonic nanoparticles was also studied during the PhD period, in particular with the perspective of obtaining floating materials for solar-driven water evaporation.

Solar-driven evaporation is a growing technology with many potential applications including desalination, power generation, purification, sterilization, and phase separation.[157] Recently, a PDMS porous material containing carbon nanoparticles (CNPs) has been produced by Wang et al. via salt-leaching technique and tested as an interfacial receiver for solar-driven water evaporation.[158] The inclusion of CNPs significantly increases the solar absorptivity of the material to ~97% without impacting their inherently low thermal conductivity. Modification with polyvinyl alcohol (PVA) was carried out to impart hydrophilicity to the porous structure, enabling continuous water transport to the air-water interface. GNS have been already successfully embedded in bulk PDMS in our laboratory, by coating them with HS-PEG-OMe (mw 5000) and dispersing in THF or ethanol. In this way, photothermally active PDMS films were produced, capable of exerting a good microbicidal action against *E. coli* upon laser irradiation at 800 nm.[71] This prompted me to study the preparation of PDMS sponges containing the same kind of photothermal gold nanoparticles.

4.2 EXPERIMENTAL DETAILS

4.2.1 Materials and instrumentation

4.2.1.1 Reagents

Gold(III) chloride solution 99.99% (30 wt. % in dilute HCl); Triton™ X-100 (laboratory grade); Silver nitrate ACS reagent, ≥99.0%; Sodium borohydride ≥98.0%; L-Ascorbic acid ≥99.0%; Poly(ethylene glycol) methyl ether thiol (HS-PEG-OMe, mw 5000); Tetrahydrofuran, ≥99.9% were all purchased from Merck Life Sciences (Milano, Italy). SYLGARD™ 184 Silicone Elastomer Kit was supplied by Dow Chemical (Midland, MI, USA). Kitchen sugar (sucrose) was purchased from a local supermarket. All reagents were used without further purification.

4.2.1.2 Glassware pre-treatment

All the glassware used in the syntheses was pre-treated with *aqua regia* for 15 minutes and then washed three times with bidistilled water in an ultrasound bath for 5 minutes.

4.2.1.3 Instrumental procedures

Ultracentrifugation
Ultracentrifugation was carried out using the ultracentrifuge Hermle Z366 with polypropylene 10 mL tubes.

UV-Vis-NIR spectroscopy
Absorption spectra were recorded on a Varian Cary 60 spectrophotometer in 1 cm optical glass cuvettes.

Thermal images were taken with a FLIR E40 thermal camera with FLIR Tools+ dedicated software for data acquisition and analysis. Different regions of interest (ROI) were defined, each comprising a single irradiated sample, and the maximum temperatures inside each ROI (±0.1 °C accuracy) were determined for all the thermal images recorded. Thermal images were acquired at 1 fps rate for 200 seconds.

4.2.2 PDMS sponges preparation

4.2.2.1 GNS synthesis

GNS were prepared according to the same general method described in Part 1.[53] In detail, a seed solution was first obtained by mixing 5.0 mL of 0.2 M Triton X-100 with 5.0 mL of 0.5 mM $HAuCl_4$ and then quickly adding 600 µL of ice-cooled 0.01 M $NaBH_4$. The resulting light orange solution was kept in an ice bath and used within 1 hour. For the growth, 50 mL of 0.2 M Triton X-100 were put in a 250 mL flask under magnetic stirring at room temperature and then the following additions were made in a fast and sequential fashion: 2.5 mL $AgNO_3$ 4 mM, 50 mL $HAuCl_4$ 1 mM, 1.7 mL ascorbic acid 78.8 mM and finally 120 µL of a freshly prepared seed solution. The solution quickly turned from pale yellow to colorless and, after the last addition, to violet and eventually blue-black color, at which point stirring was stopped. However, the growing process was allowed to proceed and considered complete after 2 hours.

4.2.2.2 GNS coating and purification

The obtained GNS were then coated with HS-PEG (mw 5000) by adding to the colloidal solution the proper amount of thiol to give a $2×10^{-5}$ M final concentration

and allowing to react for at least 3 hours at room temperature. After that, 10 mL of the pegylated GNS were purified by ultracentrifugation at 13000 rpm (15870 rcf) for 25 min. The colorless supernatant was discarded and the pellet redissolved in 10 mL of fresh water. The procedure was repeated three times, with the aim of removing all the surfactant and other subproducts from the synthesis, but after the last cycle the pellet was dried under a gentle N_2 flow and then redispersed in 100 μL of THF.

4.2.2.3 Production of PDMS-GNS sponges

First, sacrificial templates for PDMS were obtained by packing the sugar, with the addition of few drops of water (~ 1% w/w), in a silicone mold. After drying in an oven at 60°C for 4 hours, the templates were extracted from the mold and were ready to use. PDMS precursor mixture was obtained according to the manufacturer instructions, mixing the two components of the kit, base elastomer and curing agent, in a 10:1 weight ratio. For the preparation of PDMS sponges with GNS embedded, 100 μL of the concentrated GNS suspension in THF were added to 5 g of the polymer mixture, stirring until uniform distribution of the GNS was achieved. Then, the mixture was casted into a Petri dish and a sugar template was dipped in it, keeping everything under vacuum in a desiccator for 2 hours to allow the degassing of the polymer mixture and its full permeation in the template. The PDMS-soaked templates were then heated in an oven at 45 °C overnight to allow the curing process of the polymer. The cross-linked samples were then placed in a bidistilled water bath until the complete dissolution of the sugar templates, giving the final PDMS sponges with GNS included. Blank PDMS sponge samples were obtained by the same procedure without the addition of any NP.

4.3 RESULTS AND DISCUSSION

4.3.1 Photothermal PDMS sponges

4.3.1.1 GNS

Gold nanostars were prepared according to the same method described in the first part.[53] For a detailed description and characterization of GNS refer to 2.3.1.2. Since as-prepared GNS would not withstand ultracentrifugation, leading to irreversible aggregation, coating with a thiolated polyethylene glycol (HS-PEG) is necessary to perform the purification of the colloidal suspension, that is required to remove all the by-products from the synthesis and in particular the excess of the Triton X-100 surfactant. The grafting of HS-PEG molecules on the GNS surface allows the nanoparticles not only to withstand repeated ultracentrifugation cycles, but also to be dried, handled as a powder and then be readily redispersed in a variety of solvents, including non-hydrophilic ones.[53] Concentrated GNS solutions can be obtained as well, by simply adding the desired small volume of the selected dispersant to a dry pellet of PEG-coated GNS.

In this case, GNS were coated with a methoxy-terminated thiol PEG (mw 5000) and, after 3 cycles of ultracentrifugation, redispersed in THF using 1/100 of the original water volume, obtaining a concentrated solution in THF, a non-aqueous solvent that is miscible with the components of the PDMS precursor kit (see below). The absorption spectra of GNS-PEG in water (black line) and in THF after purification (red line) are displayed in Figure 33. Given that the spectrum in THF has been recorded in such a volume to have the original GNS concentration, the absorbance of the LSPR band around 800 nm should be identical. However, the repeated ultracentrifugation procedure caused a noticeable loss of material, that is responsible of the lower absorption.
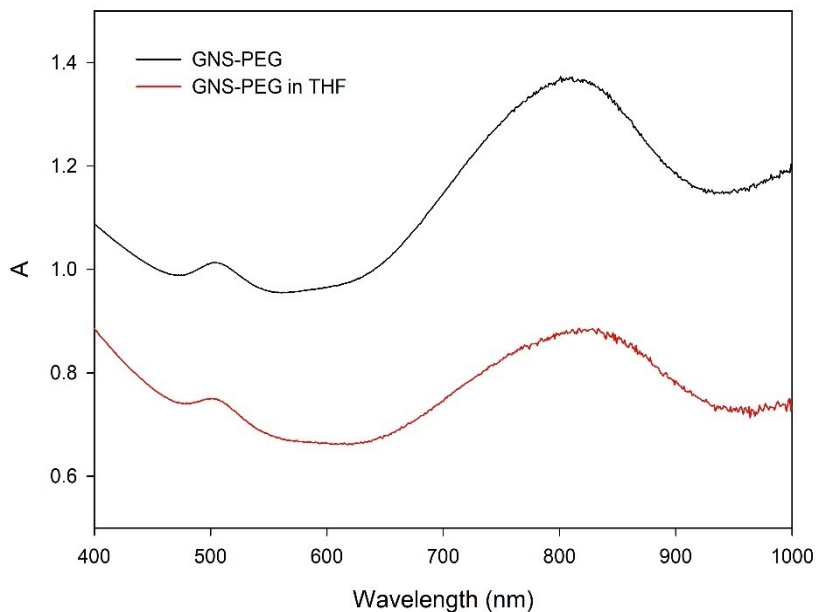
Figure 33 Extinction spectra of GNS@HS-PEG5000 in water (black line) and in THF (red line), after purification.

4.3.1.2 PDMS sponges

Polydimethylsiloxane (PDMS) was employed to produce porous sponge-like scaffolds via a simple templating method. Common sugar (sucrose) has been used here as sacrificial template to absorb the PDMS precursor mixture via capillary forces and thus support its curing process, yielding the formation of a self-standing PDMS structure. The hydrophobic nature of PDMS allows the use of a water-soluble template, which can be easily dissolved after curing the polymer, leaving a network of highly interconnected pores in the resulting PDMS scaffolds (Figure 35).
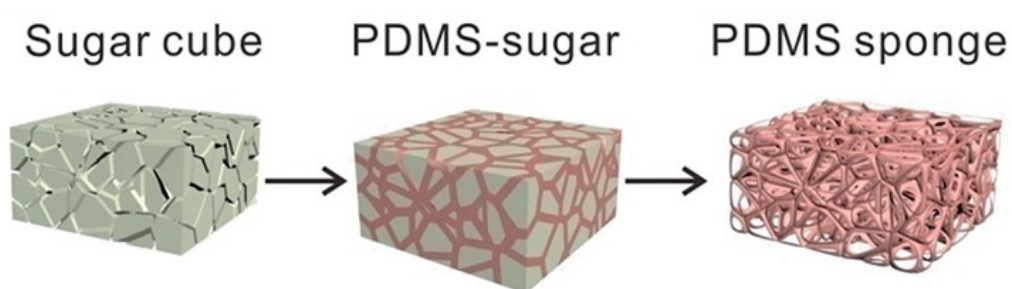
Figure 35 Schematic representation of the templating process for the preparation of PDMS sponges.
[152]

By the inclusion of GNS, photothermally active PDMS sponges have been produced. As mentioned above, GNS need to be coated with a HS-PEG to be transferred in a solvent compatible with PDMS, such as THF, allowing their efficient dispersion in the polymer mixture.[71] A small amount of the concentrated GNS-PEG solution in THF obtained by ultracentrifugation has been added to the precursor mixture. By curing at 45°C overnight, the cross-linking reaction in PDMS is promoted, and the polymer structure is consolidated. At this point, the templates have been leached in water, to obtain self-standing **PDMS-GNS** sponges. A reference blank sample has been also prepared, without the addition of any GNS in the mixture. Pictures of the obtained samples are shown in Figure 34.
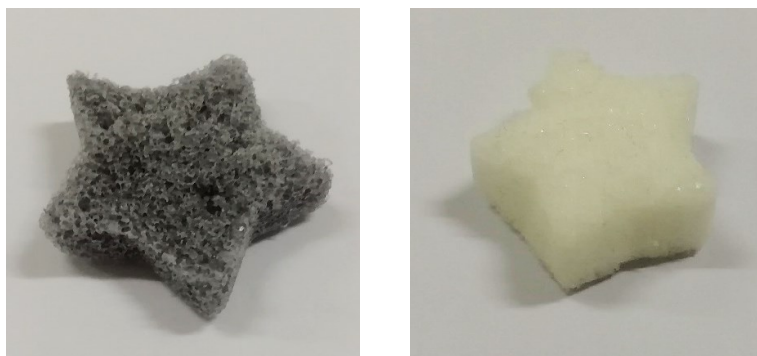
Figure 34 Appearance of the obtained PDMS sponges with GNS-PEG
embedded (left) and without (blank sample, right)

4.3.1.3 Solar photothermal response

The photothermal effect of the produced PDMS sponges has been tested directly under natural solar irradiation. Thermograms and thermal images reported in Figure 36 have been recorded with the help of a thermal camera, according to the procedure described in 2.2.1.3.
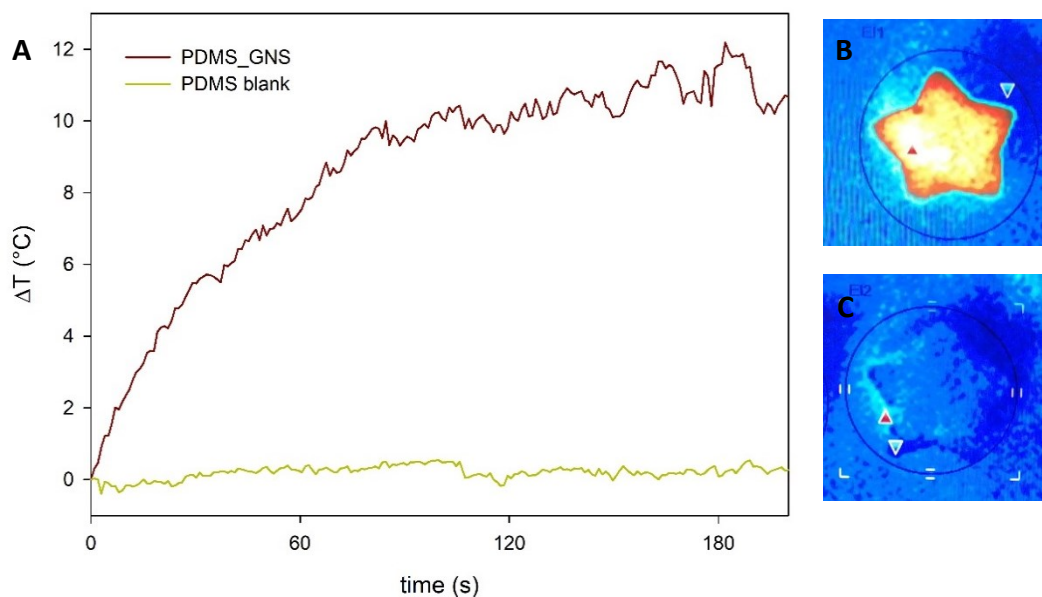
Figure 36 (A) Thermograms (ΔT vs time) obtained by solar irradiation of PDMS sponges with GNS (dark line) and without (blank sample, light line). (B) Thermal image of the sample containing GNS at 180 s of irradiation; (C) same, for blank PDMS sample.

As can be noticed in Figure 36A (dark line), the temperature of **PDMS-GNS** rapidly increases, reaching a plateau after 2 minutes. The maximum temperature measured on the sample is around 35°C, corresponding to a ΔT of 12 °C. The oscillations present in the curve are likely due to the slight variations of the solar irradiance and to the modifications of the atmospheric conditions in general, that cannot be controlled. The simultaneous irradiation of **PDMS-blank** did not produce any heating of the sample (ΔT ~ 0), as expected (light line). Figure 36B and C show a thermal image of the two samples, respectively, after 180 s of irradiation.

4.4 CONCLUSIONS

In the last part of my PhD, porous PDMS scaffolds were prepared with a simple template leaching procedure. PDMS sponges with GNS embedded were obtained for the first time. The homogeneous dispersion of GNS in the polymer was made possible by their coating with thiol-PEG molecules (mw 5000) and transfer to THF. The resulting material is very elastic and possess high absorption capacity. Moreover, it floats over water without sinking. These properties, together with its hydrophobicity and biocompatibility, make it suitable for oil separation/water decontamination, and vapour production by direct solar light absorption. However, due to lack of time and unavailability of proper instrumentation, an accurate characterization in terms of mechanical properties, porosity, pore size and morphology could not be performed within my PhD research period, and it will be necessary for a finer tuning of the final material properties. In addition, control of the pore size and porosity could be achieved by modulation of the template particle size and packing.

However, it was possible to measure the photothermal response of the PDMS sponges under real solar irradiation. Samples containing GNS presented an interesting temperature increase of more than 10°C, reached within 2 minutes, while blank samples showed no heating, as expected. The irradiation with natural solar light, as it was performed, present some limitations due to the poor control on the experimental conditions, such as the solar irradiance and the atmospheric conditions, that are always subjected to some oscillations. Such experiments would best be performed in a solar simulator, that would allow a fine control of all the parameters. However, this simple experiment is a clear indication of the heating efficiency of these materials when used in real life conditions. Moreover, it would

be certainly worth exploring different amount of included GNS, trying to enhance the photothermal response, or even to use different photothermal particles.

While such porous materials could serve as solar evaporators, by thermally converting solar power to promote interfacial water evaporation, or as devices for oil separation and decontamination of water, the possibility to exploit the photothermal effect of the PDMS-GNS sponges to degrade absorbed hydrophobic pollutants, such as dyes or pesticides, still waits to be verified.

References

(1)   Schexnailder, P.; Schmidt, G. Nanocomposite Polymer Hydrogels. *Colloid Polym. Sci.* **2009**, *287* (1), 1–11. https://doi.org/10.1007/S00396-008-1949-0/FIGURES/1.

(2)   Pastoriza-Santos, I.; Kinnear, C.; Pérez-Juste, J.; Mulvaney, P.; Liz-Marzán, L. M. Plasmonic Polymer Nanocomposites. *Nat. Rev. Mater.* **2018**, *3* (10), 375–391. https://doi.org/10.1038/s41578-018-0050-7.

(3)   Thoniyot, P.; Tan, M. J.; Karim, A. A.; Young, D. J.; Loh, X. J. Nanoparticle-Hydrogel Composites: Concept, Design, and Applications of These Promising, Multi-Functional Materials. *Adv. Sci.* **2015**, *2* (1–2), 1400010. https://doi.org/10.1002/advs.201400010.

(4)   Pardo-Yissar, V.; Gabai, R.; Shipway, A. N.; Bourenko, T.; Willner, I. Gold Nanoparticle/Hydrogel Composites with Solvent-Switchable Electronic Properties. *Adv. Mater.* **2001**, *13* (17), 1320–1323. https://doi.org/10.1002/1521-4095(200109)13:17<1320::AID-ADMA1320>3.0.CO;2-8.

(5)   Tokarev, I.; Tokareva, I.; Gopishetty, V.; Katz, E.; Minko, S. Specific Biochemical-to-Optical Signal Transduction by Responsive Thin Hydrogel Films Loaded with Noble Metal Nanoparticles. *Adv. Mater.* **2010**, *22* (12), 1412–1416. https://doi.org/10.1002/ADMA.200903456.

(6)   Endo, T.; Ikeda, R.; Yanagida, Y.; Hatsuzawa, T. Stimuli-Responsive Hydrogel–Silver Nanoparticles Composite for Development of Localized Surface Plasmon Resonance-Based Optical Biosensor. *Anal. Chim. Acta* **2008**, *611* (2), 205–211. https://doi.org/10.1016/J.ACA.2008.01.078.

(7)   Saravanan, P.; Padmanabha Raju, M.; Alam, S. A Study on Synthesis and Properties of Ag Nanoparticles Immobilized Polyacrylamide Hydrogel Composites. *Mater. Chem. Phys.* **2007**, *103* (2–3), 278–282. https://doi.org/10.1016/J.MATCHEMPHYS.2007.02.025.

(8)   Lu, Y.; Spyra, P.; Mei, Y.; Ballauff, M.; Pich, A. Composite Hydrogels: Robust Carriers for Catalytic Nanoparticles. *Macromol. Chem. Phys.* **2007**, *208* (3),

254–261. https://doi.org/10.1002/MACP.200600534.

(9)   Zhao, X.; Ding, X.; Deng, Z.; Zheng, Z.; Peng, Y.; Tian, C.; Long, X. A Kind of Smart Gold Nanoparticle –Hydrogel Composite with Tunable Thermo-Switchable Electrical Properties. *New J. Chem.* **2006**, *30* (6), 915–920. https://doi.org/10.1039/B601069E.

(10)   You, J. O.; Auguste, D. T. Conductive, Physiologically Responsive Hydrogels. *Langmuir* **2010**, *26* (7), 4607–4612. https://doi.org/10.1021/LA100294P/SUPPL_FILE/LA100294P_SI_001.PDF.

(11)   Wang, J.; Banerji, S.; Menegazzo, N.; Peng, W.; Zou, Q.; Booksh, K. S. Glucose Detection with Surface Plasmon Resonance Spectroscopy and Molecularly Imprinted Hydrogel Coatings. *Talanta* **2011**, *86* (1), 133–141. https://doi.org/10.1016/J.TALANTA.2011.08.046.

(12)   Marsich, E.; Travan, A.; Donati, I.; Di Luca, A.; Benincasa, M.; Crosera, M.; Paoletti, S. Biological Response of Hydrogels Embedding Gold Nanoparticles. *Colloids Surfaces B Biointerfaces* **2011**, *83* (2), 331–339. https://doi.org/10.1016/J.COLSURFB.2010.12.002.

(13)   Skirtach, A. G.; Dejugnat, C.; Braun, D.; Susha, A. S.; Rogach, A. L.; Parak, W. J.; Möhwald, H.; Sukhorukovt, G. B. The Role of Metal Nanoparticles in Remote Release of Encapsulated Materials. *Nano Lett.* **2005**, *5* (7), 1371–1377. https://doi.org/10.1021/NL050693N/SUPPL_FILE/NL050693NSI20050414_035917.AVI.

(14)   Shiotani, A.; Mori, T.; Niidome, T.; Niidome, Y.; Katayama, Y. Stable Incorporation of Gold Nanorods into N-Isopropylacrylamide Hydrogels and Their Rapid Shrinkage Induced by near-Infrared Laser Irradiation. *Langmuir* **2007**, *23* (7), 4012–4018. https://doi.org/10.1021/LA0627967/SUPPL_FILE/LA0627967SI20061126_095352.PDF.

(15)   Tokarev, I.; Tokareva, I.; Minko, S. Gold-Nanoparticle-Enhanced Plasmonic Effects in a Responsive Polymer Gel. *Adv. Mater.* **2008**, *20* (14), 2730–2734. https://doi.org/10.1002/ADMA.200702885.

(16)   Liu, J.; Hurt, R. H. Ion Release Kinetics and Particle Persistence in Aqueous

Nano-Silver Colloids. *Environ. Sci. Technol.* **2010**, *44* (6), 2169–2175. https://doi.org/10.1021/es9035557.

(17)   Pallavicini, P.; Preti, L.; De Vita, L.; Dacarro, G.; Diaz Fernandez, Y. A.; Merli, D.; Rossi, S.; Taglietti, A.; Vigani, B. Fast Dissolution of Silver Nanoparticles at Physiological PH. *J. Colloid Interface Sci.* **2020**, *563*, 177–188. https://doi.org/10.1016/j.jcis.2019.12.081.

(18)   Nowack, B.; Krug, H. F.; Height, M. 120 Years of Nanosilver History: Implications for Policy Makers. *Environ. Sci. Technol.* **2011**, *45* (4), 1177–1183. https://doi.org/10.1021/ES103316Q/SUPPL_FILE/ES103316Q_SI_001.PDF.

(19)   Chernousova, S.; Epple, M. Silver as Antibacterial Agent: Ion, Nanoparticle, and Metal. *Angew. Chemie Int. Ed.* **2013**, *52* (6), 1636–1653. https://doi.org/10.1002/anie.201205923.

(20)   17870 results in a search on Web Of Science for "silver nanoparticles" and "antibacterial" https://www.webofscience.com/wos/woscc/summary/198e4fe2-e45e-4037-b401-a6f13498f0fb-204e0a06/relevance/1 (accessed Feb 23, 2022).

(21)   Vasilev, K.; Cook, J.; Griesser, H. J. Antibacterial Surfaces for Biomedical Devices. *Expert Rev. Med. Devices* **2009**, *6* (5), 553–567. https://doi.org/10.1586/erd.09.36.

(22)   Pallavicini, P.; Dacarro, G.; Taglietti, A. Self-Assembled Monolayers of Silver Nanoparticles: From Intrinsic to Switchable Inorganic Antibacterial Surfaces. *Eur. J. Inorg. Chem.* **2018**, *2018* (45), 4846–4855. https://doi.org/10.1002/ejic.201800709.

(23)   D'Agostino, A.; Taglietti, A.; Desando, R.; Bini, M.; Patrini, M.; Dacarro, G.; Cucca, L.; Pallavicini, P.; Grisoli, P.; D'agostino, A.; Taglietti, A.; Desando, R.; Bini, M.; Patrini, M.; Dacarro, G.; Cucca, L.; Pallavicini, P.; Grisoli, P. Bulk Surfaces Coated with Triangular Silver Nanoplates: Antibacterial Action Based on Silver Release and Photo-Thermal Effect. *Nanomaterials* **2017**, *7* (1), 7. https://doi.org/10.3390/nano7010007.

(24)   Dacarro, G.; Cucca, L.; Grisoli, P.; Pallavicini, P.; Patrini, M.; Taglietti, A. Monolayers of Polyethilenimine on Flat Glass: A Versatile Platform for

Cations Coordination and Nanoparticles Grafting in the Preparation of Antibacterial Surfaces. *Dalt. Trans.* **2012**, *41* (8), 2456. https://doi.org/10.1039/c1dt11373a.

(25) Salomé Veiga, A.; Schneider, J. P. Antimicrobial Hydrogels for the Treatment of Infection. *Biopolymers* **2013**, *100* (6), 637–644. https://doi.org/10.1002/bip.22412.

(26) Silvestre, C.; Duraccio, D.; Cimmino, S. Food Packaging Based on Polymer Nanomaterials. *Prog. Polym. Sci.* **2011**, *36* (12), 1766–1782. https://doi.org/10.1016/j.progpolymsci.2011.02.003.

(27) de Azeredo, H. M. C. Antimicrobial Nanostructures in Food Packaging. *Trends Food Sci. Technol.* **2013**, *30* (1), 56–69. https://doi.org/10.1016/j.tifs.2012.11.006.

(28) Li, Q.; Mahendra, S.; Lyon, D. Y.; Brunet, L.; Liga, M. V.; Li, D.; Alvarez, P. J. J. Antimicrobial Nanomaterials for Water Disinfection and Microbial Control: Potential Applications and Implications. *Water Res.* **2008**, *42* (18), 4591–4602. https://doi.org/10.1016/j.watres.2008.08.015.

(29) Lau, W. J.; Gray, S.; Matsuura, T.; Emadzadeh, D.; Paul Chen, J.; Ismail, A. F. A Review on Polyamide Thin Film Nanocomposite (TFN) Membranes: History, Applications, Challenges and Approaches. *Water Res.* **2015**, *80*, 306–324. https://doi.org/10.1016/j.watres.2015.04.037.

(30) Sulaeva, I.; Henniges, U.; Rosenau, T.; Potthast, A. Bacterial Cellulose as a Material for Wound Treatment: Properties and Modifications. A Review. *Biotechnol. Adv.* **2015**, *33* (8), 1547–1571. https://doi.org/10.1016/j.biotechadv.2015.07.009.

(31) Kumar, S. S. D.; Rajendran, N. K.; Houreld, N. N.; Abrahamse, H. Recent Advances on Silver Nanoparticle and Biopolymer-Based Biomaterials for Wound Healing Applications. *Int. J. Biol. Macromol.* **2018**, *115*, 165–175. https://doi.org/10.1016/j.ijbiomac.2018.04.003.

(32) Pallavicini, P.; Arciola, C. R.; Bertoglio, F.; Curtosi, S.; Dacarro, G.; D'Agostino, A.; Ferrari, F.; Merli, D.; Milanese, C.; Rossi, S.; Taglietti, A.; Tenci, M.; Visai, L. Silver Nanoparticles Synthesized and Coated with

Pectin: An Ideal Compromise for Anti-Bacterial and Anti-Biofilm Action Combined with Wound-Healing Properties. *J. Colloid Interface Sci.* **2017**, *498*, 271–281. https://doi.org/10.1016/j.jcis.2017.03.062.

(33) Bertoglio, F.; De Vita, L.; D'Agostino, A.; Fernandez, Y. D.; Falqui, A.; Casu, A.; Merli, D.; Milanese, C.; Rossi, S.; Taglietti, A.; Visai, L.; Pallavicini, P. Increased Antibacterial and Antibiofilm Properties of Silver Nanoparticles Using Silver Fluoride as Precursor. *Molecules* **2020**, *25* (15), 3494. https://doi.org/10.3390/molecules25153494.

(34) Jain, P. K.; Huang, X.; El-Sayed, I. H.; El-Sayed, M. A. Noble Metals on the Nanoscale: Optical and Photothermal Properties and Some Applications in Imaging, Sensing, Biology, and Medicine. *Acc. Chem. Res.* **2008**, *41* (12), 1578–1586. https://doi.org/10.1021/AR7002804.

(35) Pallavicini, P.; Chirico, G.; Taglietti, A. Harvesting Light to Produce Heat: Photothermal Nanoparticles for Technological Applications and Biomedical Devices. *Chem. – A Eur. J.* **2021**, chem.202102123. https://doi.org/10.1002/CHEM.202102123.

(36) Webb, J. A.; Bardhan, R. Emerging Advances in Nanomedicine with Engineered Gold Nanostructures. *Nanoscale* **2014**, *6* (5), 2502–2530. https://doi.org/10.1039/C3NR05112A.

(37) Anker, J. N.; Hall, W. P.; Lyandres, O.; Shah, N. C.; Zhao, J.; Van Duyne, R. P. Biosensing with Plasmonic Nanosensors. *Nat. Mater. 2008 76* **2008**, *7* (6), 442–453. https://doi.org/10.1038/nmat2162.

(38) Atwater, H. A.; Polman, A. Erratum: Plasmonics for Improved Photovoltaic Devices. *Nat. Mater. 2010 910* **2010**, *9* (10), 865–865. https://doi.org/10.1038/nmat2866.

(39) Mendes, R.; Pedrosa, P.; Lima, J. C.; Fernandes, A. R.; Baptista, P. V. Photothermal Enhancement of Chemotherapy in Breast Cancer by Visible Irradiation of Gold Nanoparticles. *Sci. Reports 2017 71* **2017**, *7* (1), 1–9. https://doi.org/10.1038/s41598-017-11491-8.

(40) Riley, R. S.; Day, E. S. Gold Nanoparticle-Mediated Photothermal Therapy: Applications and Opportunities for Multimodal Cancer Treatment. *Wiley*

Interdiscip. Rev. Nanomedicine Nanobiotechnology **2017**, *9* (4), e1449. https://doi.org/10.1002/WNAN.1449.

(41)   Kim, H. S.; Lee, D. Y. Near-Infrared-Responsive Cancer Photothermal and Photodynamic Therapy Using Gold Nanoparticles. *Polym. 2018, Vol. 10, Page 961* **2018**, *10* (9), 961. https://doi.org/10.3390/POLYM10090961.

(42)   Tang, H.; Yao, L.; Yang, J.; Li, W.; Teng, Z.; Xu, C. Near-Infrared-Light-Induced Fast Drug Release Platform: Mesoporous Silica-Coated Gold Nanoframes for Thermochemotherapy. *Part. Part. Syst. Charact.* **2016**, *33* (6), 316–322. https://doi.org/10.1002/PPSC.201600062.

(43)   Fu, G.; Sanjay, S. T.; Dou, M.; Li, X. Nanoparticle-Mediated Photothermal Effect Enables a New Method for Quantitative Biochemical Analysis Using a Thermometer. *Nanoscale* **2016**, *8* (10), 5422–5427. https://doi.org/10.1039/C5NR09051B.

(44)   Paviolo, C.; Haycock, J. W.; Yong, J.; Yu, A.; Stoddart, P. R.; Mcarthur, S. L. Laser Exposure of Gold Nanorods Can Increase Neuronal Cell Outgrowth. *Biotechnol. Bioeng.* **2013**, *110* (8), 2277–2291. https://doi.org/10.1002/BIT.24889.

(45)   Okkeh, M.; Bloise, N.; Restivo, E.; De Vita, L.; Pallavicini, P.; Visai, L. Gold Nanoparticles: Can They Be the next Magic Bullet for Multidrug-Resistant Bacteria? *Nanomaterials* **2021**, *11* (2), 1–30. https://doi.org/10.3390/nano11020312.

(46)   Nikoobakht, B.; El-Sayed, M. A. Preparation and Growth Mechanism of Gold Nanorods (NRs) Using Seed-Mediated Growth Method. *Chem. Mater.* **2003**, *15* (10), 1957–1962. https://doi.org/10.1021/cm020732l.

(47)   Casu, A.; Cabrini, E.; Donà, A.; Falqui, A.; Diaz-Fernandez, Y.; Milanese, C.; Taglietti, A.; Pallavicini, P. Controlled Synthesis of Gold Nanostars by Using a Zwitterionic Surfactant. *Chem. - A Eur. J.* **2012**, *18* (30), 9381–9390. https://doi.org/10.1002/chem.201201024.

(48)   Sironi, L.; Freddi, S.; Caccia, M.; Pozzi, P.; Rossetti, L.; Pallavicini, P.; Donà, A.; Cabrini, E.; Gualtieri, M.; Rivolta, I.; Panariti, A.; D'Alfonso, L.; Collini, M.; Chirico, G. Gold Branched Nanoparticles for Cellular Treatments. *J.*

Phys. Chem. C **2012**, *116* (34), 18407–18418. https://doi.org/10.1021/jp305021k.

(49)   Poletti, A.; Fracasso, G.; Conti, G.; Pilot, R.; Amendola, V. Laser Generated Gold Nanocorals with Broadband Plasmon Absorption for Photothermal Applications. *Nanoscale* **2015**, *7* (32), 13702–13714. https://doi.org/10.1039/c5nr03442f.

(50)   Hemmer, E.; Benayas, A.; Légaré, F.; Vetrone, F. Exploiting the Biological Windows: Current Perspectives on Fluorescent Bioprobes Emitting above 1000 Nm. *Nanoscale Horizons* **2016**, *1* (3), 168–184. https://doi.org/10.1039/C5NH00073D.

(51)   Mahmoud, N. N.; Alkilany, A. M.; Khalil, E. A.; Al-Bakri, A. G. Nano-Photothermal Ablation Effect of Hydrophilic and Hydrophobic Functionalized Gold Nanorods on Staphylococcus Aureus and Propionibacterium Acnes. *Sci. Rep.* **2018**, *8* (1), 6881. https://doi.org/10.1038/s41598-018-24837-7.

(52)   Guerrero-Martínez, A.; Barbosa, S.; Pastoriza-Santos, I.; Liz-Marzán, L. M. Nanostars Shine Bright for You: Colloidal Synthesis, Properties and Applications of Branched Metallic Nanoparticles. *Curr. Opin. Colloid Interface Sci.* **2011**, *16* (2), 118–127. https://doi.org/10.1016/J.COCIS.2010.12.007.

(53)   Pallavicini, P.; Donà, A.; Casu, A.; Chirico, G.; Collini, M.; Dacarro, G.; Falqui, A.; Milanese, C.; Sironi, L.; Taglietti, A. Triton X-100 for Three-Plasmon Gold Nanostars with Two Photothermally Active NIR (near IR) and SWIR (Short-Wavelength IR) Channels. *Chem. Commun.* **2013**, *49* (56), 6265–6267. https://doi.org/10.1039/c3cc42999g.

(54)   Zhu, J.; Gao, J.; Li, J.-J.; Li, X.; Zhao, J.-W. Improve the Plasmonic Spectral Detection of Alpha-Fetoprotein: The Effect of Branch Length on the Coagulation of Gold Nanostars. *Plasmonics* **2016**, *11* (4), 1175–1182. https://doi.org/10.1007/s11468-015-0157-2.

(55)   Zhu, J.; Liu, M.-J.; Li, J.-J.; Li, X.; Zhao, J.-W. Multi-Branched Gold Nanostars with Fractal Structure for SERS Detection of the Pesticide Thiram. *Spectrochim. Acta Part A Mol. Biomol. Spectrosc.* **2018**, *189*, 586–593.

https://doi.org/10.1016/j.saa.2017.08.074.

(56)   Pallavicini, P.; Basile, S.; Chirico, G.; Dacarro, G.; D'Alfonso, L.; Donà, A.; Patrini, M.; Falqui, A.; Sironi, L.; Taglietti, A. Monolayers of Gold Nanostars with Two Near-IR LSPRs Capable of Additive Photothermal Response. *Chem. Commun.* **2015**, *51* (65), 12928–12930. https://doi.org/10.1039/C5CC04144A.

(57)   Palza, H. Antimicrobial Polymers with Metal Nanoparticles. *Int. J. Mol. Sci.* **2015**, *16* (1), 2099–2116. https://doi.org/10.3390/ijms16012099.

(58)   Curtis, L. T. Prevention of Hospital-Acquired Infections: Review of Non-Pharmacological Interventions. *J. Hosp. Infect.* **2008**, *69* (3), 204–219. https://doi.org/10.1016/J.JHIN.2008.03.018.

(59)   Kenawy, E. R.; Worley, S. D.; Broughton, R. The Chemistry and Applications of Antimicrobial Polymers: A State-of-the-Art Review. *Biomacromolecules* **2007**, *8* (5), 1359–1384. https://doi.org/10.1021/BM061150Q.

(60)   Muñoz-Bonilla, A.; Fernández-García, M. Polymeric Materials with Antimicrobial Activity. *Prog. Polym. Sci.* **2012**, *37* (2), 281–339. https://doi.org/10.1016/J.PROGPOLYMSCI.2011.08.005.

(61)   Thomas, V.; Yallapu, M. M.; Sreedhar, B.; Bajpai, S. K. A Versatile Strategy to Fabricate Hydrogel–Silver Nanocomposites and Investigation of Their Antimicrobial Activity. *J. Colloid Interface Sci.* **2007**, *315* (1), 389–395. https://doi.org/10.1016/J.JCIS.2007.06.068.

(62)   Liu, S.; He, J.; Xue, J.; Ding, W. Efficient Fabrication of Transparent Antimicrobial Poly(Vinyl Alcohol) Thin Films. *J. Nanoparticle Res.* **2009**, *11* (3), 553–560. https://doi.org/10.1007/S11051-007-9321-8/FIGURES/6.

(63)   Murthy, P. S. K.; Murali Mohan, Y.; Varaprasad, K.; Sreedhar, B.; Mohana Raju, K. First Successful Design of Semi-IPN Hydrogel–Silver Nanocomposites: A Facile Approach for Antibacterial Application. *J. Colloid Interface Sci.* **2008**, *318* (2), 217–224. https://doi.org/10.1016/J.JCIS.2007.10.014.

(64)   Murali Mohan, Y.; Lee, K.; Premkumar, T.; Geckeler, K. E. Hydrogel

Networks as Nanoreactors: A Novel Approach to Silver Nanoparticles for Antibacterial Applications. *Polymer (Guildf).* **2007**, *48* (1), 158–164. https://doi.org/10.1016/J.POLYMER.2006.10.045.

(65)   Falletta, E.; Bonini, M.; Fratini, E.; Lo Nostro, A.; Pesavento, G.; Becheri, A.; Lo Nostro, P.; Canton, P.; Baglioni, P. Clusters of Poly(Acrylates) and Silver Nanoparticles: Structure and Applications for Antimicrobial Fabrics. *J. Phys. Chem. C* **2008**, *112* (31), 11758–11766. https://doi.org/10.1021/JP8035814.

(66)   Ma, Y. Q.; Yi, J. Z.; Zhang, L. M. A Facile Approach to Incorporate Silver Nanoparticles into Dextran-Based Hydrogels for Antibacterial and Catalytical Application. *http://dx.doi.org/10.1080/10601320902852031* **2009**, *46* (6), 643–648. https://doi.org/10.1080/10601320902852031.

(67)   Sharma, S.; Sanpui, P.; Chattopadhyay, A.; Ghosh, S. S. Fabrication of Antibacterial Silver Nanoparticle - Sodium Alginate-Chitosan Composite Films. *RSC Adv.* **2012**, *2* (13), 5837–5843. https://doi.org/10.1039/C2RA00006G/.

(68)   Pallavicini, P.; Dona, A.; Taglietti, A.; Minzioni, P.; Patrini, M.; Dacarro, G.; Chirico, G.; Sironi, L.; Bloise, N.; Visaie, L.; Scarabelli, L. Self-Assembled Monolayers of Gold Nanostars: A Convenient Tool for near-IR Photothermal Biofilm Eradication. *Chem. Commun.* **2014**, *50* (16), 1969–1971. https://doi.org/10.1039/c3cc48667b.

(69)   Borzenkov, M.; Pallavicini, P.; Chirico, G. Photothermally Active Inorganic Nanoparticles: From Colloidal Solutions to Photothermally Active Printed Surfaces and Polymeric Nanocomposite Materials. *Eur. J. Inorg. Chem.* **2019**, *2019* (41), 4397–4404. https://doi.org/10.1002/ejic.201900836.

(70)   Bermúdez-Jiménez, C.; Romney, M. G.; Roa-Flores, S. A.; Martínez-Castañón, G.; Bach, H. Hydrogel-Embedded Gold Nanorods Activated by Plasmonic Photothermy with Potent Antimicrobial Activity. *Nanomedicine Nanotechnology, Biol. Med.* **2019**, *22*, 102093. https://doi.org/10.1016/j.nano.2019.102093.

(71)   Toci, G.; Olgiati, F.; Pallavicini, P.; Fernandez, Y. A. D.; De Vita, L.; Dacarro, G.; Grisoli, P.; Taglietti, A. Gold Nanostars Embedded in PDMS Films: A

Photothermal Material for Antibacterial Applications. *Nanomaterials* **2021**, *11* (12), 3252. https://doi.org/10.3390/NANO11123252.

(72)   Borzenkov, M.; Moros, M.; Tortiglione, C.; Bertoldi, S.; Contessi, N.; Faré, S.; Taglietti, A.; D'Agostino, A.; Pallavicini, P.; Collini, M.; Chirico, G. Fabrication of Photothermally Active Poly(Vinyl Alcohol) Films with Gold Nanostars for Antibacterial Applications. *Beilstein J. Nanotechnol.* **2018**, *9* (1), 2040–2048. https://doi.org/10.3762/bjnano.9.193.

(73)   Borzenkov, M.; Chirico, G.; Pallavicini, P.; Sperandeo, P.; Polissi, A.; Dacarro, G.; Doveri, L.; Collini, M.; Sironi, L.; Bouzin, M.; D'Alfonso, L. Nanocomposite Sprayed Films with Photo-Thermal Properties for Remote Bacteria Eradication. *Nanomaterials* **2020**, *10* (4). https://doi.org/10.3390/nano10040786.

(74)   Cennamo, N.; Donà, A.; Pallavicini, P.; D'Agostino, G.; Dacarro, G.; Zeni, L.; Pesavento, M.; D'Agostino, G.; Dacarro, G.; Zeni, L.; Pesavento, M. Sensitive Detection of 2, 4, 6-Trinitrotoluene by Tridimensional Monitoring of Molecularly Imprinted Polymer with Optical Fiber and Five-Branched Gold Nanostars. *Sensors Actuators B Chem.* **2015**, *208*, 291–298. https://doi.org/10.1016/j.snb.2014.10.079.

(75)   Bright, R. M.; Musick, M. D.; Natan, M. J. Preparation and Characterization of Ag Colloid Monolayers. *Langmuir* **1998**, *14* (20), 5695. https://doi.org/10.1021/la980138j.

(76)   Gentry, S. T.; Kendra, S. F.; Bezpalko, M. W. Ostwald Ripening in Metallic Nanoparticles: Stochastic Kinetics. *J. Phys. Chem. C* **2011**, *115* (26), 12736–12741. https://doi.org/10.1021/jp2009786.

(77)   Zhang, Q.; Jing, H.; Li, G. G.; Lin, Y.; Blom, D. A.; Wang, H. Intertwining Roles of Silver Ions, Surfactants, and Reducing Agents in Gold Nanorod Overgrowth: Pathway Switch between Silver Underpotential Deposition and Gold–Silver Codeposition. *Chem. Mater.* **2016**, *28* (8), 2728–2741. https://doi.org/10.1021/acs.chemmater.6b00389.

(78)   Attia, Y. A.; Buceta, D.; Requejo, F. G.; Giovanetti, L. J.; López-Quintela, M. A. Photostability of Gold Nanoparticles with Different Shapes: The Role of

Ag Clusters. *Nanoscale* **2015**, *7* (26), 11273–11279. https://doi.org/10.1039/C5NR01887K.

(79)   Attia, Y. A.; Buceta, D.; Blanco-Varela, C.; Mohamed, M. B.; Barone, G.; López-Quintela, M. A. Structure-Directing and High-Efficiency Photocatalytic Hydrogen Production by Ag Clusters. *J. Am. Chem. Soc.* **2014**, *136* (4), 1182–1185. https://doi.org/10.1021/ja410451m.

(80)   Pallavicini, P.; Bassi, B.; Chirico, G.; Collini, M.; Dacarro, G.; Fratini, E.; Grisoli, P.; Patrini, M.; Sironi, L.; Taglietti, A.; Moritz, M.; Sorzabal-Bellido, I.; Susarrey-Arce, A.; Latter, E.; Beckett, A. J.; Prior, I. A.; Raval, R.; Diaz Fernandez, Y. A. Modular Approach for Bimodal Antibacterial Surfaces Combining Photo-Switchable Activity and Sustained Biocidal Release. *Sci. Rep.* **2017**, *7* (1), 1–10. https://doi.org/10.1038/s41598-017-05693-3.

(81)   Grisoli, P.; De Vita, L.; Milanese, C.; Taglietti, A.; Fernandez, Y. D.; Bouzin, M.; D'alfonso, L.; Sironi, L.; Rossi, S.; Vigani, B.; Sperandeo, P.; Polissi, A.; Pallavicini, P. PVA Films with Mixed Silver Nanoparticles and Gold Nanostars for Intrinsic and Photothermal Antibacterial Action. *Nanomaterials* **2021**, *11* (6), 1387. https://doi.org/10.3390/nano11061387.

(82)   Hajji, S.; Chaker, A.; Jridi, M.; Maalej, H.; Jellouli, K.; Boufi, S.; Nasri, M. Structural Analysis, and Antioxidant and Antibacterial Properties of Chitosan-Poly (Vinyl Alcohol) Biodegradable Films. *Environ. Sci. Pollut. Res.* **2016**, *23* (15), 15310–15320. https://doi.org/10.1007/s11356-016-6699-9.

(83)   Tripathi, S.; Mehrotra, G. K.; Dutta, P. K. Preparation and Physicochemical Evaluation of Chitosan/Poly(Vinyl Alcohol)/Pectin Ternary Film for Food-Packaging Applications. *Carbohydr. Polym.* **2010**, *79* (3), 711–716. https://doi.org/10.1016/j.carbpol.2009.09.029.

(84)   Rossi, S.; Mori, M.; Vigani, B.; Bonferoni, M. C.; Sandri, G.; Riva, F.; Caramella, C.; Ferrari, F. A Novel Dressing for the Combined Delivery of Platelet Lysate and Vancomycin Hydrochloride to Chronic Skin Ulcers: Hyaluronic Acid Particles in Alginate Matrices. *Eur. J. Pharm. Sci.* **2018**, *118*, 87–95. https://doi.org/10.1016/j.ejps.2018.03.024.

(85)   Musetti, A.; Paderni, K.; Fabbri, P.; Pulvirenti, A.; Al-Moghazy, M.; Fava, P.;

Al-Moghazy, M.; Fava, P.; Al-Moghazy, M.; Fava, P. Poly (Vinyl Alcohol)-based Film Potentially Suitable for Antimicrobial Packaging Applications. *J. Food Sci.* **2014**, *79* (4), E577–E582. https://doi.org/10.1111/1750-3841.12375.

(86)   Russell, H.; Ayliffe´s. *Principles and Practice of Disinfection, Preservation & Sterilization*; Fraise, A. P., Lambert, P. A., Maillard, J.-Y., Eds.; Blackwell, 2004.

(87)   Borzenkov, M.; D'Alfonso, L.; Polissi, A.; Sperandeo, P.; Collini, M.; Dacarro, G.; Taglietti, A.; Chirico, G.; Pallavicini, P. Novel Photo-Thermally Active Polyvinyl Alcohol-Prussian Blue Nanoparticles Hydrogel Films Capable of Eradicating Bacteria and Mitigating Biofilms. *Nanotechnology* **2019**, *30* (29), 295702. https://doi.org/10.1088/1361-6528/AB15F9.

(88)   Evanoff, D. D.; Chumanov, G. Synthesis and Optical Properties of Silver Nanoparticles and Arrays. *ChemPhysChem* **2005**, *6* (7), 1221 – 1231. https://doi.org/10.1002/cphc.200500113.

(89)   Guzman, M.; Dille, J.; Godet, S. Synthesis and Antibacterial Activity of Silver Nanoparticles against Gram-Positive and Gram-Negative Bacteria. *Nanomedicine Nanotechnology, Biol. Med.* **2012**, *8* (1), 37–45. https://doi.org/10.1016/j.nano.2011.05.007.

(90)   Bastús, N. G.; Merkoçi, F.; Piella, J.; Puntes, V. Synthesis of Highly Monodisperse Citrate-Stabilized Silver Nanoparticles of up to 200 Nm: Kinetic Control and Catalytic Properties. *Chem. Mater.* **2014**, *26* (9), 2836–2846. https://doi.org/10.1021/cm500316k.

(91)   Link, S.; El-Sayed, M. A. Spectral Properties and Relaxation Dynamics of Surface Plasmon Electronic Oscillations in Gold and Silver Nanodots and Nanorods. *J. Phys. Chem. B* **1999**, *103* (40), 8410–8426. https://doi.org/10.1021/jp9917648.

(92)   Dacarro, G.; Pallavicini, P.; Bertani, S. M.; Chirico, G.; D'Alfonso, L.; Falqui, A.; Marchesi, N.; Pascale, A.; Sironi, L.; Taglietti, A.; Zuddas, E. Synthesis of Reduced-Size Gold Nanostars and Internalization in SH-SY5Y Cells. *J. Colloid Interface Sci.* **2017**, *505*, 1055–1064. https://doi.org/10.1016/j.jcis.2017.06.102.

(93)   Demitri, C.; Del Sole, R.; Scalera, F.; Sannino, A.; Vasapollo, G.; Maffezzoli, A.; Ambrosio, L.; Nicolais, L. Novel Superabsorbent Cellulose-based Hydrogels Crosslinked with Citric Acid. *J. Appl. Polym. Sci.* **2008**, *110* (4), 2453–2460. https://doi.org/10.1002/app.28660.

(94)   Pallavicini, P.; Bernhard, C.; Chirico, G.; Dacarro, G.; Denat, F.; Donà, A.; Milanese, C.; Taglietti, A. Gold Nanostars Co-Coated with the Cu (II) Complex of a Tetraazamacrocyclic Ligand. *Dalt. Trans.* **2015**, *44* (12), 5652–5661. https://doi.org/10.1039/c4dt03042g.

(95)   Pallavicini, P.; De Vita, L.; Merlin, F.; Milanese, C.; Borzenkov, M.; Taglietti, A.; Chirico, G. Suitable Polymeric Coatings to Avoid Localized Surface Plasmon Resonance Hybridization in Printed Patterns of Photothermally Responsive Gold Nanoinks. *Molecules* **2020**, *25* (11), 2499. https://doi.org/10.3390/molecules25112499.

(96)   Schnepf, M. J.; Mayer, M.; Kuttner, C.; Tebbe, M.; Wolf, D.; Dulle, M.; Altantzis, T.; Formanek, P.; Förster, S.; Bals, S.; König, T. A. F.; Fery, A. Nanorattles with Tailored Electric Field Enhancement. *Nanoscale* **2017**, *9* (27), 9376–9385. https://doi.org/10.1039/C7NR02952G.

(97)   Halas, N. J.; Lal, S.; Chang, W.-S.; Link, S.; Nordlander, P. Plasmons in Strongly Coupled Metallic Nanostructures. *Chem. Rev.* **2011**, *111* (6), 3913–3961. https://doi.org/10.1021/cr200061k.

(98)   Liu, S.-D. D.; Cheng, M.-T. T. Linear Plasmon Ruler with Tunable Measurement Range and Sensitivity. *J. Appl. Phys.* **2010**, *108* (3), 34313. https://doi.org/10.1063/1.3463415.

(99)   Pallavicini, P.; Taglietti, A.; Dacarro, G.; Antonio Diaz-Fernandez, Y.; Galli, M.; Grisoli, P.; Patrini, M.; Santucci De Magistris, G.; Zanoni, R. Self-Assembled Monolayers of Silver Nanoparticles Firmly Grafted on Glass Surfaces: Low Ag+ Release for an Efficient Antibacterial Activity. *J. Colloid Interface Sci.* **2010**, *350* (1), 110–116. https://doi.org/10.1016/j.jcis.2010.06.019.

(100)   American National Standard for Safe Use of Lasers. *Laser Inst. Am.* **2007**.

(101)   Yuan, H.; Khoury, C. G.; Wilson, C. M.; Grant, G. A.; Bennett, A. J.; Vo-Dinh, T. In Vivo Particle Tracking and Photothermal Ablation Using Plasmon-

Resonant Gold Nanostars. *Nanomedicine Nanotechnology, Biol. Med.* **2012**, *8* (8), 1355–1363. https://doi.org/10.1016/j.nano.2012.02.005.

(102) Li, W.-R.; Xie, X.-B.; Shi, Q.-S.; Duan, S.-S.; Ouyang, Y.-S.; Chen, Y.-B. Antibacterial Effect of Silver Nanoparticles on Staphylococcus Aureus. *BioMetals* **2011**, *24* (1), 135–141. https://doi.org/10.1007/s10534-010-9381-6.

(103) Heuer-Jungemann, A.; Feliu, N.; Bakaimi, I.; Hamaly, M.; Alkilany, A.; Chakraborty, I.; Masood, A.; Casula, M. F.; Kostopoulou, A.; Oh, E.; Susumu, K.; Stewart, M. H.; Medintz, I. L.; Stratakis, E.; Parak, W. J.; Kanaras, A. G. The Role of Ligands in the Chemical Synthesis and Applications of Inorganic Nanoparticles. *Chem. Rev.* **2019**, *119* (8), 4819–4880. https://doi.org/10.1021/acs.chemrev.8b00733.

(104) X. The Bakerian Lecture. —Experimental Relations of Gold (and Other Metals) to Light. *Philos. Trans. R. Soc. London* **1857**, *147*, 145–181. https://doi.org/10.1098/RSTL.1857.0011.

(105) Turkevich, J.; Stevenson, P. C.; Hillier, J. A Study of the Nucleation and Growth Processes in the Synthesis of Colloidal Gold. *Discuss. Faraday Soc.* **1951**, *11* (0), 55–75. https://doi.org/10.1039/DF9511100055.

(106) FRENS, G. Controlled Nucleation for the Regulation of the Particle Size in Monodisperse Gold Suspensions. *Nat. Phys. Sci. 1973 241105* **1973**, *241* (105), 20–22. https://doi.org/10.1038/physci241020a0.

(107) Kimling, J.; Maier, M.; Okenve, B.; Kotaidis, V.; Ballot, H.; Plech, A. Turkevich Method for Gold Nanoparticle Synthesis Revisited. *J. Phys. Chem. B* **2006**, *110* (32), 15700–15707. https://doi.org/10.1021/JP061667W.

(108) Patungwasa, W.; Hodak, J. H. PH Tunable Morphology of the Gold Nanoparticles Produced by Citrate Reduction. *Mater. Chem. Phys.* **2008**, *108* (1), 45–54. https://doi.org/10.1016/J.MATCHEMPHYS.2007.09.001.

(109) Schulz, F.; Homolka, T.; Bastús, N. G.; Puntes, V.; Weller, H.; Vossmeyer, T. Little Adjustments Significantly Improve the Turkevich Synthesis of Gold Nanoparticles. *Langmuir* **2014**, *30* (35), 10779–10784. https://doi.org/10.1021/LA503209B/SUPPL_FILE/LA503209B_SI_001.PDF.

(110) Dinkel, R.; Braunschweig, B.; Peukert, W. Fast and Slow Ligand Exchange

at the Surface of Colloidal Gold Nanoparticles. *J. Phys. Chem. C* **2016**, *120* (3), 1673–1682. https://doi.org/10.1021/ACS.JPCC.5B11055/SUPPL_FILE/JP5B11055_SI_001 .PDF.

(111) Dreaden, E. C.; Alkilany, A. M.; Huang, X.; Murphy, C. J.; El-Sayed, M. A. The Golden Age: Gold Nanoparticles for Biomedicine. *Chem. Soc. Rev.* **2012**, *41* (7), 2740–2779. https://doi.org/10.1039/C1CS15237H.

(112) Hühn, J.; Carrillo-Carrion, C.; Soliman, M. G.; Pfeiffer, C.; Valdeperez, D.; Masood, A.; Chakraborty, I.; Zhu, L.; Gallego, M.; Yue, Z.; Carril, M.; Feliu, N.; Escudero, A.; Alkilany, A. M.; Pelaz, B.; Pino, P. Del; Parak, W. J. Selected Standard Protocols for the Synthesis, Phase Transfer, and Characterization of Inorganic Colloidal Nanoparticles. *Chem. Mater.* **2017**, *29* (1), 399–461. https://doi.org/10.1021/ACS.CHEMMATER.6B04738/SUPPL_FILE/CM6B0 4738_SI_001.PDF.

(113) Pensa, E.; Cortés, E.; Corthey, G.; Carro, P.; Vericat, C.; Fonticelli, M. H.; Benítez, G.; Rubert, A. A.; Salvarezza, R. C. The Chemistry of the Sulfur– Gold Interface: In Search of a Unified Model. *Acc. Chem. Res.* **2012**, *45* (8), 1183–1192. https://doi.org/10.1021/AR200260P.

(114) Häkkinen, H. The Gold–Sulfur Interface at the Nanoscale. *Nat. Chem. 2012 46* **2012**, *4* (6), 443–455. https://doi.org/10.1038/nchem.1352.

(115) Azcárate, J. C.; Corthey, G.; Pensa, E.; Vericat, C.; Fonticelli, M. H.; Salvarezza, R. C.; Carro, P. Understanding the Surface Chemistry of Thiolate-Protected Metallic Nanoparticles. *J. Phys. Chem. Lett.* **2013**, *4* (18), 3127–3138. https://doi.org/10.1021/jz401526y.

(116) Ram, S.; Fecht, H. J. Modulating Up-Energy Transfer and Violet-Blue Light Emission in Gold Nanoparticles with Surface Adsorption of Poly(Vinyl Pyrrolidone) Molecules. *J. Phys. Chem. C* **2011**, *115* (16), 7817–7828. https://doi.org/10.1021/JP105941H.

(117) Sun, X.; Dong, S.; Wang, E. One-Step Synthesis and Characterization of Polyelectrolyte-Protected Gold Nanoparticles through a Thermal Process. *Polymer (Guildf).* **2004**, *45* (7), 2181–2184.

https://doi.org/10.1016/J.POLYMER.2004.01.010.

(118) Newman, J. D. S.; Blanchard, G. J. Formation and Encapsulation of Gold Nanoparticles Using a Polymeric Amine Reducing Agent. *J. Nanoparticle Res. 2006 95* **2006**, *9* (5), 861–868. https://doi.org/10.1007/S11051-006-9145-Y.

(119) Wang, Z.; Tan, B.; Hussain, I.; Schaeffer, N.; Wyatt, M. F.; Brust, M.; Cooper, A. I. Design of Polymeric Stabilizers for Size-Controlled Synthesis of Monodisperse Gold Nanoparticles in Water. *Langmuir* **2007**, *23* (2), 885–895. https://doi.org/10.1021/LA062623H/SUPPL_FILE/LA062623HSI20060907_1 22256.PDF.

(120) Karakoti, A. S.; Das, S.; Thevuthasan, S.; Seal, S. PEGylated Inorganic Nanoparticles. *Angew. Chemie Int. Ed.* **2011**, *50* (9), 1980–1994. https://doi.org/10.1002/ANIE.201002969.

(121) Barenholz, Y. Doxil® — The First FDA-Approved Nano-Drug: Lessons Learned. *J. Control. Release* **2012**, *160* (2), 117–134. https://doi.org/10.1016/J.JCONREL.2012.03.020.

(122) Suk, J. S.; Xu, Q.; Kim, N.; Hanes, J.; Ensign, L. M. PEGylation as a Strategy for Improving Nanoparticle-Based Drug and Gene Delivery. *Adv. Drug Deliv. Rev.* **2016**, *99*, 28–51. https://doi.org/10.1016/J.ADDR.2015.09.012.

(123) Oh, E.; Susumu, K.; Goswami, R.; Mattoussi, H. One-Phase Synthesis of Water-Soluble Gold Nanoparticles with Control over Size and Surface Functionalities. *Langmuir* **2010**, *26* (10), 7604–7613. https://doi.org/10.1021/LA904438S/SUPPL_FILE/LA904438S_SI_001.PDF.

(124) Borzenkov, M.; Chirico, G.; D'Alfonso, L.; Sironi, L.; Collini, M.; Cabrini, E.; Dacarro, G.; Milanese, C.; Pallavicini, P.; Taglietti, A.; Bernhard, C.; Denat, F. Thermal and Chemical Stability of Thiol Bonding on Gold Nanostars. *Langmuir* **2015**, *31* (29), 8081–8091. https://doi.org/10.1021/ACS.LANGMUIR.5B01473/SUPPL_FILE/LA5B0147 3_SI_001.PDF.

(125) Sperling, R. A.; Parak, W. J. Surface Modification, Functionalization and Bioconjugation of Colloidal Inorganic Nanoparticles. *Philos. Trans. R. Soc. A Math. Phys. Eng. Sci.* **2010**, *368* (1915), 1333–1383.

https://doi.org/10.1098/RSTA.2009.0273.

(126) Fernandes, R.; Smyth, N. R.; Muskens, O. L.; Nitti, S.; Heuer-Jungemann, A.; Ardern-Jones, M. R.; Kanaras, A. G. Interactions of Skin with Gold Nanoparticles of Different Surface Charge, Shape, and Functionality. *Small* **2015**, *11* (6), 713–721. https://doi.org/10.1002/SMLL.201401913.

(127) Kalsin, A. M.; Kowalczyk, B.; Wesson, P.; Paszewski, M.; Grzybowski, B. A. Studying the Thermodynamics of Surface Reactions on Nanoparticles by Electrostatic Titrations. *J. Am. Chem. Soc.* **2007**, *129* (21), 6664–6665. https://doi.org/10.1021/JA068329T/SUPPL_FILE/JA068329TSI20070410_042 100.PDF.

(128) Pallavicini, P.; Diaz-Fernandez, Y. A.; Pasotti, L. Micelles as Nanosized Containers for the Self-Assembly of Multicomponent Fluorescent Sensors. *Coord. Chem. Rev.* **2009**, *253* (17–18), 2226–2240. https://doi.org/10.1016/j.ccr.2008.11.010.

(129) Diaz-Fernandez, Y.; Foti, F.; Mangano, C.; Pallavicini, P.; Patroni, S.; Perez-Gramatges, A.; Rodriguez-Calvo, S. Micelles for the Self-Assembly of "off-on-off" Fluorescent Sensors for PH Windows. *Chem. - A Eur. J.* **2006**, *12* (3), 921–930. https://doi.org/10.1002/chem.200500613.

(130) Da Silva, F. L. B.; Bogren, D.; Söderman, O.; Åkesson, T.; Jönsson, B. Titration of Fatty Acids Solubilized in Cationic, Nonionic, and Anionic Micelles. Theory and Experiment. *J. Phys. Chem. B* **2002**, *106* (13), 3515–3522. https://doi.org/10.1021/JP012033M.

(131) Charron, G.; Hühn, D.; Perrier, A.; Cordier, L.; Pickett, C. J.; Nann, T.; Parak, W. J. On the Use of PH Titration to Quantitatively Characterize Colloidal Nanoparticles. *Langmuir* **2012**, *28* (43), 15141–15149. https://doi.org/10.1021/LA302570S.

(132) Wang, D.; Nap, R. J.; Lagzi, I.; Kowalczyk, B.; Han, S.; Grzybowski, B. A.; Szleifer, I. How and Why Nanoparticle's Curvature Regulates the Apparent PKa of the Coating Ligands. *J. Am. Chem. Soc.* **2011**, *133* (7), 2192–2197. https://doi.org/10.1021/JA108154A.

(133) DeVries, G. A.; Brunnbauer, M.; Hu, Y.; Jackson, A. M.; Long, B.; Neltner, B.

T.; Uzun, O.; Wunsch, B. H.; Stellacci, F. Divalent Metal Nanoparticles. *Science (80-.). * **2007**, *315* (5810), 358–361. https://doi.org/10.1126/SCIENCE.1133162/SUPPL_FILE/DEVRIES_SOM.PDF.

(134) Creager, S. E.; Clarke, J. Contact-Angle Titrations of Mixed .Omega.-Mercaptoalkanoic Acid/Alkanethiol Monolayers on Gold. Reactive vs Nonreactive Spreading, and Chain Length Effects on Surface PKa Values. *Langmuir* **2002**, *10* (10), 3675–3683. https://doi.org/10.1021/LA00022A048.

(135) Kane, V.; Mulvaney, P. Double-Layer Interactions between Self-Assembled Monolayers of ω-Mercaptoundecanoic Acid on Gold Surfaces. *Langmuir* **1998**, *14* (12), 3303–3311. https://doi.org/10.1021/LA971296Y.

(136) Gans, P.; Sabatini, A.; Vacca, A. Investigation of Equilibria in Solution. Determination of Equilibrium Constants with the HYPERQUAD Suite of Programs. *Talanta* **1996**, *43* (10), 1739–1753. https://doi.org/10.1016/0039-9140(96)01958-3.

(137) Das, S.; Heasman, P.; Ben, T.; Qiu, S. Porous Organic Materials: Strategic Design and Structure–Function Correlation. *Chem. Rev.* **2016**, *117* (3), 1515–1563. https://doi.org/10.1021/ACS.CHEMREV.6B00439.

(138) Yang, X. Y.; Chen, L. H.; Li, Y.; Rooke, J. C.; Sanchez, C.; Su, B. L. Hierarchically Porous Materials: Synthesis Strategies and Structure Design. *Chem. Soc. Rev.* **2017**, *46* (2), 481–558. https://doi.org/10.1039/C6CS00829A.

(139) Wang, W.; Zhou, M.; Yuan, D. Carbon Dioxide Capture in Amorphous Porous Organic Polymers. *J. Mater. Chem. A* **2017**, *5* (4), 1334–1347. https://doi.org/10.1039/C6TA09234A.

(140) Ding, S. Y.; Wang, W. Covalent Organic Frameworks (COFs): From Design to Applications. *Chem. Soc. Rev.* **2012**, *42* (2), 548–568. https://doi.org/10.1039/C2CS35072F.

(141) Kaur, P.; Hupp, J. T.; Nguyen, S. T. Porous Organic Polymers in Catalysis: Opportunities and Challenges. *ACS Catal.* **2011**, *1* (7), 819–835. https://doi.org/10.1021/CS200131G.

(142) Kim, S.; Lee, Y. M. Rigid and Microporous Polymers for Gas Separation

Membranes. *Prog. Polym. Sci.* **2015**, *43*, 1–32. https://doi.org/10.1016/J.PROGPOLYMSCI.2014.10.005.

(143) Amendola, V.; Pilot, R.; Frasconi, M.; Maragò, O. M.; Iatì, M. A. Surface Plasmon Resonance in Gold Nanoparticles: A Review. *J. Phys. Condens. Matter* **2017**, *29* (20). https://doi.org/10.1088/1361-648X/aa60f3.

(144) Sun, J. K.; Xu, Q. Functional Materials Derived from Open Framework Templates/Precursors: Synthesis and Applications. *Energy Environ. Sci.* **2014**, *7* (7), 2071–2100. https://doi.org/10.1039/C4EE00517A.

(145) Xiang, Z.; Cao, D. Porous Covalent–Organic Materials: Synthesis, Clean Energy Application and Design. *J. Mater. Chem. A* **2013**, *1* (8), 2691–2718. https://doi.org/10.1039/C2TA00063F.

(146) Dong, C. H.; He, L.; Xiao, Y. F.; Gaddam, V. R.; Ozdemir, S. K.; Han, Z. F.; Guo, G. C.; Yang, L. Fabrication of High-Q Polydimethylsiloxane Optical Microspheres for Thermal Sensing. *Appl. Phys. Lett.* **2009**, *94* (23), 231119. https://doi.org/10.1063/1.3152791.

(147) Quake, S. R.; Scherer, A. From Micro- to Nanofabrication with Soft Materials. *Science (80-.).* **2000**, *290* (5496), 1536–1540. https://doi.org/10.1126/SCIENCE.290.5496.1536/ASSET/16AAC7B0-9415-4318-A119-3207D22AA82F/ASSETS/GRAPHIC/SE4509008005.JPEG.

(148) Lee, J. N.; Park, C.; Whitesides, G. M. Solvent Compatibility of Poly(Dimethylsiloxane)-Based Microfluidic Devices. *Anal. Chem.* **2003**, *75* (23), 6544–6554. https://doi.org/10.1021/ac0346712.

(149) Zhou, J.; Ellis, A. V.; Voelcker, N. H. Recent Developments in PDMS Surface Modification for Microfluidic Devices. *Electrophoresis* **2010**, *31* (1), 2–16. https://doi.org/10.1002/ELPS.200900475.

(150) Hu, S.; Ren, X.; Bachman, M.; Sims, C. E.; Li, G. P.; Allbritton, N. L. Tailoring the Surface Properties of Poly(Dimethylsiloxane) Microfluidic Devices. *Langmuir* **2004**, *20* (13), 5569–5574. https://doi.org/10.1021/LA049974L.

(151) Chen, I. J.; Lindner, E. The Stability of Radio-Frequency Plasma-Treated Polydimethylsiloxane Surfaces. *Langmuir* **2007**, *23* (6), 3118–3122. https://doi.org/10.1021/LA0627720.

(152) Zhu, D.; Handschuh-Wang, S.; Zhou, X. Recent Progress in Fabrication and Application of Polydimethylsiloxane Sponges. *Journal of Materials Chemistry A*. Royal Society of Chemistry 2017, pp 16467–16497. https://doi.org/10.1039/c7ta04577h.

(153) Choi, S. J.; Kwon, T. H.; Im, H.; Moon, D. Il; Baek, D. J.; Seol, M. L.; Duarte, J. P.; Choi, Y. K. A Polydimethylsiloxane (PDMS) Sponge for the Selective Absorption of Oil from Water. *ACS Appl. Mater. Interfaces* **2011**, *3* (12), 4552–4556. https://doi.org/10.1021/am201352w.

(154) Zhao, X.; Li, L.; Li, B.; Zhang, J.; Wang, A. Durable Superhydrophobic/Superoleophilic PDMS Sponges and Their Applications in Selective Oil Absorption and in Plugging Oil Leakages. *J. Mater. Chem. A* **2014**, *2* (43), 18281–18287. https://doi.org/10.1039/C4TA04406A.

(155) Yu, C.; Yu, C.; Cui, L.; Song, Z.; Zhao, X.; Ma, Y.; Jiang, L.; Yu, C. L.; Cui, L. Y.; Song, Z. Y.; Zhao, X. Y.; Yu, C. M.; Ma, Y.; Jiang, L. Facile Preparation of the Porous PDMS Oil-Absorbent for Oil/Water Separation. *Adv. Mater. Interfaces* **2017**, *4* (3), 1600862. https://doi.org/10.1002/ADMI.201600862.

(156) Kang, S.; Lee, J.; Lee, S.; Kim, S.; Kim, J.-K.; Algadi, H.; Al-Sayari, S.; Kim, D.-E.; Kim, D.; Lee, T.; Kang, S.; Lee, J.; Lee, S.; Kim, S.; Algadi, H.; Kim, D.; Kim, D. E.; Lee, T.; Kim, J.; Al-Sayari, S. Highly Sensitive Pressure Sensor Based on Bioinspired Porous Structure for Real-Time Tactile Sensing. *Adv. Electron. Mater.* **2016**, *2* (12), 1600356. https://doi.org/10.1002/AELM.201600356.

(157) Gao, M.; Zhu, L.; Peh, C. K.; Ho, G. W. Solar Absorber Material and System Designs for Photothermal Water Vaporization towards Clean Water and Energy Production. *Energy Environ. Sci.* **2019**, *12* (3), 841–864. https://doi.org/10.1039/C8EE01146J.

(158) Wang, S.; Almenabawy, S. M.; Kherani, N. P.; Leung, S. N.; O'Brien, P. G. Solar-Driven Interfacial Water Evaporation Using Open-Porous PDMS Embedded with Carbon Nanoparticles. *ACS Appl. Energy Mater.* **2020**, *3* (4), 3378–3386. https://doi.org/10.1021/acsaem.9b02399.